POLITECNICO
MILANO 1863

SCUOLA DI INGEGNERIA INDUSTRIALE
E DELL'INFORMAZIONE

Spatially resolved investigation of methane oxidation over Pd-based catalyst: effect of fuel composition and water concentration

TESI DI LAUREA MAGISTRALE IN
ENERGY ENGINEERING
INGEGNERIA ENERGETICA

Author: **Paolo Comolli**

Student ID: 945169
Advisor: Gianpiero Groppi
Co-advisor: Vittoria Troisi
Academic Year: 2021-22

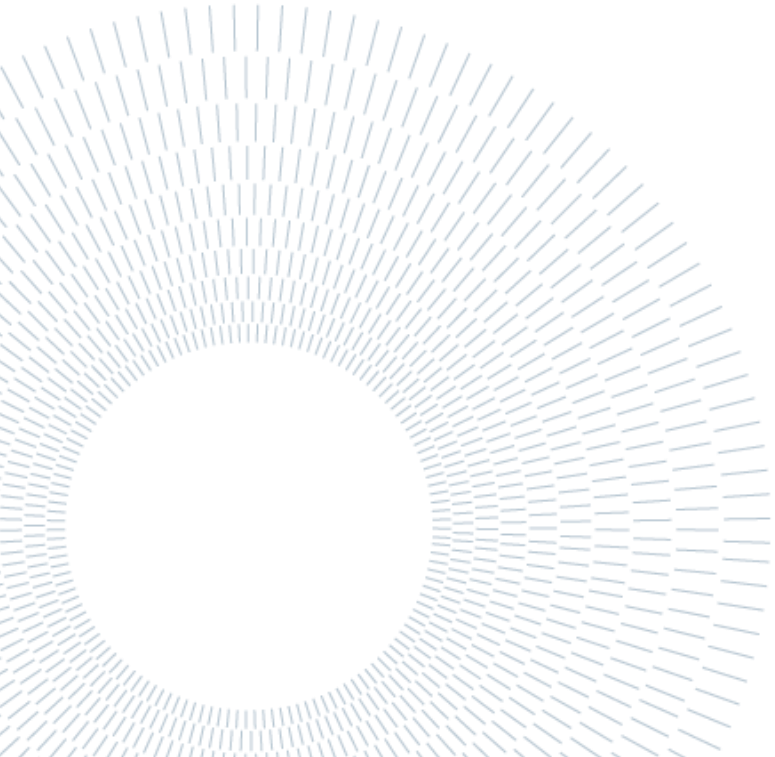

Abstract

Nowadays, growing environmental awareness is driving the transport sector towards the use of cleaner fuels. Among them, natural gas and biomethane seem to be very interesting.

The aftertreatment system of a natural gas vehicle consists of the so-called three-way catalytic converter (TWC), which is able to abate unburned hydrocarbons, CO and NO_X. The only drawback is that, at the typical temperature of NGV exhausts, methane is hard to be oxidized, due to its high stability.

In this work, a commercial Pd-Rh/Al_2O_3 catalyst has been tested using the spatially resolved sampling technique: concentration and temperature profiles have been evaluated, in order to better understand the reaction mechanisms on the catalytic surface, under different conditions.

Two experimental campaigns have been conducted, the first one carried out by using a CH_4/CO/H_2 mixture as fuel, the second one by testing pure CH_4. For both, focus was put on the effect of temperature and water inhibition on methane conversion.

Interesting results have been obtained. As it regards the first campaign, concentration profiles suggested the existence of an oxygen partial pressure threshold below which the catalyst results more active towards methane conversion. The relation between the reaction temperature and the occurrence of the oxygen threshold is in good agreement with previous evidences found in the literature.

The second experimental campaign highlighted that, under lean conditions, the effect of water inhibition is much more evident at lower temperatures. Under rich conditions, the presence of a new critical oxygen partial pressure was found.

Keywords: Methane oxidation; Lean; Rich; Pd-based catalyst; Natural gas; Concentration profiles; Temperature profiles; Water inhibition.

Abstract in italiano

Al giorno d'oggi, la crescente consapevolezza in tema ambientale sta spingendo il settore dei trasporti verso l'impiego di carburanti più puliti. Tra questi, il gas naturale e il biometano sembrano essere tra i più interessanti.

In questo lavoro di tesi, un catalizzatore commerciale del tipo Pd-Rh/Al_2O_3 è stato testato utilizzando tecniche di campionamento in situ, al fine di ottenere profili di concentrazione e temperatura. Questo è stato fatto per comprendere più a fondo i meccanismi di reazione che avvengono sulla superficie del catalizzatore in diverse condizioni.

Sono state condotte due campagne sperimentali, la prima utilizzando come combustibile una miscela CH_4/CO/H_2, la seconda testando CH_4 puro. In entrambi i casi, l'attenzione è stata focalizzata sull'effetto della temperatura e dell'inibizione da acqua sulla conversione del metano.

Sono stati ottenuti risultati piuttosto interessanti. Per quanto riguarda la prima campagna, i profili di concentrazione hanno suggerito l'esistenza di una soglia di pressione parziale dell'ossigeno al di sotto della quale il catalizzatore mostra una maggiore attività verso la conversione del metano. La corrispondenza tra la temperatura di reazione e la soglia dell'ossigeno è risultata essere in accordo con precedenti evidenze in letteratura. Per quanto riguarda la seconda campagna sperimentale, si è visto che, in condizioni magre, l'effetto inibitorio dell'acqua è molto più pronunciato alle basse temperature. In condizioni ricche, una nuova pressione parziale critica di ossigeno è stata trovata.

Parole chiave: Ossidazione del metano; Miscela magra; Miscela ricca; Catalizzatore a base Pd; Profili di concentrazione; Profili di temperatura; Inibizione da acqua

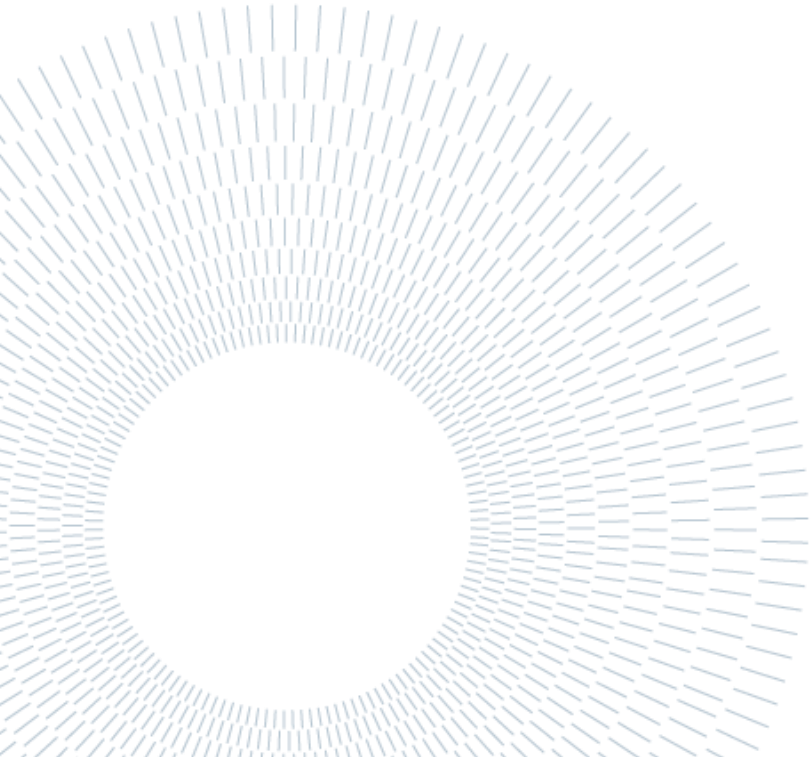

Contents

Introduction

In recent decades, interest in renewable energies has grown a lot due to an increased environmental awareness. The impact of the air pollution on human health [1] and on global warming [2], which is dramatically evident, pushes policymakers towards the introduction of severe restrictions on fossil fuel consumption. In Europe some regulations are being introduced to set new targets to mitigate the environmental impact. As illustrated in Figure A, in 2009 the RED (Renewable Energy Directive) introduced two main goals: to reduce greenhouse emissions by 55% (compared to 1990) by 2030 and to achieve the climate neutrality by 2050 [3]. To obtain these ambitious results the directive sets some subgoals by 2020: the reduction of greenhouse gas emissions to at least 20% and the achievement of a 10% contribution of energy from renewable sources in the transport sector. In 2020, there was a 31% cut in greenhouse gas emissions compared to 1990, 11% more than the RED target, but this is also driven by the large reduction in energy consumption due to the pandemic. In order to achieve the 2030 target and climate neutrality in 2050, new legislations by European countries are needed to strongly push for emissions reduction.

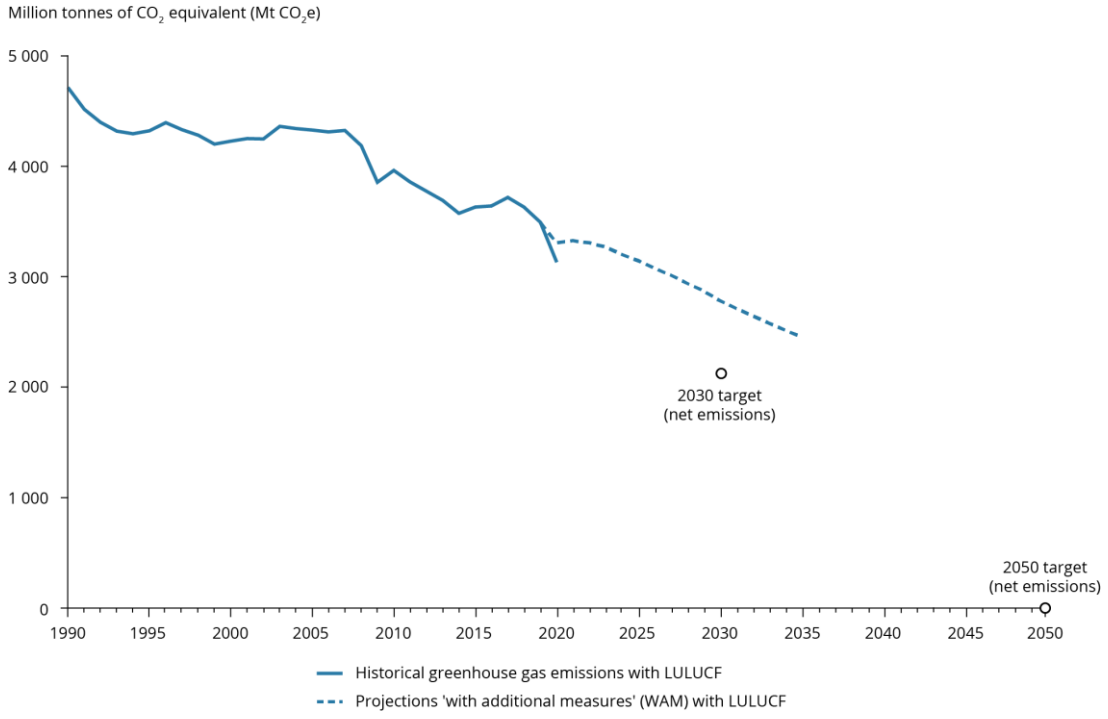

Figure A – GHG emissions trend and RED targets [4]

In Figure B, the GHG emission trend, divided by sectors, is represented. Greenhouse gas emissions decreased between 1990 and 2018 in sectors like energy supply, industry, residential, agriculture and waste management. Unfortunately, emissions from road transportation have increased with respect to 1990 levels.

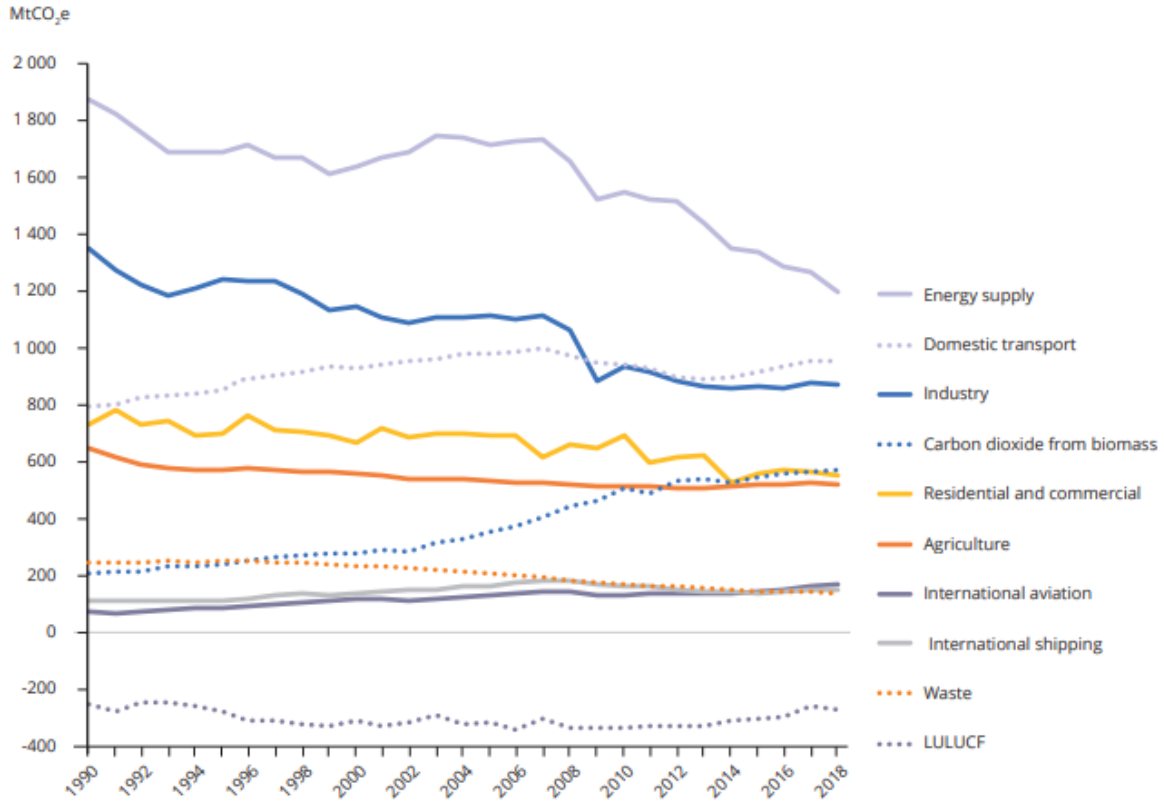

Figure B – GHG emissions trend by sectors [4]

In this scenario, it is easy to see that the implementation of cleaner transport fuels is also crucial, in order to have a smooth transition to climate neutrality.

CO_2 is a major contributor to global warming; to limit greenhouse gas emissions, increasing the number of CNG vehicles on the market could be a solution. Even if within the next few years renewable sources are likely to grow their share in all sectors, the emancipation from fossil sources seems to be a long-term objective. To reach the ambitious goals set by European policymakers, the natural gas exploitation could be inevitable. Figure C shows that road transportation accounts for 26% of EU CO_2 emissions; natural gas vehicles can drive the transition to cleaner means of transportation in the short to medium term, accompanying the transition to an electric transport sector.

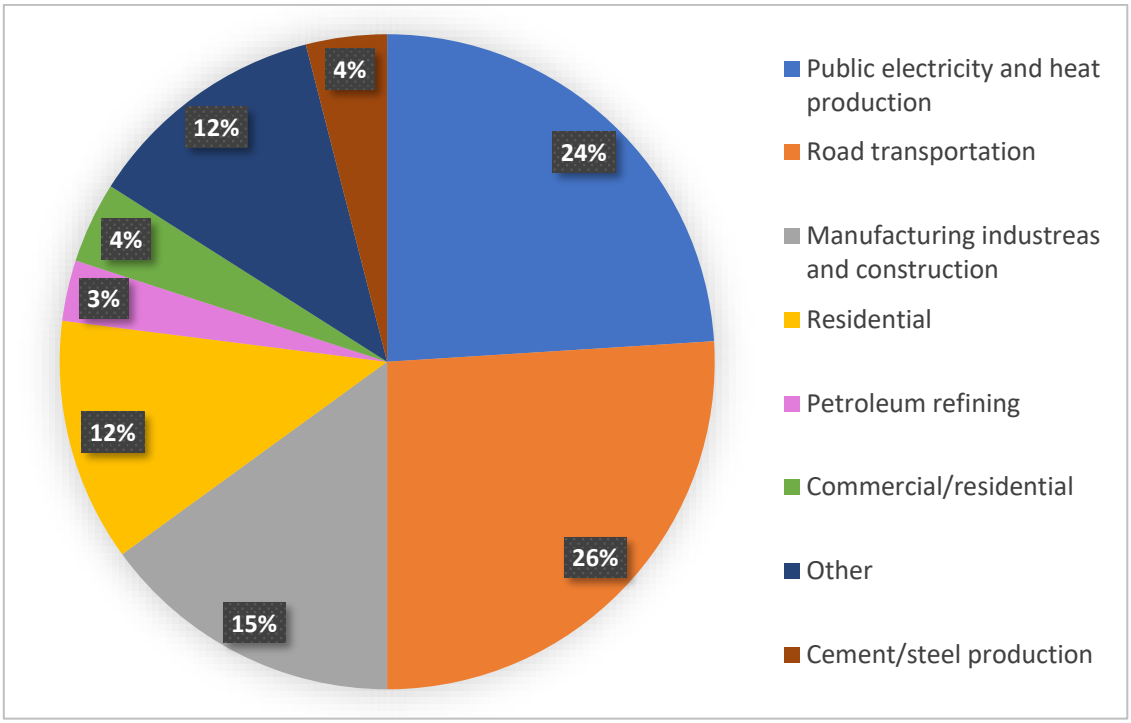

Figure C – EU-27 CO2 emissions by sectors (2020) [4]

But why NGVs could be a solution? The main component of NG is methane, the alkane characterized by the highest hydrogen/carbon ratio. This means that it is characterized by a higher heat of reaction per unit of CO_2 emitted compared to traditional fossil fuels. As a result, the value of greenhouse gas emissions per unit distance travelled is reduced. This is not the only advantage: NG is characterised by the absence of aromatic compounds and less sulfur, so less particulate matter and SO_x are also produced [5], [6]. In addition, natural gas is very abundant in the world and new reservoirs are discovered every year. Another advantage is that NG engines can also run on biomethane, which has much less environmental impact than fossil natural gas. There is one drawback that must be overcome for a large-scale development of natural gas vehicles: methane has a global warming potential (GWP) 32 times that of CO_2 [7]; to effectively reduce greenhouse gas emissions, unburned CH_4 must be avoided.

1 Catalytic combustion of methane State of art

In this chapter present regulations, future developments and most adopted solutions for methane emission abatement are introduced.

1.1. Regulatory background

In 2015, 197 countries signed the Paris Agreement, pledging to keep global warming well below 2 °C, aiming for a maximum increase of 1.5 °C, compared to the pre-industrial era [8]. The Green Deal - signed in 2019 - was Europe's response, setting an ambitious target of achieving zero net greenhouse gas emissions by 2050 [9], [10]. As already discussed, transport is responsible for a quarter of greenhouse gas emissions in the European Union. The Green Deal emphasises that to achieve climate neutrality it is necessary to reduce emissions produced by transport by 90%. To do this, it also encourages the production of sustainable alternative fuels to replace the fossil based ones, including Biomethane. To limit the on-board emissions in the transport sector, the European Union sets some standards that the new vehicles must meet. Today, the standard in use is the EURO 6 (Table 1.1), that is active since 2014 [11]. We should be close to the entry into force of EURO 7, which has already been discussed for some time. The latest postponement has moved the date for the official proposal to 20 July 2022. As it concerns how the levels of emissions are evaluated, in the past the NEDC (New European Driving Cycle) was adopted, whereas since September 2017 it has been substituted by the WLTP (Worldwide Harmonized Light Vehicles Test Procedure) [12].

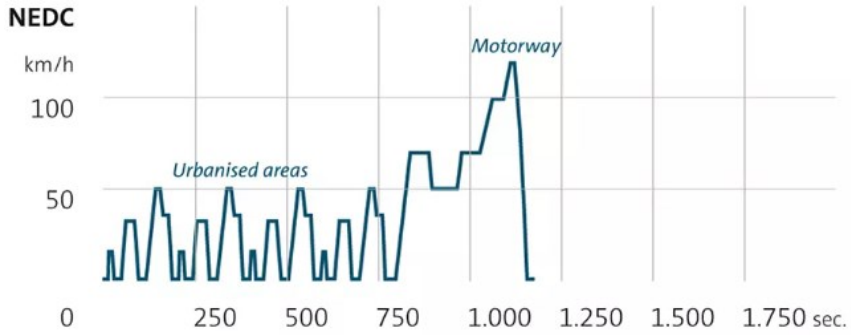

Figure 1. 1 – New European Driving Cycle (NEDC)

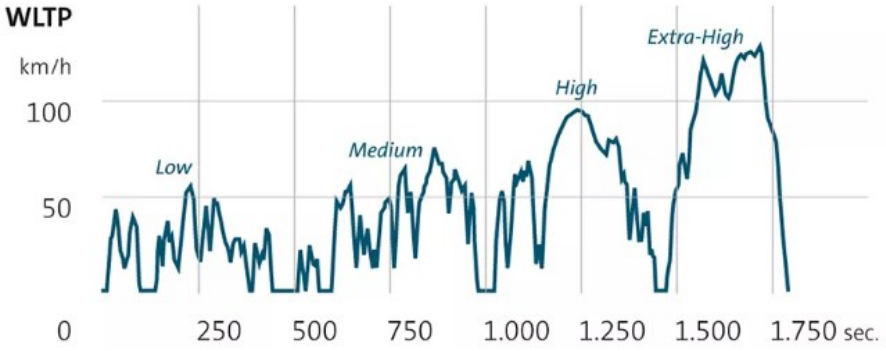

Figure 1. 2 – Worldwide Harmonized Light Vehicles Test Procedure (WLTP)

Both tests take place in the laboratory but the WLTP is more stringent and simulates road conditions in a more realistic way. Figures 1.1 and 1.2 show for each test the velocities reached during each phase. Today also a RDE (Real Driving Emissions Test) is adopted, to evaluate in more realistic way the emissions of NO_x and particulate matter [13]. During this test a car is fitted with PEMS (Portable Emission Measuring Systems) and it is driven on public roads in a range of different conditions.

Table 1. 1 – Euro 6 Emission Limits

Category	Engine	Limit values					
		CO	THC	NMHC	NO_x	THC+NO_x	PM
		L1 [mg/km]	L2 [mg/km]	L3 [mg/km]	L4 [mg/km]	L2+l4 [mg/km]	L4 [mg/km]
M	PI	1000	100	68	60	-	4.5
	CI	500	-	-	80	170	4.5
N1 (RM ≤ 1305 kg)	PI	1000	100	68	60	-	4.5
	CI	500	-	-	80	170	4.5
N1 (1305 kg ≤ RM ≤ 1760 kg)	PI	1810	130	90	75	-	4.5
	CI	630	-	-	105	195	4.5
N1 (RM ≥ 1760 kg)	PI	2270	160	108	82	-	4.5
	CI	740	-	-	125	215	4.5
N2	PI	2270	160	108	82	-	4.5
	CI	740	-	-	125	215	4.5

1.2. Natural Gas in Europe

Natural gas is an immediate alternative to oil for the transportation sector, since natural gas engine is a well-known technology. A lot of advantages derive from exploitation of natural gas as transportation fuel. From an environmental point of view, NG is characterized by lower greenhouse gases, NO_x and particulate matter emissions. NG is very aboundant all over the world, there are no problems related to availability. It has been estimated that the natural gas reserves, in 2020, in the various fields in the world amount to 188.1 trillion cubic meters. Interestingly, this trend has increased in recent years due to the large number of new deposits being discovered. [14].

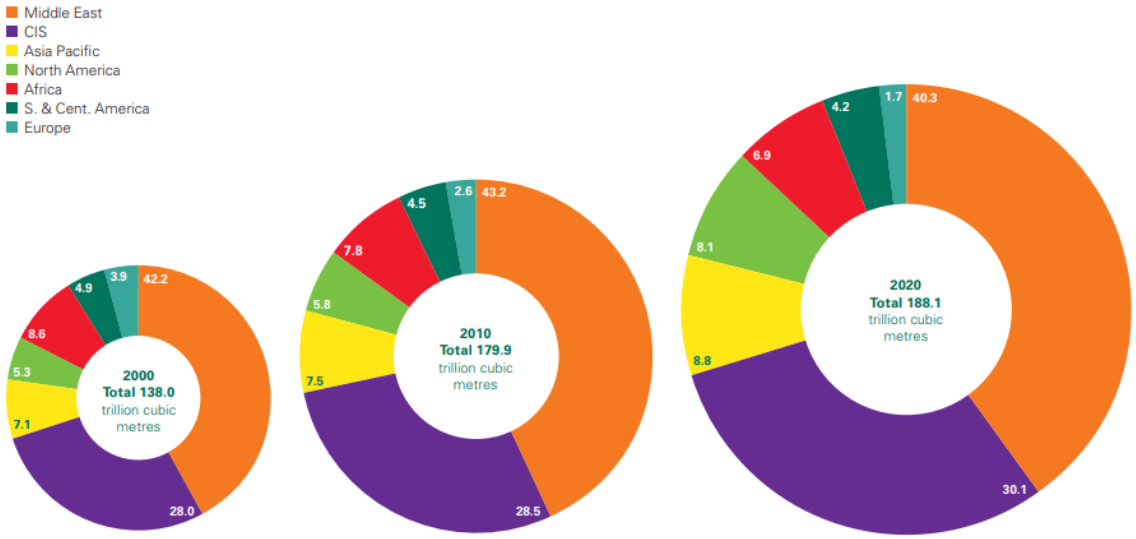

Figure 1. 3 – Natural gas reservoirs around the world [14]

For the transport sector we can use NG in form of Compressed Natural Gas (CNG) or Liquefied Natural Gas (LNG). As the name suggest, the LNG is obtained by liquefaction: natural gas is cooled down to really low temperatures until it becomes liquid. The advantage is that the obtained liquefied gas occupies 1/ 600 of the original volume. There is a drawback, a LNG vehicle is a more complex technology because the fuel needs to be maintained at about -160 °C. Due to the higher energy density and the less storage volume needed, LNG is the best solution for long trucking means of transportation [15].

The natural gas vehicle market is growing rapidly. In 2020, 55028 Natural Gas Passenger Cars, 3189 NG buses and 6802 NG trucks were registered in Europe. Also looking at the gas fueling station network, it is easy to understand that the upward trend is evident. Since 2020, the number of both CNG stations and LNG stations has

been increased by about 300 and 150 unities (CNG +8.1%, LNG +60%) [16]. By increasing the number of natural gas vehicles, improving the efficiency of the engines and increasing the quality of the after-treatments, a large reduction in GHG emissions can be achieved in the next few years.

1.3. Biomethane in Europe

Biomethane is a renewable energy source that can be derived from agricultural biomass or Organic Fraction Municipal Solid Waste. Its origins can rely on two different strategies. The most used today is the upgrading of Biogas [17]: 90% of Biomethane is obtained like this. Firstly we get Biogas from the anaerobic digestion of the organic matter, than CO_2 and other contaminants are removed to obtain quasi-pure CH_4 [18]. The other method is a thermal gasification of solid biomass, followed by a methanation reaction [19]. In the first step, thanks to the high temperature and the high pressure, solid biomass in broken down to obtain a gaseous mixture called Syngas (composed principally by CH_4, CO, CO_2, H_2 and small quantities of undesired compounds). Subsequently contaminants are removed and the remaining syngas is ready to be treated. Methanation is a catalytic reaction in which CO_x and H_2 react to obtain methane. Also in this case, after a process of purification, high percentage of CH_4 can be reached [20].

Exploiting biomethane as a fuel in the transport sector reduces greenhouse gas emissions as a zero emissions renewable gas, since any remaining lifecycle emisisons can be compensated by negative emissions created in agriculture producing biomethane.

This is not true for natural gas, for which there is a net increase in CO_2 in the atmosphere, because the CH_4 has been trapped underground for millions of years. An other great advantage of biomethane is that it can be moved through the existing methane pipelines and can be used directly in the vehicles that today run on natural gas. Furthermore, as far as the green transition of the transport sector is concerned, biomethane and electric vehicles are not in conflict. Biomethane can be used for vehicles that have to travel long distances (trucks, buses...) or in regions where the electricity grid is not sufficient to recharge many vehicles.

Today, about 17% of methane used in the transport sector is renewable, but this percentage is growing. By 2030, an average of 40% biomethane is expected to fuel more than 13 million NGVs, NGVA Europe estimates. This scenario could contribute to an overall reduction in greenhouse gas emissions of 55% by 2030, according to the target set by policymakers.

1.4. Methane abatement: aftertreatment strategies

As already said, NG and biomethane are interesting alternative fuels. However, in order to exploit them, some aftertreatments strategies need to be adopted. The objective is to reduce the NO_x, CO and, in particular, unburned hydrocarbons.

Figure 1.4 plots qualitatively the emissions from an internal combustion engine versus the equivalence ratio λ, defined in Equation (1.1):

$$\lambda = \frac{AFR}{AFR^{st}} \tag{1.1}$$

With:

- λ = equivalence ratio [-];
- AFR = air-fuel ratio [-];
- AFR^{st} = stoichiometric air-fuel ratio [-];

If $\lambda < 1$ the mixture is rich, if $\lambda > 1$ the mixture is lean.

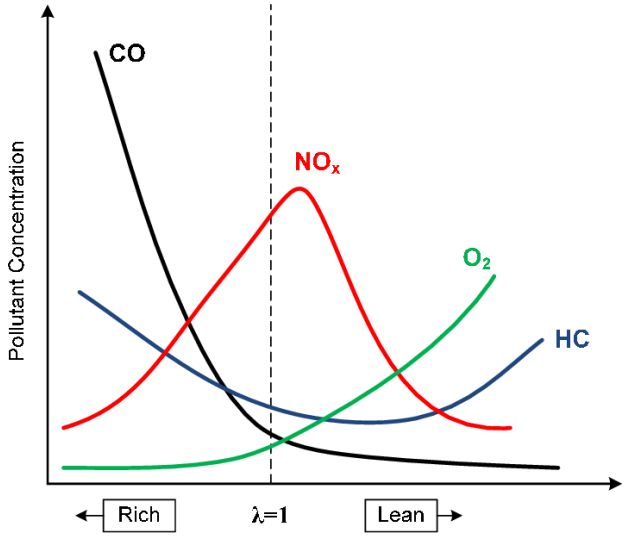

Figure 1. 4 – Typical emissions from internal combustion engines [21]

Usually, NG vehicles can work in two different conditions depending on the application. Passenger cars typically exploit a stoichiometric mixture, while heavy duty vehicles are based on lean burn engines. NGVs emission abatement systems are based principally in three components: a catalyst, an oxygen sensor (or lambda sensor) and an air-fuel ratio controller. The lambda sensor is able to evaluate the oxygen content in the exhaust system. The air-fuel ratio controller, as the name says, allows to

modulate the fuel control valve. A closed loop regulation system, schematized in Figure 1.5, is exploited. There is an engine control unit that receives information from the lambda sensor and, then, sends a signal to the fuel control valve to modulate the air-fuel ratio. When an excess of oxygen in the exhausts is evaluated the control unit opens the valve in order to feed a slightly rich mixture, while when a defect of oxygen is seen the valve is closed a bit. By this way, it is possible to run the engine in the λ window of maximum activity of the ctalytic converter.

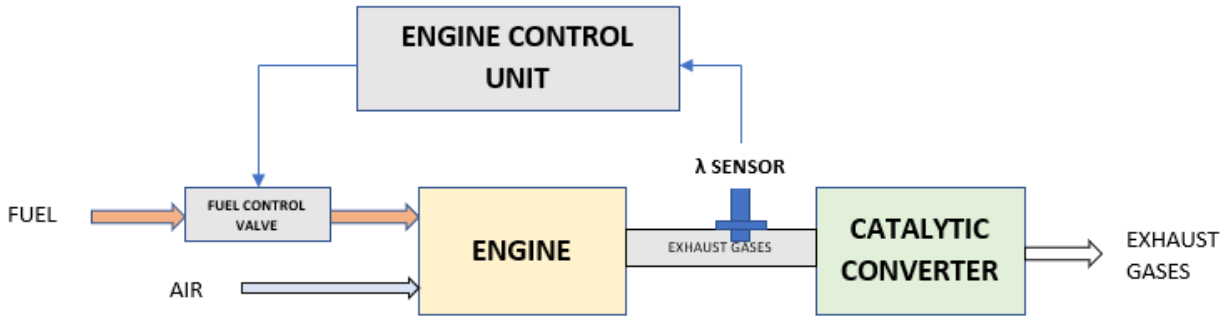

Figure 1. 5 – closed loop regulation system

1.5. Catalytic converter for NGVs

The catalytic converter in a natural gas vehicle needs to be able to purify hydrocarbons, nitrogen oxides and carbon monoxide. Based on this, the adopted technology, established in the 1970s, takes the name of three-way catalyst (TWC). The TWC converter is a well-known technology, it is also employed for the pollutant abatement of gasoline engines, where higher hydrocarbons are converted. At the low temperatures typical of the exhaust gases of the NGVs (400-500 °C) CH_4 is hard to be oxidized, due to its small molecular size and the strength of the C-H bonds. To convert it, it is necessary to reduce the activation energy of the reaction by using a catalyst. The TWC converter consists in a honeycomb monolithic matrix (Figure 1.6) composed by a high number of parallel channels, where the reactions occur. The exhaust gases from the engine pass through the channels of the monolith (also called substrate), which are covered with a washcoat. The catalyst particles, usually noble metals, are dispersed on the washcoat.

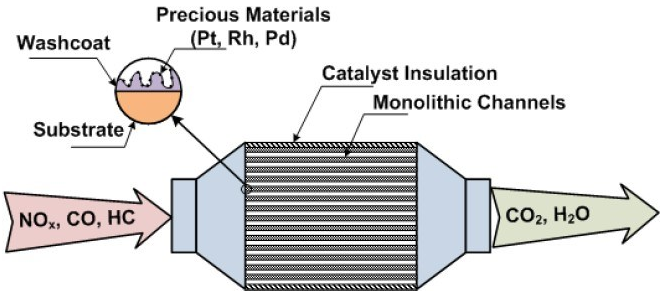

Figure 1. 6 – Monolithic catalytic converter

The operating window in terms of oxygen content at which the converter can work is quite small. As already mentioned, TWC must convert CO, NO and the unburned CH_4. Under rich conditions ($\lambda < 1$), CO and H_2 consume O_2 and reduce the NO, so a high conversion of NO is achieved, but the CH_4 is hard to be completely oxidized due to a lack of O_2. Under lean conditions ($\lambda > 1$), CH_4 conversion is easier but the NO dissociation is severely penalized. It is clear that the catalytic converter must work under approximately stoichiometric conditions ($\lambda \cong 1$).

1.5.1 Substrates

In a catalytic monolith, the substrate represents the fundamental structure. The most important characteristics of a monolith are the number of channels, their diameters and the wall thickness which determines the cell density, expressed as cells per square inch (CPSI). Typical values for commercial honeycombs ranging from 400 to 1200 cpsi. One important advantage of this structure is the large open frontal area, which results in low resistance to flow, low pressure drops and, consequently, low energy losses. Another advantage is the large contact area between the gas phase and the monolith walls, which are covered with catalyst [22]. For automotive applications, usually, ceramic and metallic monoliths are adopted. The latter are characterized by even thinner walls that provide frontal areas approaching 90%; they are used heavy-duty trucks and in some high-performance vehicles [23]. Ceramic monoliths are the most used for TWC converters, in particular a material called cordierite (2MgO 2Al2O3 5SiO2) shows excellent performances. Cordierite monoliths ensure low thermal expansion, resulting in high resistance to thermal shock damages [24].

1.5.2 Supports

The main objectives of a support, also called washcoat, are to increase the specific surface area (SSA) of the monolith and to disperse the active sites in order to enhance the catalyst activity [25]. γ-Al_2O_3 is the most widely used support for three-way-catalyst converters. It is characterized by high SSA, low chemical activity and low cost. There are other types of aluminas that can be used (θ-, δ-, κ-, η-Al_2O_3). For example, θ-

Al_2O_3, coupled with PdO catalyst, shows a high methane conversion and good performances in terms of thermal stability [26]. Depending on grain size, chemical composition or heating rate , γ-Al_2O_3 can modify its structure evolving to α-Al_2O_3 that is characterized by a lower surface area. This will result in a lower pollutants abatement. To avoid phenomena like this, some stabilization agents, called promoters, are employed to improve the alumina stability [27], [28]. It is also important to mention that γ-Al_2O_3, as all support oxides, is characterized by acid/base properties that can influence the noble metals catalytic activity for methane conversion [29].

1.5.3 Promoters

Promoters are added to increase the performances of the TWC converters, particularly for Pd-based catalysts. They usually are alkali metals (Mg, Ca, Ba, etc.), rare earths (La, Ce, Y, etc.) and transition metals (Mn, Fe, Co, Ni, etc.). More in detail, they can increase the catalytic activity at low temperatures and improve the hydrothermal stability of the catalyst at high temperatures [30]. The promoter usually adopted in commercial TWC converters is a mixed solid-state solution composed by CeO2-ZrO2. CZ oxides as promoter have several advantages:

- Promote the noble metal dispersion;
- Increase the stability of the support;
- Increase the catalytic activity of the methane oxidation;
- Promote WGS and SR reactions;
- Improve the oxygen storage capability (OSC), reducing problems during cold start;

If we are using Pd as a catalyst, CZ doping has also a positive effect on the Pd/PdO distribution, so we obtain a more stable PdO_x catalyst during the reaction. CZ oxides also enlarge the λ-window at which the converter can work, due to the presence of the lattice oxygen. When a lean feed is passing through the monolith, the oxygen is stored thanks to the presence of the cerium oxide, while under slightly rich conditions the oxygen previously stored is released [31]. Barium is also a promoter that can be used for NGVs applications. It has been showed that it increases the hydrothermal stability of Pd-based catalysts [32]. TiO_2 is considered an interesting solution at low temperatures: the addition of titania increases the oxygen mobility resulting in a higher O_2 availability at the catalyst surface, thus enhancing the catalytic activity [33]. Rare earths, such as Yttrium, have been studied as promoters and appear to be able to significantly improve Pd dispersion, increasing the effective area available for reactions [34].

1.5.4 Noble metal catalysts

Noble metal catalysts are widely used and studied, due to their high catalytic activity at low temperatures. Pd and Pt are considered the best option for the methane oxidation [35], [36].

Pd-based catalysts

Palladium based catalysts are considered the most active materials for methane oxidation under lean-burn conditions. The behaviour of this catalyst is quite complex, in fact depending on the operating conditions (temperature, oxygen partial pressure and particle dispersion) different species of PdO can be formed [37]. Pd and PdO coexist on the catalyst surface, and this has a strong influence on methane oxidation. Over PdO the reaction takes place through a Mars-van Krevelen redox mechanism: the oxide is reduced to metallic Palladium providing lattice oxygen to gas-phase methane. Then, PdO is formed again thanks to gas-phase oxygen [38]. Over metallic Pd, a Langmuir-Hinshelwood mechanism is believed to control the reaction [39]. In a (L-H) reaction mechanism, the surface adsorption reaction, which must be the rate-determining step, sees two different species competing to be adsorbed at the same sites. These complex mechanisms, due to the coexistence of Pd and PdO, are not yet completely elucidated and certainly need further study to be fully understood.

Pd based catalyst are characterized by two main drawbacks: deactivation from water poisoning and sensitivity to sulfur-containing compounds. As regarding the former, water tends to create stable surface hydroxides that inhibit the active sites [40], [41]. As far as sulphur poisoning is concerned, a strong influence is given by the type of substrate used: if a sulfating material (e.g. Al_2O_3) is used, deactivation is less because the substrate acts as a sink for SO_2/SO_3, protecting the active sites [42].

Some studies have shown that the addition of Rh in the catalyst formulation increases NO_x conversion [43], [44].

Pt-based catalysts

Platinum based catalysts, which proved to be more effective for the combustion of higher alkanes, are characterized by a lower methane conversion compared to Pd-based ones [45]. This difference is strongly accentuated when an excess of O_2 is fed: Pt-based catalysts are highly susceptible to oxygen poisoning due to the competitive adsorption of CH_4 and O_2, which in this case is unbalanced in favour of the latter. As a result, less methane is able to reach the active sites and this reduces the CH_4 conversion [46]. An advantage of Pt-based catalysts is that, unlike Pd-based ones, they are very resistant to water and sulfur poisoning [47].

Good performances of bimetallic and trimetallic catalysts has also been recognized, making Pd-Pt catalysts interesting for NGVs application [48], [49].

1.5.5 Noble metal-free catalyst

Noble metal catalysts are not the only possible choice for methane oxidation. Some problems associated with their exploitation, such as the high price of active

components and the environmental impact of extraction, encourage research into more sustainable and less expensive solutions.

Spinel-type oxides (general formula AB_2O_4) are interesting as alternative for NGVs aftertreatments because of their stable crystal structure and high thermal resistance. Among these, Co_3O_4 is one of the most promising: it shows good catalytic activity for CH_4 and CO oxidation reaction, due to the abundance of oxygen vacancies on its surface [50]. The conversion of CH_4 can be improved by adding, for example, Ti, Zr or Mg in the catalyst formulation. More generally, Ni and Co oxides individually exhibit good methane conversions, but Ni/Co mixed oxides (NiCo2O4) show even higher performances [51].

The perovskite-type oxides (general formula ABO_3), composed of alkaline or rare earth elements and transition metals, are characterised by a stable structure, good thermal stability and a low tendency to agglomeration of the active phase [52]. For these reasons, they are considered attractive for NGVs.

1.6. Objective of the work

In this work, the performances of a commercial Pd-Rh/Al_2O_3 catalyst were tested in a wide range of different conditions. Experiments were carried out varying the feed composition and the reaction temperature, in order to better understand the behaviour of the catalyst towards the conversion of methane. The focus of the experimental activity was on the measurement of concentration and temperature profiles, which were obtained by means of the spatially resolved sampling technique. Collected data allowed to hypothesise the effect of temperature, water poisoning and fuel type on the activity of the Pd-based catalyst.

2 Experimental methods

In this chapter, the experimental setup used for the thesis work is described. A definition of the procedures and methods followed to carry out the tests is also provided.

2.1. Catalytic test rig

The tests described in the next chapter were conducted on the rig represented in Figure 2.1 and schematized in Figure 2.2, under fume hood.

Three main sections can be identified:

- Feed section;
- Reaction section;
- Analysis section;

During all the activities, lines and instrumentation are kept at controlled temperature levels mainly to avoid condensation phenomena, which are likely to happen given the consistent amount of water fed. For this purpose, heating tapes are employed (highlighted in red in theP&ID – Figure 2.2).

The rig components kept at controlled temperature are:

- Reactor inlet line – $T_{setpoint}$ = 150 °C
- Reactor outlet line – $T_{setpoint}$ = 135 °C
- Evaporator – $T_{setpoint}$ = 160 °C
- Hygrometer – $T_{setpoint}$ = 120 °C
- Mass spectrometer – $T_{setpoint}$ = 70 °C
- Mass spectrometer inlet capillary – $T_{setpoint}$ = 170 °C

Regarding the first three of the list, temperature readings are obtained from thermocouples thanks to a National instrument data acquisition module connected to "DAQExpress" software.

Figure 2. 1 – Experimental rig

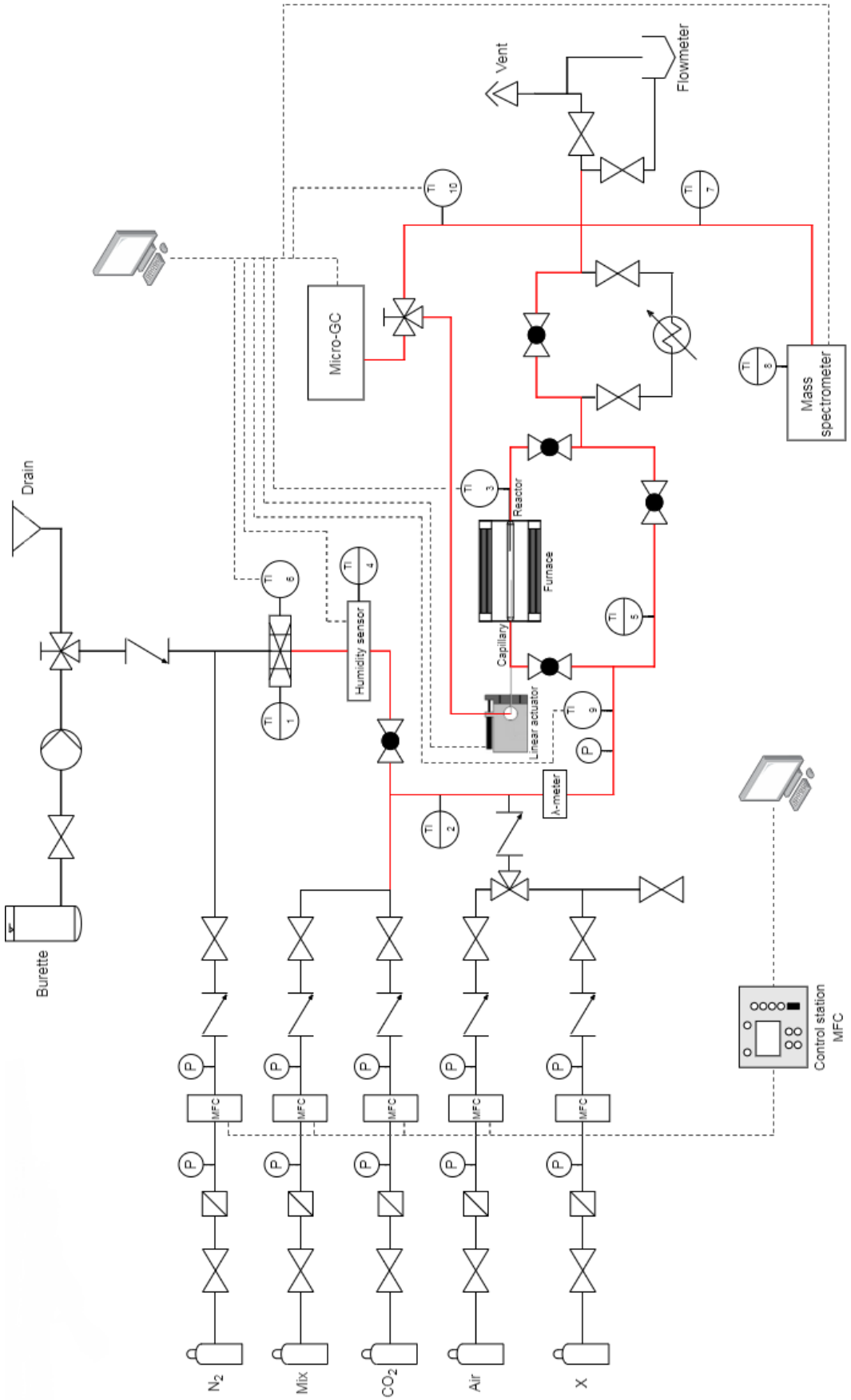

Figure 2. 2 – Experimental rig P&ID, red lines indicate heated tapes

2.1.1 Feed section

The feed section consists of six lines that carry the reactants employed in the experiments. Four of them allow to connect cylinders located outside the laboratory with the reaction section, while line named "X" in the process flow diagram could be potentially used in synergy with a Burkert 1078 valve to switch between the adopted air stream and a different one. Lastly, water is provided from a 25 mL burette located under the hood.

Table 2. 1 – Cylinders composition

Cylinder	Composition	Concentration [vol%]
Nitrogen	N_2	100%
Mixture 1	H_2	1.97%
	CH_4	2.97%
	CO	11.8%
	N_2	Balance
Mixture 2	CH_4	20%
	N_2	80%
Carbon dioxide	CO_2	100%
Air	O_2	21%
	N_2	79%

Each of the lines providing gases is equipped with:

- 1/4-inch stainless steel piping;
- Shut off valves;
- Bourdon spring pressure gauges (6 bar scale);
- A metal mesh filter, so that impurities in the gases do not damage the instrumentation;
- A Brooks mass flow controller;
- A non-return valve;

Mass flow controllers

Mass flow controllers located on feed lines are Brooks Instrument MFCs (Figure 2.3); the full scales of the MFC employed for the campaigns conducted during this work are summarized in Table 2.2:

Table 2. 2 – MFC full scales

Line	Nominal Flux [NmL/min]
Nitrogen	3000
Mixture 1	200
Mixture 2	50
Carbon dioxide	1000
Air	200

Nitrogen is stored as a liquid in a tank located outside the laboratories, near the entrance of the building. The remaining compounds are stored in cylinders on the balconies next to the labs. Pressure inside containers is obviously very high and it is reduced before getting into the plant by means of pressure reducers, mounted on the walls. In this way pressure goes from more than 150 bar to 5 bar.
All the MFC are connected to a Brooks 0154 control unit (Figure 2.3) which can be operated from the laboratory PC thanks to Brooks "SmartDDE" software.

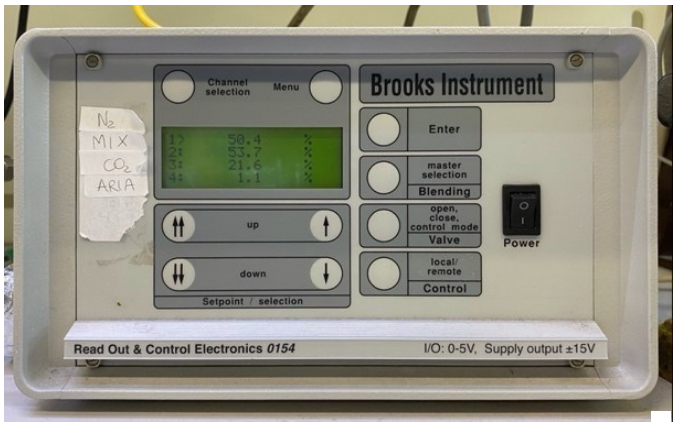

Figure 2. 3 – Brooks 0154 control unit

Figure 2. 4 – Brooks mass flow controller

To properly operate the controllers, a calibration was performed: a linear trend between the opening degree of the MFC and the corresponding flow rate could be established. Starting from the nominal flow rate of the Brooks MFC, a set of appropriate opening values in the range of the desired component flow rate is chosen; then, the corresponding fluxes are measured using a bubble flow meter connected to the vent and a stopwatch. These points allow to perform a linear regression to obtain the required calibration line, as reported in Figure 2.5. Its equation is used to compute a first guess opening degree value starting from a desired flow rate.

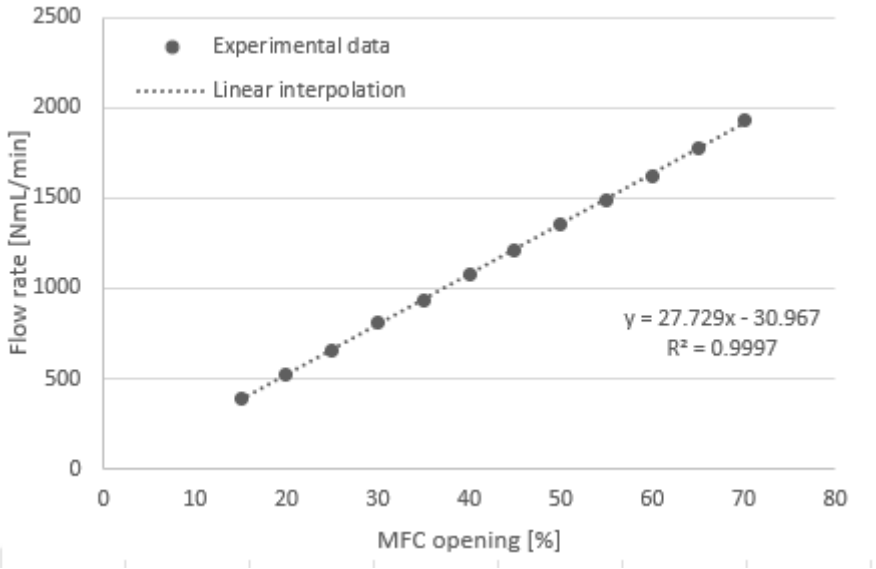

Figure 2. 5 – N2 Brooks MFC calibration line

Water pump

The water, drawn from a burette, is fed to the evaporator via a Gilson 305 piston pump, shown in Figure 2.6. The 5SC pump head has a full scale of 5 mL/min; the water needed during experiments is much lower, so the Gilson 305 head is equipped with a "Microflow" plug, which reduces the maximum liquid flow to 0.5 mL/min. The numerical keypad on the front is used to choose the actual set point, directly inserting the desired flow. A "Prime" option, activated by pressing the prime button on the keypad, is available to operate the pump at its maximum flux.

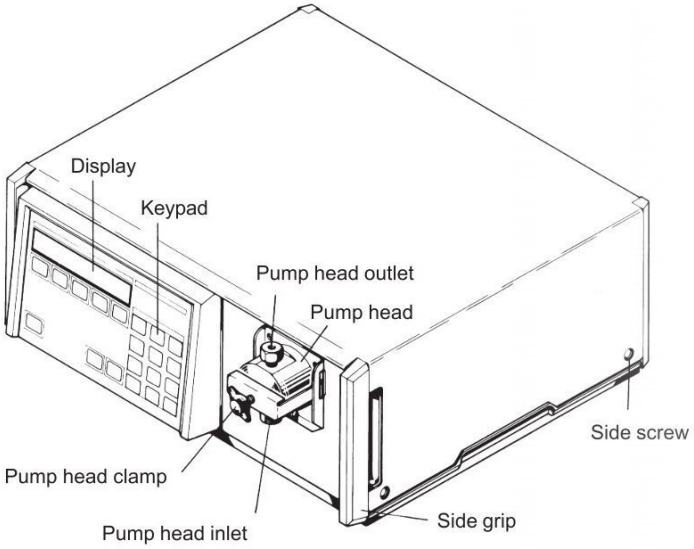

Figure 2. 6 – Gilson 305 piston pump

Once decided the percentage of water in the feed stream, it is possible to evaluate the H_2O gaseous flow rate. To compute the liquid flow rate to be set on the pump, the following correlation is used:

$$\dot{Q}_{H_2O,liq} = \dot{Q}_{H_2O,gas} \cdot \frac{p \cdot MW_{H_2O}}{\rho_{H_2O,liq} \cdot R \cdot T} \tag{2. 1}$$

With:

- $\dot{Q}_{H_2O,liq}$ = volumetric flow rate provided by the pump [mL/min] ;
- $\dot{Q}_{H_2O,gas}$ = water vapour flow rate in the reactants [NmL/min] ;
- MW_{H_2O} = water molecular weight [g/mol] ;
- $\rho_{H_2O,liq}$ = water density at ambient conditions [g/mL] ;
- R = 8.314 J/(mol·K) ;
- T = 273.15 K ;
- p = 101325 Pa ;

Evaporator

The water is fed through a 1/16-inch steal line and is mixed with the nitrogen flow in a three-way fitting. A non-return valve is mounted on the liquid side, to avoid N_2 backflow. Then the two-phase mixture, composed by H_2O and N_2, is supplied to the evaporator to obtain the complete evaporation of the water. The evaporator is based on the electrical heating of aluminium plates, its temperature is kept at 160 °C. A K-type thermocouple is mounted to check the temperature. To avoid thermal losses, the system is wrapped in glass wool and covered by aluminium foil.

Humidity sensor

Downstream the evaporator, a Vaisala HUMICAPP – HMT334 humidity sensor is installed. The sensor consists of a glass substrate on which a thin film of polymer is deposited between two conductive electrodes. The unit is covered by a metal electrode to avoid damages due to contamination and moisture.

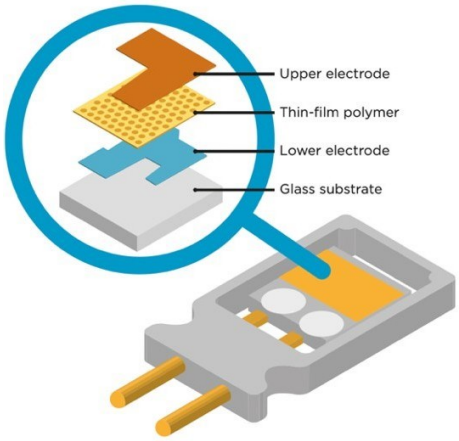

Figure 2. 7 – Vaisala HUMICAPP-HMT334 sensor

The polymeric film is able to absorb or release water vapour when the feed stream relative humidity changes. The amount of water absorbed has an influence on the dielectric properties of the polymer, for this reason a change in humidity causes a variation of the sensor capacitance. The sensor is connected to National Instrument data acquisition system (NI cDAQ-9174) so that we can read the value of the output voltage on the DAQExpress software.

Also in this case, a calibration is needed to correlate the amount of water fed through the pump with the output voltage given by the humidity sensor. A nitrogen flow representative of the typical conditions is chosen; then the pump is set at different opening values to obtain different moisture fractions. The oscillating signal of the hygrometer is recorded for a few minutes and then a mean output voltage can be

calculated. Using the Equation 2.1, the value of the liquid flow rate fed with the pump can be converted into the respective vapour flux so that the moisture fraction in the water-nitrogen mixture can be evaluated. As already done for Brooks MFCs, a linear trend is plotted to evaluate the correspondence of the pump set point with the water content in the feed.

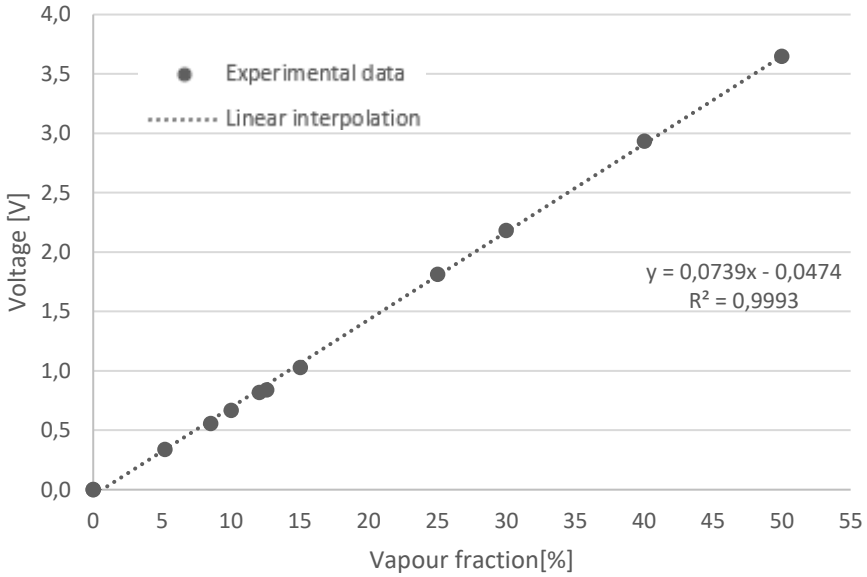

Figure 2. 8 – Humidity sensor calibration line

Oxygen sensor

A Bosh LSU 4.9 wideband lambda sensor (Figure 2.9) is placed upstream the reaction section, once all the individual flows are mixed in 1/8-inch lines, to monitor the lambda value before entering in the reactor.

Figure 2. 9 – Bosch LSU 4.9 lambda sensor

The lambda sensor operation is based on the working principle of a Nernst cell. It is composed by two Pt catalytic electrodes, separated by the Zirconia solid electrolyte; one electrode is exposed to exhaust gases while the other is surrounded by ambient air, which is used as reference for the O_2 concentration ($y_{O_2}^{air}$~21%).

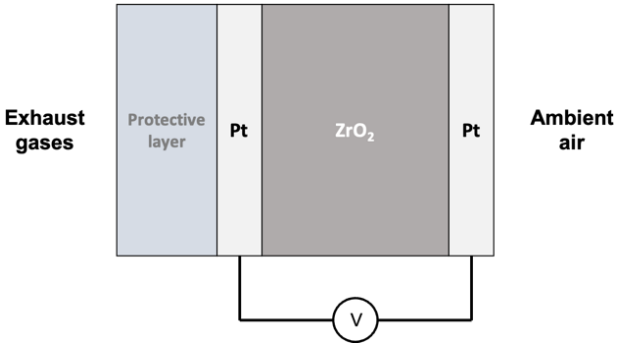

Figure 2. 10 – Lambda sensor Nernst cell scheme

On the flue gas side, a porous ceramic layer protects the Pt electrode from gas contamination and erosion. The equilibrium O_2 concentration of the electrolyte is strongly influenced by the surface reactions occurring on the left electrode.

Anodic processes, i.e. oxidation reactions, occur on the left Pt electrode, according to equation (2.2):

$$2O^{2-} \rightarrow O_2 + 4e^- \tag{2. 2}$$

On the right electrode, the reduction reaction reported in Equation (2.3) takes place:

$$O_2 + 4e^- \rightarrow 2O^{2-} \tag{2. 3}$$

A stream of electrons is established from the left Pt electrode (anode) to the right Pt electrode (cathode), through an external circuit. To balance the electrons motion, the oxygen ions move across the ZrO_2 element. In order to increase the electrolyte temperature and enhance its permeability to ions, a heating element is often added to the lambda sensor.

Figure 2.11 shows the signal of a narrowband oxygen sensor. Assuming constant oxygen concentration in the reference air, the output voltage is influenced by the O_2

concentration in the exhausts. When $\lambda < 1$, the low O_2 content in the exhausts leads to a significant difference with respect to the reference air, in terms of oxygen fraction. This difference results in a high output voltage. When $\lambda > 1$, the oxygen concentration does not change too much across the electrolyte and the output voltage is quite low.

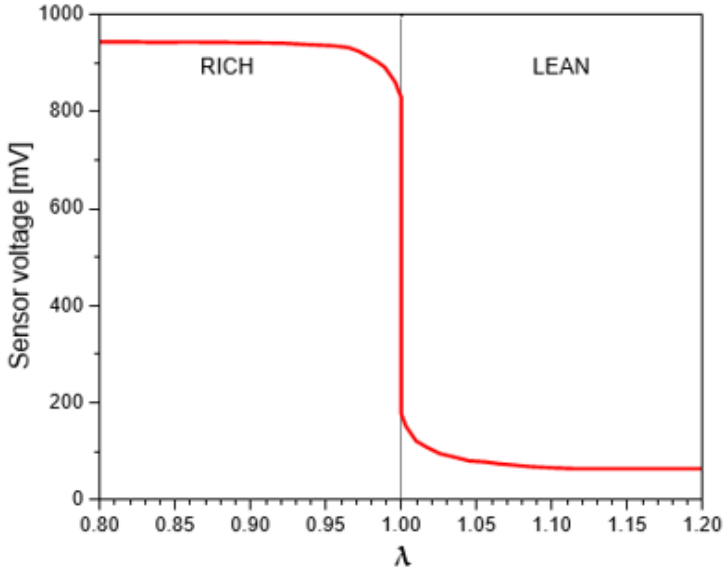

Figure 2. 11 – Narrowband lambda sensor output

The reason of the steep trend close to the stoichiometric limit is to be found in the difference between unreacted and equilibrium oxygen concentration. The sensor responds to the equilibrium oxygen concentration, which is the result of the reaction occurring at the anode, previously mentioned. This means that the output voltage is not representative of the real free oxygen concentration, that varies approximately linearly with λ around stoichiometric conditions.

The lambda sensor mounted on the rig is a wideband oxygen sensor, instead a narrowband one. The main difference between the two sensors is in the output signal, a wideband probe gives as result a monotonic output ranging from 0.65 to infinity, that guarantee a higher accuracy in the λ value estimation. This is possible because of the presence of a so-called "pumping cell".

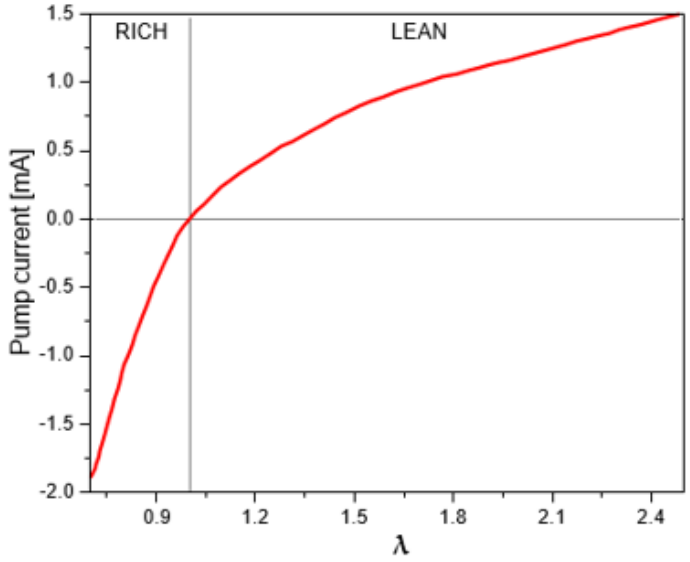

Figure 2. 12 – Wideband lambda sensor output

As showed in Figure 2.13, in a wideband sensor the Nernst cell is exposed to the reference air on one side and to a monitor chamber on the other. In the monitor chamber, by means of the pumping cell, the oxygen is kept constant at a concentration that guarantee a λ value equal to 1, which translates into an output voltage of the Nernst cell equal to 450 mV. The pumping cell can transport oxygen into and out of the monitor chamber to maintain constant the Nernst cell output voltage. The current flow across the pumping cell in now the indicator used to monitor the λ value.

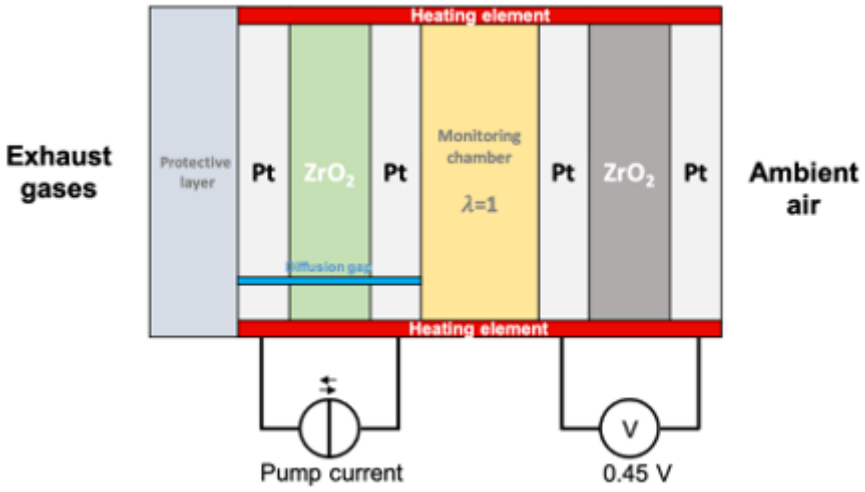

Figure 2. 13 – Wideband lambda sensor scheme

The output signal is processed by an ETAS LA4 Lambda Meter (Figure 2.14), it uses fuel-specific curves to determine and display the lambda value.

Figure 2. 14 – ETAS LA4 Lambda Meter

2.1.2 Reaction section

The pollutant abatement takes place in a stainless-steel tubular reactor, which contains the catalyst. To sustain the reaction temperature, the reactor is inserted in an oven. A reactor bypass line is present, useful to analyse the feed stream.

Catalytic materials

In this work, a commercial 400 CPSI honeycomb Pd-Rh catalyst (Figure 2.15), manufactured by Ecocat, was tested. The support consists of γ-Al_2O_3, with a 7.1 g/L loading of Pd-Rh (Pd:Rh-39:1). Cerium/zirconium mixed oxides are present in the formulation, to increase the oxygen storage capacity (OSC) and the oxygen mobility.

Square samples (6x6 channels) were cut from the monolith core to prevent the influence of dusting phenomena, possibly occurred on the most exposed parts, which could have affected the activity of the material.

Figure 2. 15 – Ecocat honeycomb monolith

Figure 2.16 shows the geometrical structure of the honeycomb material, highlighting some dimensions of interest.

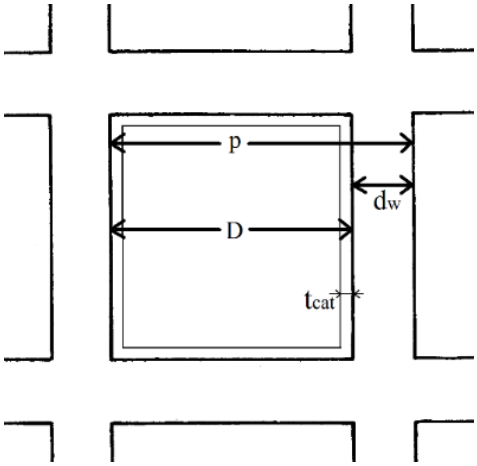

Figure 2. 16 – Honeycomb monolith geometrical structure

From direct evaluation of the samples the following measurements are obtained:

- t_{cat} = 0.0025 cm (catalyst thickness on the support);
- d_w = 0.0222 cm (support thickness);
- S_{mon} = 0.789 cm (side of the monolith square frontal section);

There are other important quantities that can be calculated, to define the characteristics of the catalytic sample:

$$Pitch = \frac{2.54}{\sqrt{CPSI}} = 0.1270\ cm \tag{2. 4}$$

$$D = Pitch - d_w = 0.1048\ cm \tag{2. 5}$$

$$D_{h,ch} = D - 2t_{cat} = 0.09980\ cm \tag{2. 6}$$

$$\varepsilon = \frac{D_{h,ch}^2}{Pitch^2} = 0.6175 \tag{2. 7}$$

$$A_{eq} = S_{mon}^2 = 0.6150\ cm^2$$

(2. 8)

With:

- $Pitch$ = sum of the cordierite thickness d_w and channel side D [cm] ;
- $D_{h,ch}$ = length representative of the actual area available for the flow [cm] ;
- ε = void fraction [-] ;
- A_{eq} = equivalent cross section area [cm^2] ;

Reactor

As already mentioned, a stainless-steel tubular reactor (L=38.5 cm, ID=1.63 cm) has been used to carry out the experiments. In Figure 2.17 it is possible to see the section of the reactor when the catalyst is mounted. Starting from the left, a first holder containing a 2 cm long Fecralloy foam is placed. Thanks to its randomly porous structure, the axial mixing of the feed stream is enhanced to obtain a better reactants distribution. Subsequently, a second steel holder 12.8 cm long is inserted: here the Ecocat sample is placed in a precise position.

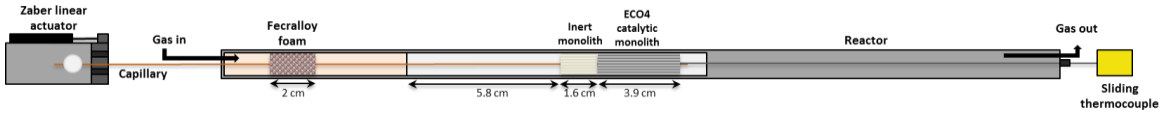

Figure 2. 17 – Reactor loading configuration

The catalyst sample is a 6x6 channels monolith honeycomb, 3.9 cm long, with a volume equal to 2.496 cm^3. Right before entering the catalyst, the feed stream pass through an inert cordierite honeycomb monolith (L=1.6 cm) which serves as guide for the sampling capillary. In fact, due to its high length and low diameter, the capillary tends to bend. It is worth to underline that the measurements right before the monolith inlet could be affected by an interaction with the holder walls.

The monolith is wrapped in a fibrous quartz wool tape to avoid unwanted sliding of the catalyst and bypass phenomena, that could affect the conversion measured. The position of the catalyst in the reactor has been chosen to keep the temperature as constant as possible along its axis, considering the heat of reactions and the thermal losses of the oven. The void space between the inlet of the second holder and the inert monolith (L=5.8 cm) was consequently computed.

A K-type thermocouple (L=50 cm, OD=0.5 mm) is slid 28.5 cm in from the rear of the reactor to monitor the temperature in correspondence of the catalyst outlet.

Oven

The reactor is inserted in a Carbolite oven placed horizontally under the hood; it is 30 cm long and features a 2.5 cm internal diameter. The oven temperature can be controlled thanks to a Eurotherm 2132 controller. It uses PID (Proportional Integral Derivative) error correction systems to maintain the temperature constant in time, at the desired value.

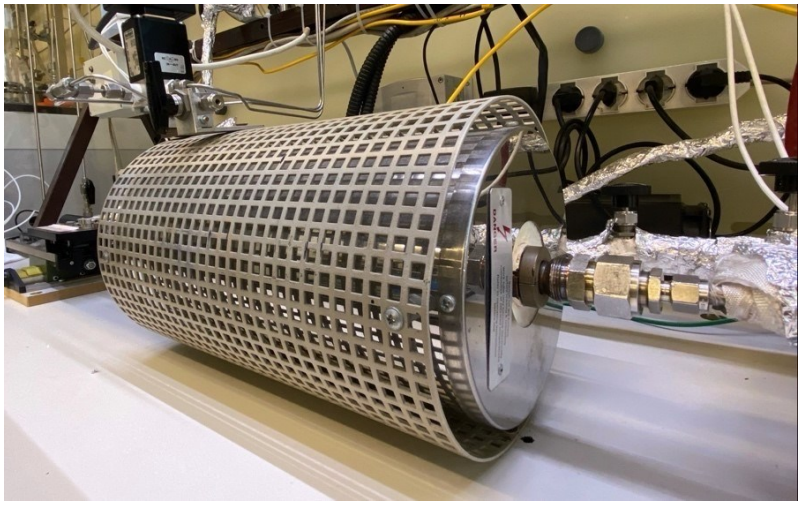

Figure 2. 18 – Furnace with reactor inserted

The inlet part of the reactor, that remains outside the oven, is covered in glass wool and aluminum tape; at the outlet side of the reactor, iron supports are mounted to fit the gap between the oven walls and the tubular reactor. This is to prevent convective heat transfer losses and help the system in achieving the temperature set point.

In Figure 2. 19 the temperature profile of the oven is represented. To obtain this curve the operative temperature of the oven has been set from the controller and a nitrogen flow rate equal to the one carried out during the experiments was sent through the reactor. An inert monolith is placed instead the catalyst to consider the sample thermal resistance. To register the temperature profile, a sliding thermocouple is inserted from the exit of the reactor and placed in correspondence of the inlet; then, the TC is moved back with a 0.5 cm axial displacement and the temperature is continuously recorded thanks to “DAQExpress” software.

The catalyst position has been chosen according to the coordinate where the difference between the recorded real temperature and the actual set point reaches its minimum.

It is important to notice that, due to heat transfer phenomena, the isothermal position of the reactor may vary depending on the total flow rate and the set point temperature of the oven.

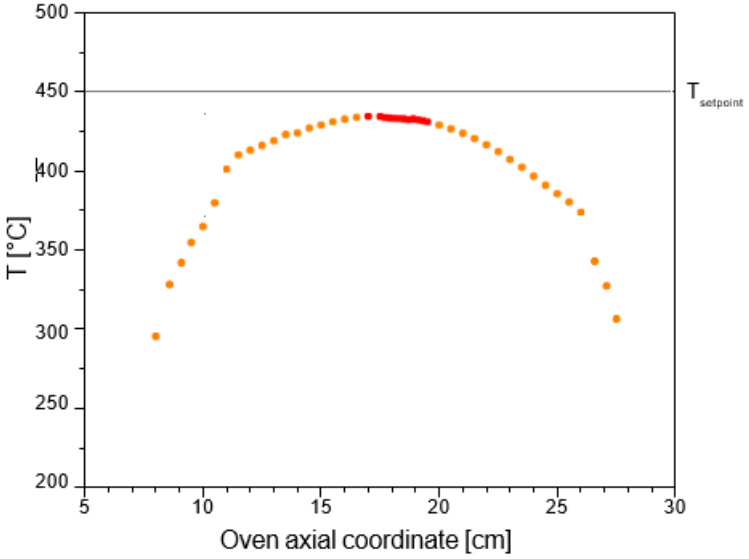

Figure 2. 19 – Oven temperature profile ($T_{setpoint}$ = 450 °C)

Condenser

Moisture removal is crucial to avoid damages to the mass spectrometer filaments and saturation of the micro-GC columns. To accomplish this task, a SCC-C Sample Gas Cooler is placed downstream the reactor, connected with 1/4-inch pipelines.

Here, the gaseous stream is cooled to 3 °C and almost 100% of the water is condensed and separated from the products, the condensate is collected in a container outside the hood. A bypass line has been installed for each time the plant is switched off or when dry samples need to be analysed. The amount of product gases dissolved in the condensate was considered negligible.

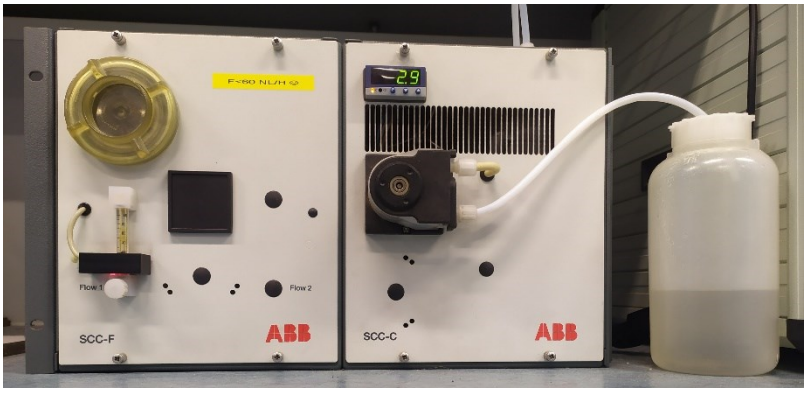

Figure 2. 20 – SCC-C Sample Gas Cooler

2.1.3 Analysis section

The analysis section of the plant consists in:

- A micro gas chromatograph;
- A mass spectrometer;

The former has been used to evaluate the feed, the downstream products composition and, thanks to a capillary inserted in the monolith, the axial concentration profiles.

The latter allows to monitor continuously the downstream performances of the catalyst, having feedback in real time of what happens in the monolith.

Spatially resolved sampling technique

In this study, the spatial solved technique, introduced by Horn et al. [46], has been employed to measure temperature and composition along the reactor axial coordinate.

Concentration profiles

The concentration profiles are collected employing an Agilent quartz capillary coated by polyimide; it is a deactivated silica capillary tubing with an inner diameter equal to 0.2 mm and an outer diameter of 0.36 mm. The material it is made is chemically inert and ensures small heat losses, this is important because we want to reduce as possible the impact of the capillary on the results.

One open extremity is inserted in one of the four central channels, both of the inert and the monolith; the other one is connected, through a heated steel line, to the micro-GC so that it can analyse the gas composition at the different coordinates. To connect the micro gas chromatograph line and the capillary, a Valco fused silica adapter has been used. It consists of a liner, sliding over the capillary, and a ferrule that is assembled from the top of the liner (Figure 2. 21). A nut captures both the liner and the ferrule, then the assembled adapter is screwed in the union body, which is fixed on the top of the Zaber stage. The micro-GC line is connected to the other side of the union body, as showed in Figure 2.22.

Figure 2. 21 – Vici fitting assembly

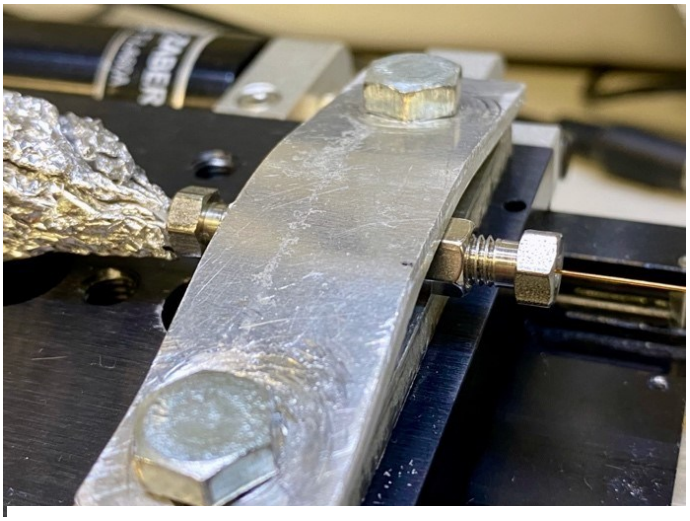

Figure 2. 22 – Connection between micro-GC line and capillary

A motorized Zaber Technologies T-LA60A linear actuator is adopted to move the capillary among the monolith axis. It features a 0.09921875 μm default resolution and a 60 mm travel range, controlled via dedicated software.

By measuring the length of the visible capillary and knowing the total one, it is easy to calculate the position of the sampling tip within the reactor. Therefore, once the moving stage is operated it is possible to associate every step with a sampling coordinate and build the concentration profile along the monolith axis. It is recommended to keep the exposed part of the capillary as short as possible to avoid condensation phenomena.

Temperature profiles

Gas phase temperature profiles are acquired thanks to a K-type thermocouple (OD=0.25 mm) inside a quartz capillary (ID=0.53mm; OD=0.67mm). The capillary used for temperature acquisition is sealed at one end using an oxyacetylene torch, this is in order to avoid gas leakages from the reaction zone. To place the thermocouple in the correct position within the reactor, the same technique is used as for the concentration profiles. In Figure 2.23, it can be seen that a different adapter is used to fix the capillary, in which the thermocouple is inserted, to the linear stage.

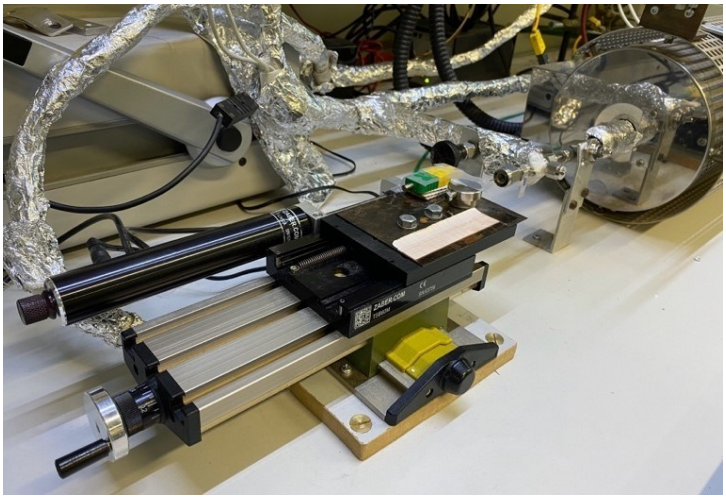

Figure 2. 23 – Temperature profile acquisition setup

Micro gas chromatograph

An Agilent 3000A micro-GC is employed to analyse the gas samples. Thanks to a three-way valve, as in Figure 2.24, the micro-GC can process gas samples from both downstream the reactor, or the oven bypass line if needed, or the capillary to obtain the concentration profiles along the monolith. A filter was fitted to prevent the possible effects of excessive moisture content in the aspirated gases.

Figure 2. 24 – Agilent 300A micro-GC filter, sampling line and three-way valve

The micro-GC is equipped with two different capillary columns, each one is able to evaluate a specific set of chemical species. The molecular sieve column separates H_2, O_2, CH_4 and CO, using argon as carrier gas. The PLOTQ column uses helium as carrier to evaluate the so called "Macro" - it comprises oxygen, nitrogen, and carbon monoxide in a single peak – CH_4, CO_2 and H_2O.

Channel A displays the peaks obtained with the molecular sieve column, while channel B refers to U-plot one.

Table 2. 3 – Agilent 3000A micro-GC columns specifications

	Molsieve	**PLOTQ**
Length [m]	10	8
Film thickness [μm]	12	10
Internal diameter [μm]	320	320
Carrier gas	Ar	He

The difference between a micro-GC and a conventional one is the size, as the name suggests, and this allows a higher speed of the analyses. When the sampled mixture components move thorough a separation column of the micro-GC, due to the different affinity with the solid phase lining the column, they exit at different times. The higher is the affinity with the column coating, the higher is the gas displacement velocity, which is also influenced by pressure and temperature. The separated species are subsequently analysed thanks to a TCD (Thermal Conductivity Detector), which uses a Wheatstone bridge circuit. There are four resistors, one is in contact with the column effluent stream, while another one is invested by a reference flow. Each of the sampled species has a different thermal conductivity with respect to the carrier gas, resulting in a change in electrical resistance and thus an output voltage signal. Then, a chromatogram is obtained for each column: the TCD signal is plotted as a function of time. The process ideally leads to Gaussian-shaped peaks, each representing a specific compound with its residence time in the column. Of course, the narrower the peak, the higher the separation efficiency of the system.

The chromatograms need to be managed to convert the areas between the peaks and the baseline into fluxes and concentrations.

The major part of the water vapour content in the product stream is condensed and removed, thanks to the condenser already described. Therefore, to account for the water content in the composition, the pump setpoint is corrected in combination with the hydrogen conservation balance:

$$\dot{Q}_{H_2O}^{out} = \dot{Q}_{H_2O}^{in} - 2 \cdot \Delta\dot{Q}_{CH_4} - \Delta\dot{Q}_{H_2} \tag{2. 9}$$

With:

- $\dot{Q}_{H_2O}^{out}$ = reactor outlet water volumetric flow rate [Nml/min] ;
- $\dot{Q}_{H_2O}^{in}$ = reactor inlet water volumetric flow rate [Nml/min] ;
- $\Delta\dot{Q}_{CH_4} = \dot{Q}_{CH_4}^{out} - \dot{Q}_{CH_4}^{in}$ [Nml/min] ;
- $\Delta\dot{Q}_{H_2} = \dot{Q}_{H_2}^{out} - \dot{Q}_{H_2}^{in}$ [Nml/min] ;

To avoid the interference of unwanted species, the carrier streams are purified with the help of a filter and oxygen trap mounted before the micro-GC inlet. In this way, practically pure He and Ar are sent to the columns.

Three different sets of micro-GC parameters have been used for this work. The first method, called "CPO Metano", is used during the analysis of the samples; the parameters are showed in Figure 2.25:

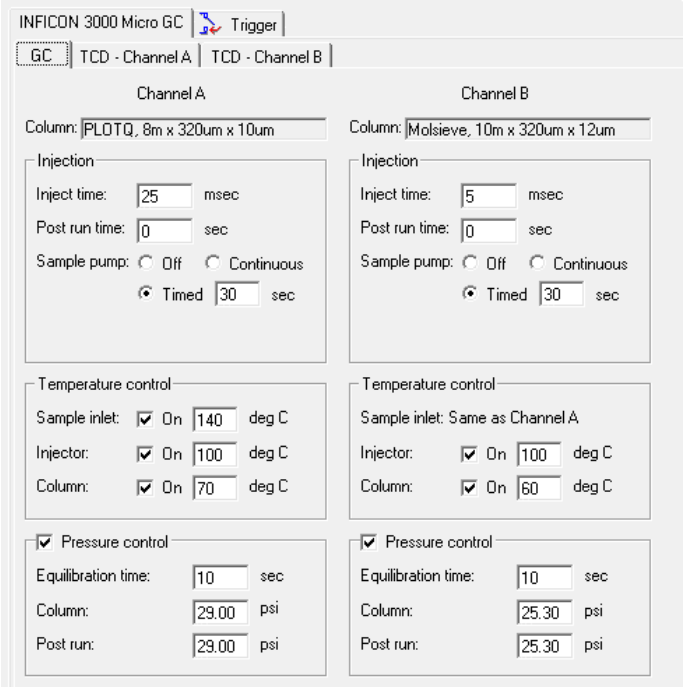

Figure 2. 25 – "CPO Metano" method parameters for columns A and B

The second method implemented, called "Spegnimento", is described in Figure 2.26. It sets the injection and columns temperature at low values; it is used overnights and whenever the micro-GC needed to be shut off.

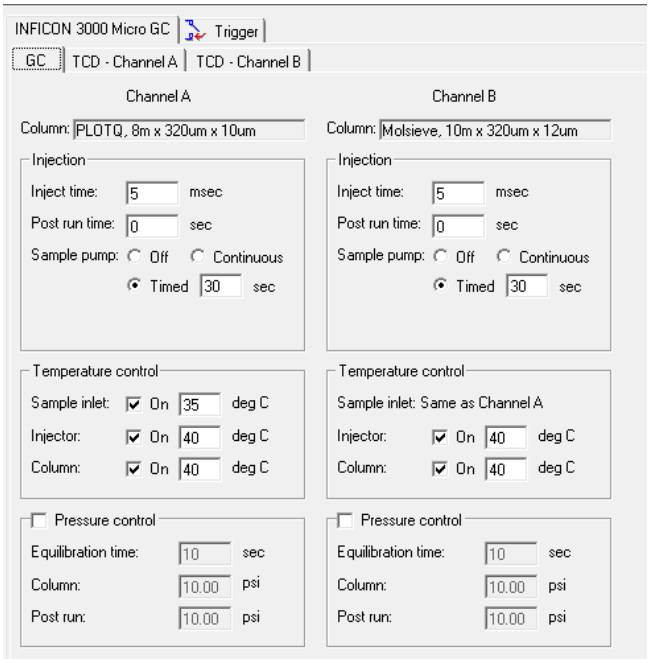

Figure 2. 26 – "Spegnimento" method parameters for columns A and B

The last method, whose parameters are represented in Figure 2.27, is "Condizionamento". It increases micro-GC temperatures to purify the columns from possible residues and prevent water saturation, this is important because the samples from the capillary do not pass through the condenser. The "Condizionamento" method was applied once a week for 13 hours.

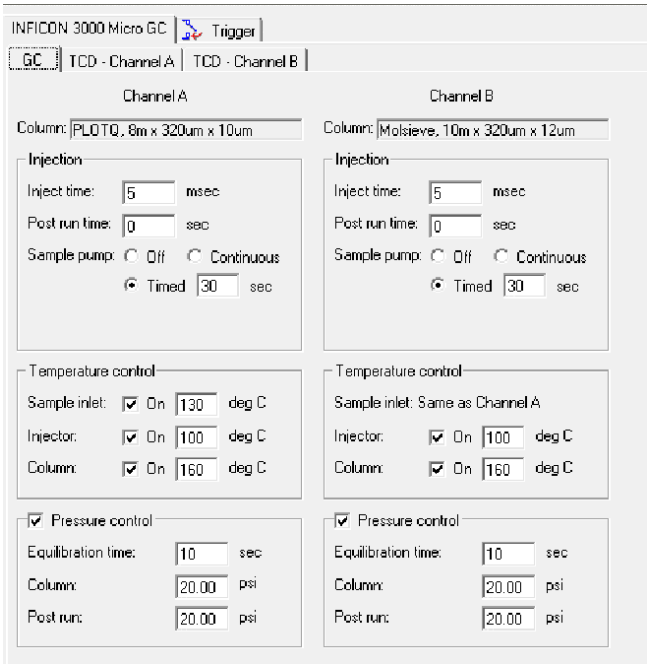

Figure 2. 27 – "Condizionamento" method parameters for columns A and B

Sample chromatograms are reported in Figure 2.28 and Figure 2.29, by way of example:

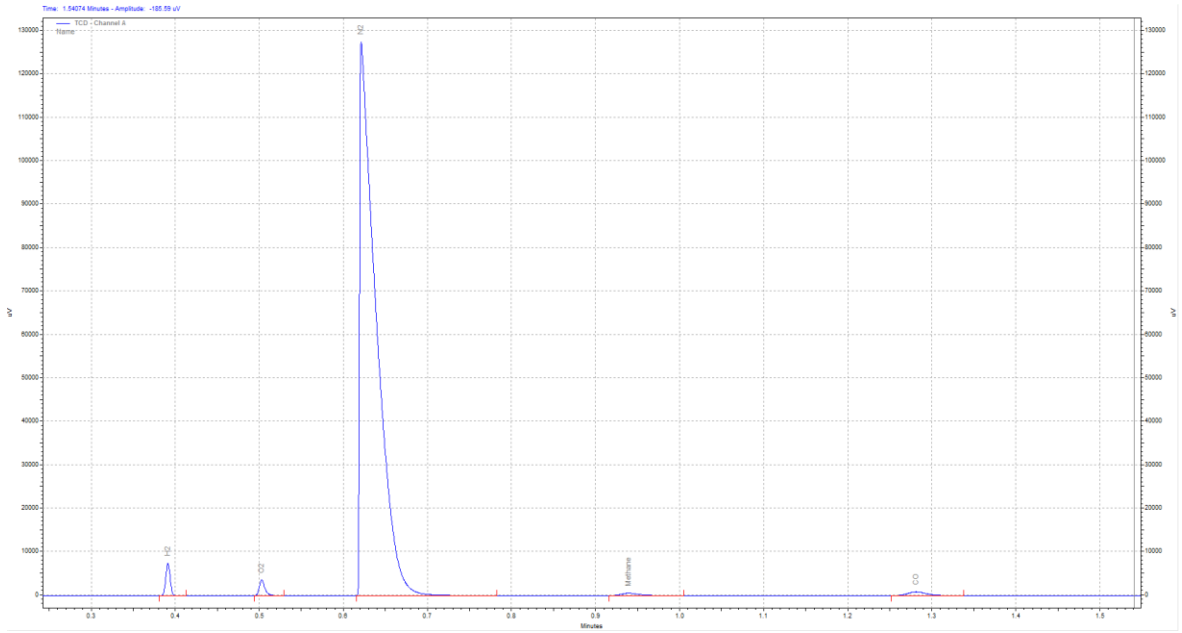

Figure 2. 28 - Column A output chromatogram

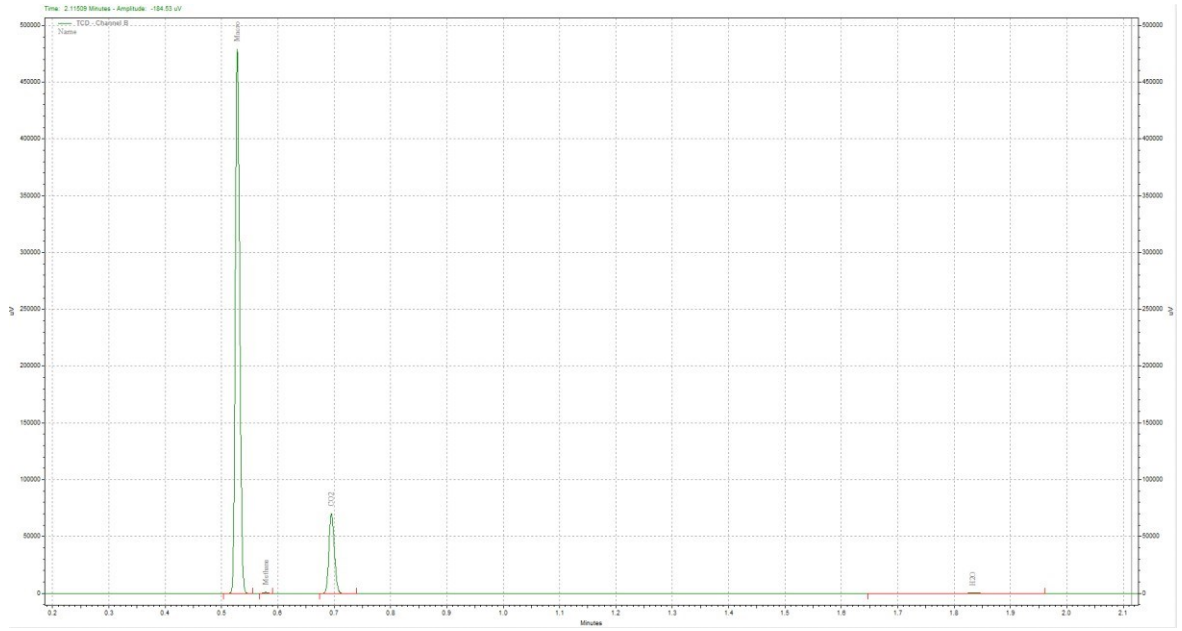

Figure 2. 29 - Column B output chromatogram

The chromatogram is characterised by some areas: in order to evaluate the gases composition, a correlation between chromatogram areas and the flux is necessary. For this purpose, a calibration of a set of so-called response factors has been made, according to the definition reported in Equation (2.10):

$$\alpha_i = \frac{\dot{Q}_i / \dot{Q}_{N_2}}{A_i / A_{N_2}} \tag{2.10}$$

With:

- α_i = i-species response factor [-];
- $\dot{Q}_i$ = i-species volumetric flow rate [NmL/min];
- $\dot{Q}_{N_2}$ = nitrogen volumetric flow rate [NmL/min];
- A_i = area subtended by i-species peak [μV·s];
- A_{N_2}= area subtended by the nitrogen peak [μV·s];

To compute each α_i, a mixture of nitrogen- which is used as reference gas- and i-species is prepared. The calibration concentrations and the volumetric flow rates are chosen to be in the range of values adopted during the experiments. The flow rates of each single component are measured thanks to a bubble flow meter. Of course, the total flow rate is kept constant, so varying the i-species concentration, the nitrogen flow rate is changed to balance. Once the mixture is analysed and a chromatogram is obtained, a calibration line for response factor of the investigated species is derived.

As already mentioned, the PLOTQ column does not evaluate a nitrogen peak, N_2, O_2 and CO are all represented in one. The signal from channel B chromatogram is worked out based on the data from Molsieve column: since O_2 and CO areas are known from channel A, it is possible to establish a correlation to find a "N_2 apparent peak" starting from the Macro peak. CO_2 and CH_4 response factors are based on the area of this apparent peak, defined in Equation (2.11):

$$A^*_{N_2} = A_{Macro} \cdot \frac{A_{N_2}}{A_{N_2} + A_{O_2} + A_{CO}} \tag{2.11}$$

With:

- $A^*_{N_2}$ = area of the "N_2 apparent peak" [μV·s];
- A_{Macro} = area subtended by the Macro peak [μV·s];

A second equation, useful to calculate the response factors of channel B, is represented in Equation (2.12):

$$\alpha_i = \frac{\dot{Q}_i / \dot{Q}_{N_2}}{A_i / A^*_{N_2}} \tag{2.12}$$

As already explained, water does not need an actual response factor, as the H_2O input flow rate is calculated from the pump setpoint, while the output flow rate is obtained from a material hydrogen balance.

Species retention time and response factors are summarized in Table 2.4.

Table 2. 4 – Agilent 3000A micro-GC species retention time and response factor calibration results

Species	Column	Carrier gas	Retention times [min]	α_i [-]
H_2	Molsieve	Ar	0.39	0.081
O_2			0.51	0.813
N_2			0.632	1.000
CH_4			0.959	0.404
CO			1.297	1.014
Macro (O_2+N_2+CO)	PLOTQ	He	0.536	1.000
CH_4			0.575	0.404
CO_2			0.682	0.788
H_2O			1.8	-

Ones the α_i values and the total nitrogen flow rate are known, the areas subtended by the peaks are converted into i-species flows. For channel A species:

$$\dot{Q}_i = \alpha_i \cdot \dot{Q}_{N_2} \cdot \frac{A_i}{A_{N_2}}$$

(2. 13)

For channel B species:

$$\dot{Q}_i = \alpha_i \cdot \dot{Q}_{N_2} \cdot \frac{A_i}{A^*_{N_2}}$$

(2. 14)

Since it is used as a reference gas, the response factor of N_2 is set equal to one: the corresponding flux used in Equations (2.13) and (2.14), can be calculated from the micro-GC analyses with Equation (2.15):

$$\dot{Q}_{N_2} = \frac{\dot{Q}_{tot}}{\sum_{i=1}^{m} \alpha_i \cdot \frac{A_i}{A_{N_2}}} = \frac{\dot{Q}_{tot}}{\frac{\sum_{i=1}^{m} \dot{Q}_i}{\dot{Q}_{N_2}}}$$

(2. 15)

With:

- m = number of species [-];
- $\dot{Q}_{tot}$ = total volumetric flow rate, evaluated with the bubble flowmeter [NmL/min];

Then, the molar flow rates are also computed by using the general gas equation:

$$\dot{N}_i = \frac{\dot{Q}_i}{RT/p} = \frac{\dot{Q}_i}{22.414 \cdot 10^{-3}}$$

(2. 16)

With:

- $\dot{N}_i$ = i-species molar flow rate [mol/min] ;
- R = 8.314 J/(mol·K) ;
- T = 273.15 K ;
- p = 101325 Pa ;

Finally, outlet molar fractions, reactants conversions and selectivities are computed, respectively with Equations (2.17),(2.18) and (2.19):

$$y_i = \frac{\dot{N}_i}{\sum_{i=1}^{m} \dot{N}_i} \tag{2. 17}$$

$$\chi_i = \frac{\Delta\dot{N}_i}{\dot{N}_i^{in}} = 1 - \frac{\dot{N}_i^{out}}{\dot{N}_i^{in}} \tag{2. 18}$$

$$S_i = \frac{\Delta\dot{N}_i^{j}}{\sum_{i=1}^{m} \Delta\dot{N}_i^{j}} = \frac{\Delta\dot{N}_i \cdot n_i^{j}}{\sum_{i=1}^{m} \Delta\dot{N}_i \cdot n_i^{j}} \tag{2. 19}$$

With:

- χ_i = i-species conversion [-] ;
- S_i = i-species selectivity [-] ;
- $\Delta\dot{N}_i = \dot{N}_i^{out} - \dot{N}_i^{in}$ [mol/min] ;
- n_i^j = number of j-element atoms in i-species molecule [-] ;
- $\Delta\dot{N}_i^j$ = molar flux of j-element relative to i-species with $\Delta\dot{N}_i \geq 0$;

Of course, reactants conversion and selectivities are defined only for $\Delta\dot{N}_i > 0$. Therefore, by convention, REP is set equal to zero if $\Delta\dot{N}_i < 0$.

Carbon, hydrogen and oxygen balances are computed to make sure that the chromatographic analyses meet the expected quality standards. The generic definition of these balances is reported in Equation (2.20):

$$B_j = \frac{\sum_{i=1}^{m} y_i^{out} \cdot n_i^{j}}{\sum_{i=1}^{m} y_i^{out} \cdot n_i^{j}} \cdot \frac{y_{N_2}^{in}}{y_{N_2}^{out}} \tag{2. 20}$$

Which leads to:

$$B_C = \frac{\sum_{i=1}^{m} y_i^{out} \cdot n_i^C}{\sum_{i=1}^{m} y_i^{out} \cdot n_i^C} \cdot \frac{y_{N_2}^{in}}{y_{N_2}^{out}} \tag{2. 21}$$

$$B_H = \frac{\sum_{i=1}^{m} y_i^{out} \cdot n_i^H}{\sum_{i=1}^{m} y_i^{out} \cdot n_i^H} \cdot \frac{y_{N_2}^{in}}{y_{N_2}^{out}} \tag{2. 22}$$

$$B_O = \frac{\sum_{i=1}^{m} y_i^{out} \cdot n_i^O}{\sum_{i=1}^{m} y_i^{out} \cdot n_i^O} \cdot \frac{y_{N_2}^{in}}{y_{N_2}^{out}} \tag{2. 23}$$

These quantities should, in theory, always be equal to one, but the formation of parasite species can lead to small variations. Consequently, if the balance exceeds unity, the concentrations of the reaction products are likely to have been overestimated; on the other hand, if they are less than one, an underestimation could affect the results. During experiments, a maximum deviation of 5% from unity is accepted. It is worth noting that, according to the equation (2.22), B_H is strongly dependent on the ratio $\frac{y_{N_2}^{in}}{y_{N_2}^{out}}$.

Mass spectrometer

The mass spectrometer is able to measure the downstream flue gases composition continuously, performing an analysis cycle every 8 seconds.

The instrument operating on the rig is a Balzer QMS200, presented in Figure 2.30; it is located outside the hood and connected to the outlet of the reactor, where also the micro-GC line samples the product gases from.

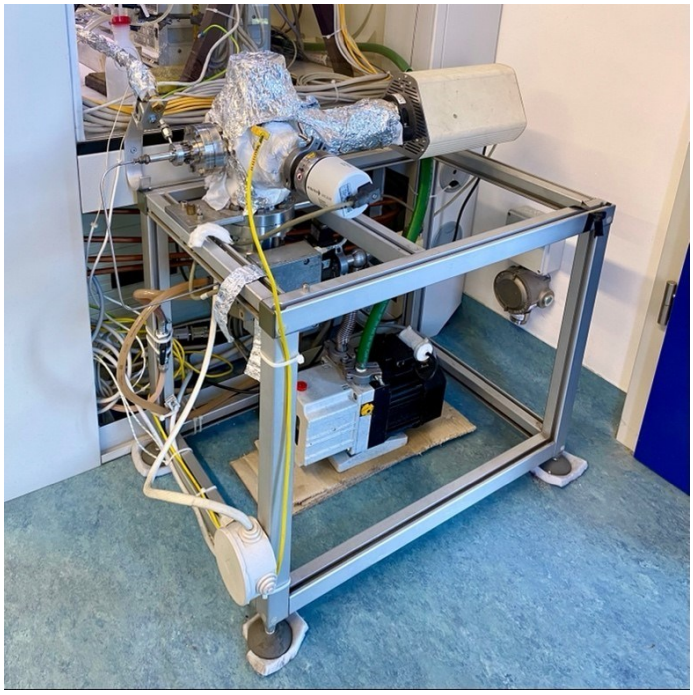

Figure 2. 30 - Balzer QMS200 mass spectrometer

Mass spectrometers work acquiring a small and constant flux (10 NmL/min) from the line. Then, as later described, only a portion (10-20%) of this flow rate reaches the actual analysis section of the instrument.

Mass spectrometers main components are:

- A sampling system ;
- A vacuum system ;
- An ion source (or ionization chamber) ;
- A mass analyser ;
- A detector ;

The sampling system makes it possible to collect the gas whose composition needs to be investigated.

The vacuum system consists of a chamber with two orifices, one located at the front, the other at the back of the volume. The internal diameter are 30 μm for the former, while 50 μm for the latter. Three lines split from here: the first one, introduces the gas sample through the front orifice; the second connects the chamber to the differential pump; the third sends a flow rate to the analysing system through the 50 μm orifice.

The vacuum chamber is kept at around 0.25 mbar, while the analysis section works under extremely low-pressure conditions, of the order of 10^{-6} mbar, thanks to a turbomolecular pump. A rotary vane liquid-ring pump, called "forepump", is placed prior to the vent atmospheric discharge, to not exceed the limit on the possible pressure jump across the turbopump. Pressure levels are constantly monitored; if they differ from the reported values, it means that something wrong is happening, such as clogging or leakages, which could affect the results.

When not performing measurements, even overnight, it is pivotal to keep a minimum flow rate in the lines (nitrogen in this case) in order to prevent the differential pump mechanism from damages. Furthermore, the oxidizing agents' content in the sampled stream should be controlled and adjusted by dilution with inert to protect the ionizing elements.

Gases enter in the ionization chamber by pressure difference. Here, two yttria-coated iridium filaments, heated up to between 1600 °C and 2000 °C, liberate electrons by thermionic emission. Each electron has an energy of 70 eV: about 10 eV are enough to ionize natural species, while the remaining lead to ions fragmentation. Such generated hot ion beam then encounters an electric field generated by a series of alternately charged perforated plates. Anions collide on the first positively charged electrode; subsequently, cations are attracted towards a negative electrode. Here, a neutrally charged plate is located in order to maintain the right trajectory. A second positive electrode provides for a further accelerationof the remaining ions.

The quadrupole mass analyser (QMS) consists of four parallel steel cylindrical rods; a directvoltage is applied between each of the pairs of opposite rods, which are also connected electrically to a radio frequency generator. Ions, reaching the analyser thanks to a weak driving potential around 5-10 V, enter the quadrupole and travel following oscillating pathways along the axis of the QMS under the effect of the two applied electrical fields. They are then separated according to their mass-to-charge ratio (m/z): for a certain value of voltages ratios, only ions of a given m/z will reach the detector. Other ones will collide with the rods due to their unstable trajectories. By adjusting the applied voltages, while their ratio is kept constant, it is possible to examine a different m/z range.

Charged molecules are detected relying on a direct current signal, whose magnitude is influenced by the charge and by the abundance of the compound. As the concentration grows, the ions flux will be more significant, leading to a higher electric current. Anyway, since the number of ions reaching the detector per unit time is modest, amplification is needed: electron multipliers and electrometers are employed for this purpose.

Signals are acquired and displayed by dint of "Measure" (Figure 2.31) and "Dispsav" (Figure 2.32) software programs.

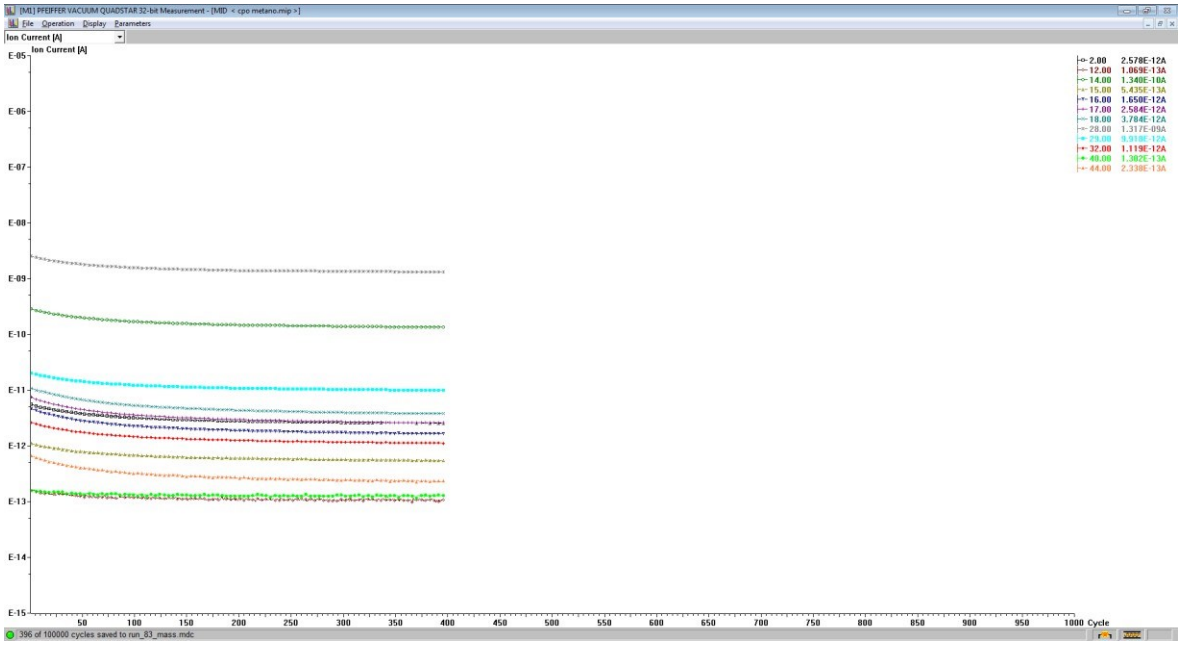

Figure 2. 31 - "Measure" software signal acquisition

At this point, we obtain different signals each referring to a value of m/z. To obtain effective and physical results, it is necessary to determine the most representative signal for each species in the reactor outlet mixture. Quite likely, the signal characterized by a value of m/z corresponding to the molecular weight of the compound under investigation is the best one, but this is not always true. Nevertheless, a rigorous calibration is required to investigate which output signal is the most sensitive to concentration variations of the given species. For example, the output current signal with a ratio m/z =15 is the most representative for methane concentrations.

Here, in Table 2.5, output signal m/z values for each species are reported:

Table 2. 5 – Correspondence between mass spectrometer m/z values and chemical species

Species	**Mass-to-charge ratio (m/z)**
H_2	2
CH_4	15
H_2O	18
O_2	32
Ar	40
CO_2	44

Now, the output current signals expressed in [A] need to be converted into concentration values. To do so, a β response factor is required for each i-species. The derivation of this parameter is the basis of the following procedure for operating the mass spectrometer during the tests:

1. A nitrogen mass flow rate, equal to the total one sent during experiments, is sent through the bypass line. This will generate an output signal, called *background* signal, that takes some time to stabilize;
2. Once the background is stable, the second step is to switch to the reactants mixture, bypassing the reactor. A series of micro-GC analyses are performed to pinpoint the *feed* stream molar fractions;
3. Once the oven is preheated, the feed mixture is sent to the reactor.

The sequence of output signals relative to the procedure is visible in Figure 2.32, on the software "Dispsav". It is easy to recognize three different signals relating to background, feed and product mixture respectively.

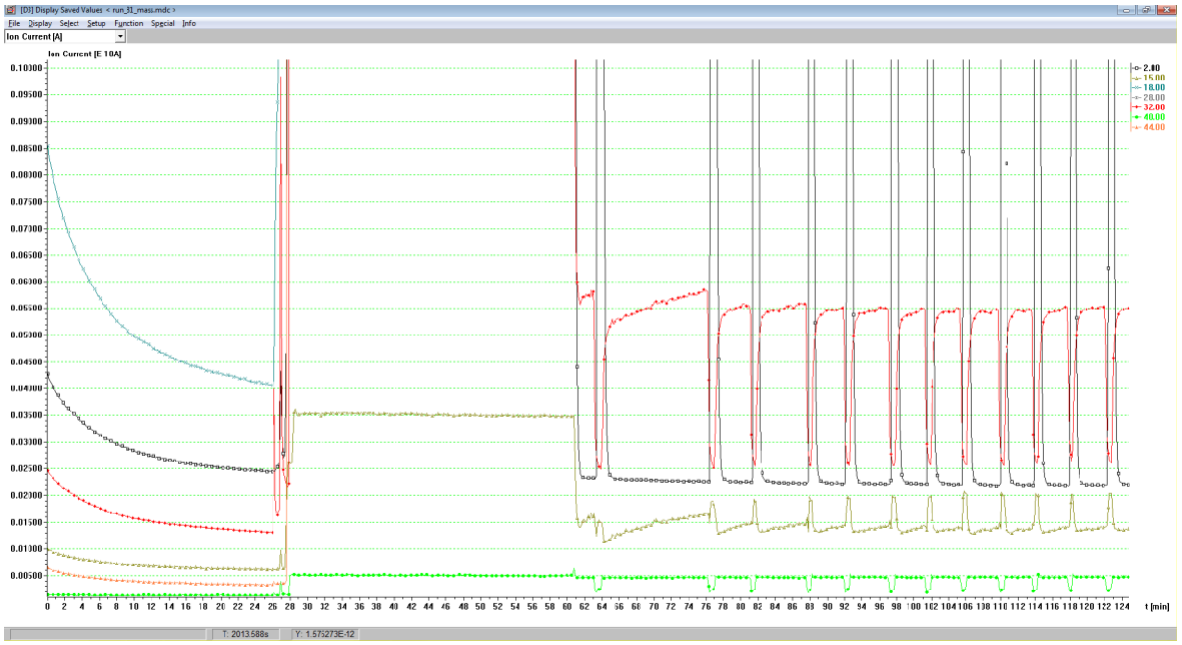

Figure 2. 32 - "Dispsav" data processing: background, feed and products

The *background* signal is used as a reference ionic current, while the feed signal contains information about reactant concentration, that are required to establish the complete relationship.

According to Equation (2.24), β correlates the output signal and the concentration of the i-species:

$$\Delta\mu_i = \beta_i \cdot \Delta y_i \tag{2. 24}$$

With:

- β_i = i-species response factor [A/ppm];
- $\Delta\mu_i = \mu_i^{feed} - \mu_i^{background}$ = difference between feed and background stream i-species signal [A];
- $\Delta y_i = y_i^{feed} - y_i^{background}$ = difference between feed and background i-species concentration; numerically it is equal to the molar fraction in the reactant mixture for each species, except for nitrogen [ppm];

Since μ_i value is extracted from Dispsav software, y_i^{feed} is obtained from micro-GC analyses and $y_i^{background}$ is assumed equal to zero (background is 100% nitrogen), β_i is easily computed.

The next step is to evaluate the i-species concentration in time during the experiment. To do this, the β_i definition in simply rearranged in Equations (2.25) and (2.26):

$$\Delta y_i(t) = \frac{\Delta\mu_i(t)}{\beta_i} \tag{2. 25}$$

$$y_i^{products} = \frac{\mu_i^{products}(t) - \mu_i^{background}}{\beta_i} + y_i^{background} \tag{2. 26}$$

With:

- $\Delta\mu_i(t) = \mu_i^{products}(t) - \mu_i^{background}$ = difference between time *t* and background stream i-species signal [A] ;
- $\Delta y_i(t) = y_i^{products}(t) - y_i^{background}$ = difference between time *t* and background stream i-species concentration [ppm] ;

Then, reactants conversions can be computed:

$$\chi_i(t) = 1 - \frac{y_i^{products}(t)}{y_i^{feed}} \tag{2. 27}$$

It is worth to notice that conversion could also be expressed as not dependent from the response factors, but only as a function of the signal differences as represented in Equation (2.28):

$$\chi_i(t) = 1 - \frac{\frac{\mu_i^{products}(t) - \mu_i^{background}}{\beta_i}}{\frac{\mu_i^{feed}(t) - \mu_i^{background}}{\beta_i}} = 1 - \frac{\mu_i^{products}(t) - \mu_i^{background}}{\mu_i^{feed}(t) - \mu_i^{background}} \tag{2. 28}$$

2.2. Experimental approach and methods

Concerning the experimental activity, beside oven temperature and feed mixture composition, one of the most important parameters to be chosen is the Gas Hourly Space Velocity (GHSV), defined as:

$$GHSV = \frac{\dot{Q}_{tot} \cdot 60}{V_{mon}} \tag{2. 29}$$

With:

- $GHSV$ = Gas Hourly Space Velocity [1/h] ;
- $\dot{Q}_{tot}$ = total gas flow rate at NTP [Ncm^3/min] ;
- V_{mon} = monolithic sample volume [cm^3];

The total gas volumetric flow rate adopted for all the experiments is $\dot{Q}_{tot}$= 2100 [Ncm^3/min], leading to a GHSV value of 50481 h^{-1}.

Table 2. 6 – Values for GHSV calculation

V_{nom} [cm^3]	$\dot{Q}_{tot}$ [Ncm^3/min]	GHSV [1/h]
2.496	2100	50481

The feed mixture composition was modified during the experimental campaign to investigate various effects, always referring to the definition of equivalence ratio:

$$\lambda = \frac{\dot{Q}_{air,engine}}{\dot{Q}^{st}_{air,engine}} \tag{2. 30}$$

With:

- λ = equivalence ratio [-] ;
- $\dot{Q}_{air,engine}$ = actual internal combustion engine inlet air flow rate [Ncm^3/min] ;
- $\dot{Q}^{st}_{air,engine}$ = stoichiometric internal combustion engine inlet air flow rate [Ncm^3/min] ;

The stoichiometric amount of air is the quantity needed to obtain the complete fuel oxidation; the flow rates are not referred to the catalyst inlet, but to the engine.

However, a λ formulation can be derived from stoichiometric balances for a natural gas engine; the result is the Equation (2.31) [53]:

$$\lambda = \frac{y_{O_2,air}}{2} \cdot \frac{4 \cdot y_{CH_4} + 3 \cdot y_{CO} + 3 \cdot y_{H_2} - 2 \cdot y_{O_2} - 4}{\left(y_{CO} + y_{H_2} - 2\right) \cdot y_{O_2,air} + \left(2 \cdot y_{O_2} - y_{CO} - y_{H_2} - 4 \cdot y_{CH_4}\right)} \tag{2. 31}$$

With:

- y_i = i-species molar fraction at the ICE outlet (i.e., catalytic converter inlet) [-]

If $\lambda < 1$, the feed is *rich*, while when $\lambda > 1$ the feed is *lean*.

Two sets of feed mixture composition (A and B), representative of the exhausts from a natural gas vehicle, were investigated. The compositions are reported in Table 2.7:

Table 2. 7 – Feed mixture compositions

Species	**CH_4**	**H_2**	**CO**	**H_2O**	**O_2**	**CO2**	**N_2**
$y_{i,A}$ [vol%]	0.15	0.1	0.6	0 - 10	0.46 – 1.02	10.7	Balance
$y_{i,B}$ [vol%]	0.325	0	0	0 - 10	0.46 - 1.02	10.7	Balance

The different λ values are obtained by changing the oxygen content in the feed mixture and adjusting the N_2 concentration to balance the total flow rate. Also, the effect of moisture has been investigated, keeping constant the total flow rate in the same way.

It is useful to introduce another parameter: the equivalence ratio at the converter inlet, S, computed as:

$$S = \frac{\dot{Q}_{air,cat}}{\dot{Q}^{st}_{air,cat}} = \frac{y_{O_2}}{y^{st}_{O_2}} \tag{2. 32}$$

With:

- S = catalyst equivalence ratio [-] ;
- $\dot{Q}_{air,cat}$ = actual catalyst inlet air flow rate [Ncm^3/min] ;
- $\dot{Q}^{st}_{air,cat}$ = stoichiometric catalyst inlet air flow rate [Ncm^3/min] ;
- y_{O_2}= catalyst inlet oxygen molar fraction [-] ;
- $y^{st}_{O_2}$ = stoichiometric catalyst inlet oxygen molar fraction [-] ;

S amplifies the engine equivalence ratio: due to the combustion in the ICE, small λ variations become large S differences.

In the present work, fuel species fed to the catalyst are a mixture of methane, carbon monoxide and hydrogen or pure methane. $\dot{Q}^{st}_{air}$ can be computed from the reaction balances:

$$CH_4 + 2O_2 \rightarrow CO_2 + 2H_2O \tag{2. 33}$$

$$CO + \frac{1}{2}O_2 \rightarrow CO_2 \tag{2. 34}$$

$$H_2 + \frac{1}{2}O_2 \rightarrow H_2O \tag{2. 35}$$

According to the stoichiometric coefficients, in both composition A and B, $y^{st}_{O_2}$= 0.65.

In figure 2.33, the relationship between S and λ is reported:

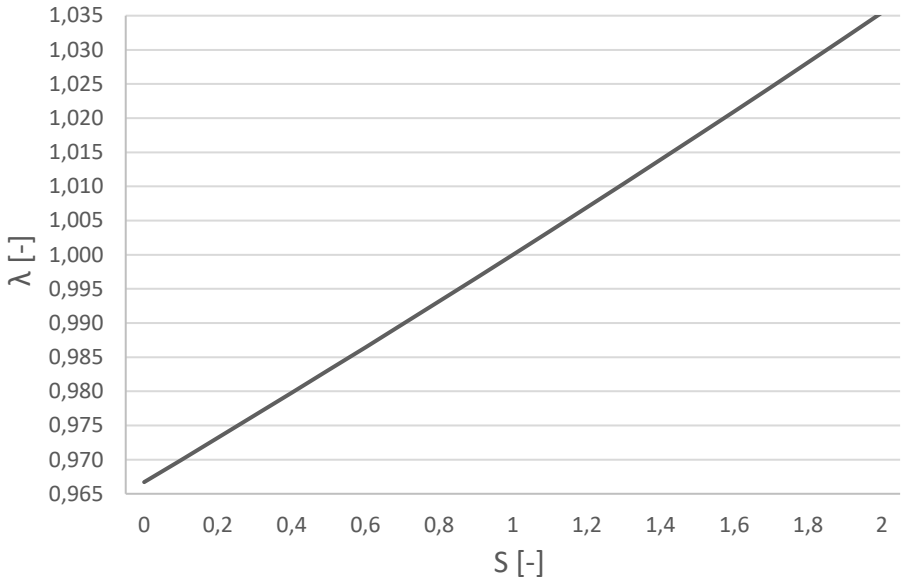

Figure 2. 33 - λ vs S

2.2.1 Degreening treatment

Prior to each experimental campaign, whenever the catalytic sample is changed, a degreening treatment is needed. Firstly, a stoichiometric mixture (λ = 1) is prepared, always keeping constant the fuel concentrations (CH_4, CO, H_2), Then, after preheating the oven to 600 °C, the feed is sent to the reactor for 5 hours, Downstream concentrations are constantly monitored with both micro-GC and mass spectrometer.

2.2.2 Conditioning treatment

The conditioning test consists in feeding the catalyst with a slightly lean mixture (λ = 1.02) after pre-heating the oven at 450 °C. This is done to stabilize as much as possible the honeycomb catalytic performances. Once the reactant composition is found and the oven reaches the setpoint temperature, reactants are fed to the reactor. During the first 30 minutes, downstream conversions are monitored. Then, a series of 30-seconds rich pulses (λ = 0.98) is performed to push the conversion to its maximum. After a pulse, three micro-GC analysis are launched so that 12 minutes are waited between each pulse. The final purpose is to obtain a more stable behaviour of the catalyst, reaching the same conversions after each pulse, by reducing the conversion delta between pulses.

2.2.3 Deactivation test

During this test, the catalytic converter works under oxidizing conditions for a prolonged time. The aim is to quantify the decline in methane conversion when a mixture is fed without performing rich pulses.

Firstly, the desired reactants composition is found and the oven is pre-heated. Then, the mixture is sent to the reactor and micro-GC analyses are sent to monitor the products composition. Mass spectrometer is also used to monitor methane behaviour. During this phase, as already mentioned, pulses are not performed.

This test, necessary for every mixture composition, gives guidelines to evaluate the behaviour of catalytic activity in the explored conditions.

2.2.4 Concentration and temperature profiles acquisition

Concentration profiles acquisition allows to obtain information about the gas composition through the reactor. It is important because different reactions occur on the system and it is significant to see how they proceed both in time and space, to better understand the behaviour of the catalyst.

Concentration and temperature profiles are obtained at different λ, oven temperatures and compositions to cover as much as possible the working range conditions of a natural gas vehicle.

For each experiment, λ, water content, and oven temperature are chosen. The feed composition can be stationary for the entire test, or a series of periodic pulses can be introduced to contrast the catalyst deactivation. The downstream conversion of methane – a key parameter for catalyst activity- is kept constant through monitoring with the micro-GC and the mass spectrometer. For experiments with pulses, the optimal pulse frequency is defined based on the deactivation test: one pulse every 8 minutes is usually enough to prevent catalyst deactivation.

The starting point for the procedure is the feed check using the micro-GC; then the background is sent in bypass until MS signals become stable and the oven is preheated. When the reactants are sent to the reactor, three rich pulses are performed to make sure the initial activity level of the catalyst is comparable among different experiments. At this point, downstream conversion is assessed by running two micro-GC analyses, the second of which is always integrated to obtain concentration values.

By operating the three-way valve in Figure 2.24, the micro-GC aspiration is switched from downstream to the concentration capillary.

The starting point of the capillary tip is 2 mm beyond the catalyst outlet section, to ensure that the complete profile is sampled. Now, the capillary can be moved backward to the monolith inlet, thanks to the linear stage, to analyse the gases composition along the entire catalyst. Depending on the experiment, the sampling resolution can be 1 mm or 2 mm. The axial profile is sampled from the outlet of the catalyst to avoid possible capillary tip breaks, due to interactions with monolith walls; damages are more likely to occur when the tubing is inserted in the honeycomb channel.

The mass spectrometer gives a real-time check on downstream concentration; in addition, once a hour, it is also monitored with micro-GC. The profile acquisition is considered complete once the sampled composition coincides with the feed mixture.

Gas temperature profiles cannot be acquired at the same time as concentration profiles, as a different configuration of the mobile stage is required. However, the reaction conditions are highly reproducible and a good correspondence between the results is obtained. Obviously, a check on the composition of the reactants and downstream conversions is carried out prior to temperature acquisition to ensure that the same mixture feeds the reactor and conversions are representative of the concentration profile tests.

Temperature measurements are collected with the data recording function in "DAQExpress" software. The temperature reading is monitored until it reaches a stable value; then the thermocouple is moved to the next axial coordinate. Rich pulses are performed with the same frequency, in the experiments characterized by catalyst deactivation.

The temperature capillary length is purposely supersized; a void part between the thermocouple tip and the end of the tubing guarantees that the sealed extremity never enters the monolith, even when the data acquisition at the catalyst inlet is taking place. For this reason, the linear actuator can be operated back and forth without the risk of damages. Consequently, since there is no need to reposition the tubing, the temperature profiles are collected much more rapidly. Another plus is that relative misalignment between the profiles is avoided.

Both when performing concentration and temperature test, it is good practice to alternate rich and lean-mixture tests test to re-oxidize the catalytic sample.

3 Results

In this chapter, experimental results are discussed. In particular, the effects of temperature, water content and feed mixture on methane conversion are presented. Also, an analysis of some preliminary tests are given.

3.1. Preliminary concepts

First, a description of the degreening test and conditioning test are reported. Then, general information about the strategies adopted during experiments are explained.

3.1.1. Results of degreening test

As already anticipated, before each experimental campaign, the catalyst sample needs to be treated. The procedure followed is called "degreening test" and it is a common practice when commercial honeycombs are tested. During this test, the oven is preheated at 600 °C and a stoichiometric mixture ($\lambda = 1$) is sent to the reactor. The feed composition is reported in Table 3.1:

Table 3. 1 - Species concentrations of the mixture used during the degreening test

Species	**CH_4**	**H_2**	**CO**	**H_2O**	**O_2**	**CO_2**	**N_2**
y_i [vol %]	0.15	0.1	0.6	10	0.6508	10.7	Balance

The oven temperature set during the degreening is out of the range of interest for the experimental activities (400 °C < T_{oven} < 450 °C), it is chosen to establish reproducible performances. The total duration of the process is 5 hours: 97% of methane is converted at the beginning, then the downstream conversion decreases due to catalyst deactivation. The final conversion reached is around 82.5%.

The methane conversion trend during the test is displayed in Figure 3.1:

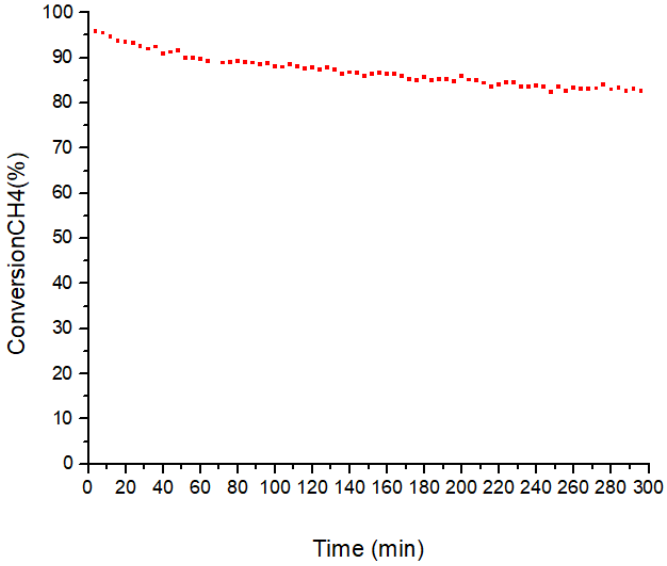

Figure 3. 1 – Methane conversion during the degreening test

3.1.2. Results of conditioning test

In order to stabilize the catalyst activity in the experimental operating conditions [54], [55], a conditioning treatment is required. It consists in running a test with a feed mixture which is the one used during experiments. A lean mixture (λ = 1.02) is used, at 10% water content (Table 3.2).

Table 3. 2 - Species concentrations of the mixture used during the conditioning test

Species	**CH_4**	**H_2**	**CO**	**H_2O**	**O_2**	**CO_2**	**N_2**
y_i [vol %]	0.15	0.1	0.6	10	1.032	10.7	Balance

To do this, the oven is preheated at 200°C, to avoid species condensation, while the gases are flowing through the bypass line. Then, the mixture is fed to the reactor; once it is flowing through it, the oven is heated up to 450 °C. Initially, the lean flow rate is fed to the reactor for 30 minutes.

Then, a series of rich pulses (30s at λ = 0.98) is performed, with the same composition of table 3.2 but at 0.265% O_2 , one every 12 minutes. The downstream methane conversion is monitored, analysing gas samples exiting the reaction section with the micro-GC. This process continues until stable methane conversions are reached.

The methane conversion profile is reported in Figure 3.2. It is clearly visible that at the beginning the catalyst activity is very low (χ_{CH_4} = 31 % after the first 30 minutes without

pulses). When pulses are performed, methane conversion rapidly increases and, at the end of the process, it approaches 94%.

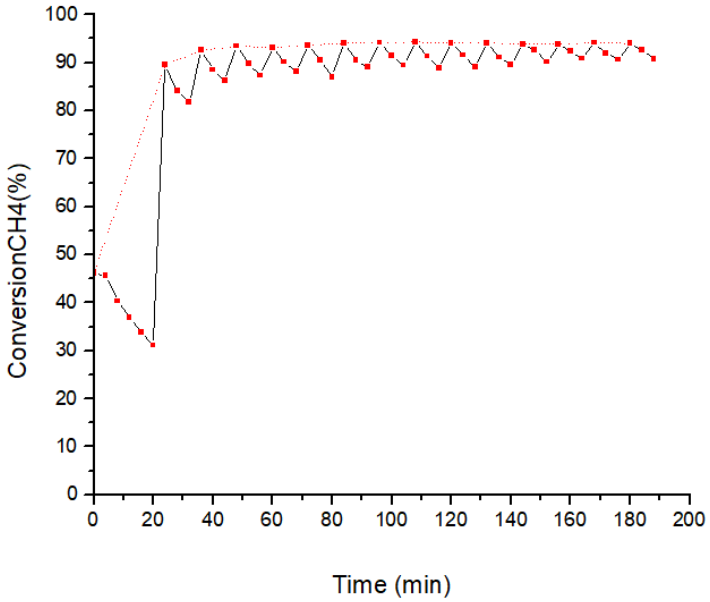

Figure 3. 2 – Methane conversion during the conditioning test

It is worth to notice that through the strategy of rich pulses, not only the total catalyst activity increases, but also the conversion losses with time are reduced. After the first pulse, CH_4 conversion decreases of ~ 8%, while after the last one the reduction becomes ~ 3%. At the end of this procedure, high catalyst activity and good performances in terms of time-stability are reached.

The reasons of this increase in catalyst activity, up to a stable maximum level, is related to the weakening of the interactions between the Pd catalyst and the support, which would otherwise inhibit PdO redox ability [56].

3.1.3. Stability and periodic pulse operation

Depending on feed composition, temperature, water feed content, the Ecocat sample could be affected by deactivation. For example, under lean conditions (λ = 1.02), with a 10% water content, at 450 °C, a sensible reduction in methane conversion is already visible after 30/45 minutes of reaction, in agreement with previous results from the literature [37]. Different explanation for activity losses have been suggested, like the formation of stable palladium hydroxides or a decrease of active surface because of PdO layers smoothening. For sure, strong impact is given by water poisoning.

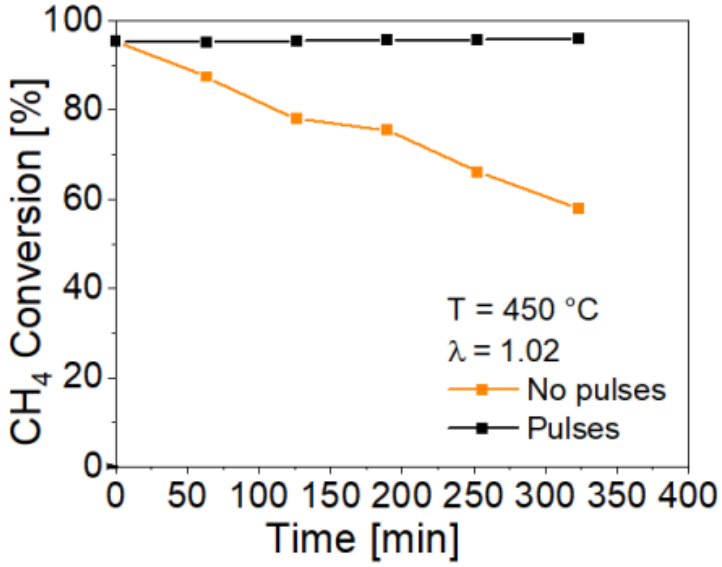

Figure 3. 3 – Catalyst deactivation at 450 °C and λ = 1.02

A concentration profile acquisition test may last between 4 and 7 hours, depending on the axial capillary resolution. It is clear that a strategy to stabilize the catalyst activity is needed, to obtain comparable profiles. To restore the catalytic activity, periodic rich mixture switches are considered optimal [57]. On average it was observed that a 30 seconds pulse every 8 minutes is enough to keep the downstream methane conversion constant.

In Figure 3.4, the outlet methane, oxygen and hydrogen concentrations during a rich pulse are showed.

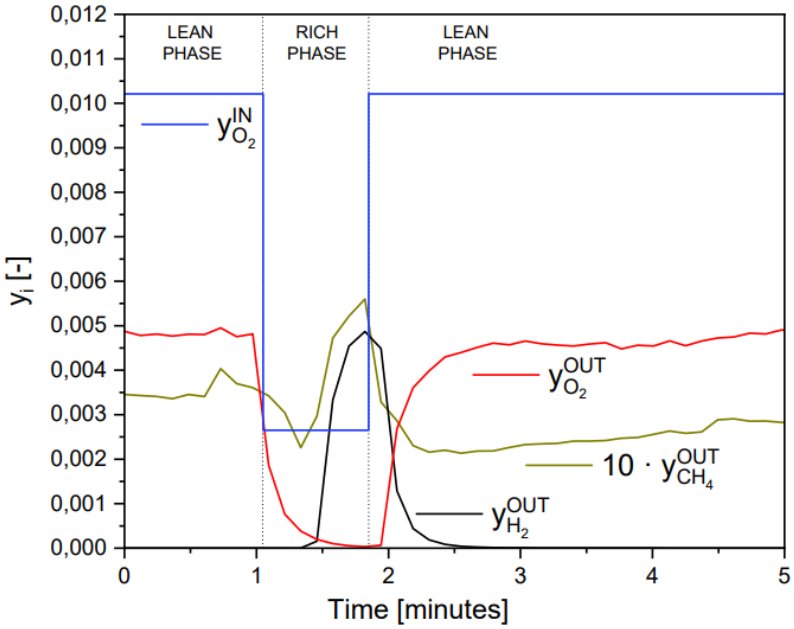

Figure 3. 4 – Concentration of involved species during a rich pulse

Passing from lean to rich conditions, hydrogen and methane concentration increases preceded by an evident delay. This is related to the redox reactions occurring at the catalyst surface. Once rich conditions are established, PdO is reduced to metallic Pd following three reactions:

$$CH_4 + 4PdO \rightarrow 4Pd + CO_2 + 2H_2O \tag{3. 1}$$

$$CO + PdO \rightarrow Pd + CO_2 \tag{3. 2}$$

$$H_2 + PdO \rightarrow Pd + H_2O \tag{3. 3}$$

After a first increase in methane fraction, y_{CH_4} is reduced once the oxygen approaches zero. This is because of steam reforming (SR) and water gas shift (WGS) reactions on metallic Pd [58]. SR and WGS reactions are, respectively:

$$CH_4 + H_2O \rightarrow CO + 3H_2 \tag{3. 4}$$

$$CO + H_2O \rightarrow CO_2 + H_2$$

(3. 5)

At the end of the pulse, once the initial oxygen content is re-established, palladium undergoes oxidation:

$$Pd + \frac{1}{2}O_2 \rightarrow PdO$$

(3. 6)

The result is that methane concentration decreases, reaching a lower value than before the rich pulse. Thanks to this reduction/re-oxidation process the catalyst activity is restored.

Oppositely, as reported in Figure 3.5 for experiments in rich conditions, there is no evidence for need of pulses since the downstream conversion of methane suggests a stable behaviour of the catalyst.

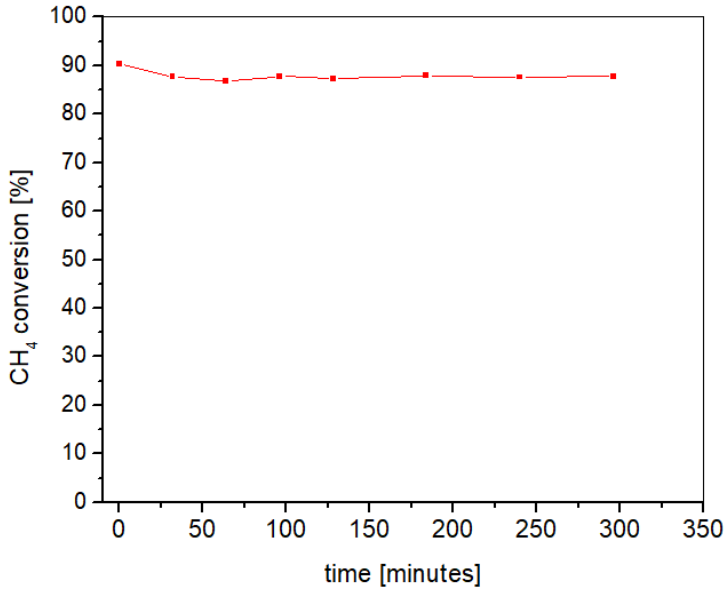

Figure 3. 5 – Methane conversion at 450 °C, 10% H_2O and λ = 0.99

Further analyses showed that the higher the water content, the largest is the set of feed compositions which require rich pulses to keep the downstream methane conversion constant.

In this work, different set of conditions are tested changing fuel composition, water content, oxygen content and temperature. As already mentioned in Table 2.7, the first campaign is performed running a fuel feed mixture composed by CH_4, CO and H_2 and changing λ, y_{H_2O}, and temperature. During the second experimental campaign, CO and H_2 are removed and replaced with CH_4, in order to respect the stoichiometry for the O_2 consumption.

3.2. CH_4 – CO – H_2 feed

First, a feed composition made of CH_4, CO and H_2 has been investigated, according to the classical composition of NGVs exhausts. All the experiments are performed keeping constant their concentrations in the feed:

Table 3. 3 - Species concentrations of the mixture used during the first campaign

Species	CH_4	H_2	CO	H_2O	O_2	CO_2	N_2
y_i [vol %]	0.15	0.1	0.6	0 - 10	0.46 – 1.02	10.7	Balance

The concentrations of oxygen and water were changed to evaluate the impact of different λ and moisture content, as well as temperature.

In Table 3.4 a list of the experiments carried out with the CH4-CO-H2 fuel is reported:

Table 3. 4 – List of experiments performed by feeding CH_4-CO-H_2 as fuel

λ	S	T [°C]	CH_4	H_2	CO	H_2O	O_2	CO_2	N_2	Pulses
1.02	1.57	450	0.15	0.1	0.6	10	1.03	10.7	Balance	Yes
0.9963	0.89	450	0.15	0.1	0.6	10	0.58	10.7	Balance	Yes
0.99	0.71	450	0.15	0.1	0.6	10	0.46	10.7	Balance	No
1.02	1.57	400	0.15	0.1	0.6	10	1.03	10.7	Balance	Yes
0.9963	0.89	400	0.15	0.1	0.6	10	0.58	10.7	Balance	Yes
0.99	0.71	400	0.15	0.1	0.6	10	0.46	10.7	Balance	No
1.02	1.57	450	0.15	0.1	0.6	2	1.03	10.7	Balance	Yes
0.9963	0.89	400	0.15	0.1	0.6	2	0.58	10.7	Balance	No
0.99	0.71	400	0.15	0.1	0.6	2	0.46	10.7	Balance	No
1.02	1.57	450	0.15	0.1	0.6	0	1.03	10.7	Balance	No
0.9963	0.89	400	0.15	0.1	0.6	0	0.58	10.7	Balance	No
0.99	0.71	400	0.15	0.1	0.6	0	0.46	10.7	Balance	No

3.2.1. Effect of λ

The effect of the oxygen content is the first studied. For this purpose, tests with three different values of λ have been performed:

- λ = 1.02;
- λ = 0.9963;
- λ = 0.99;

Temperature profiles at different λ, by fixing T_{oven} = 450 °C and 10% water content are reported in Figure 3.6:

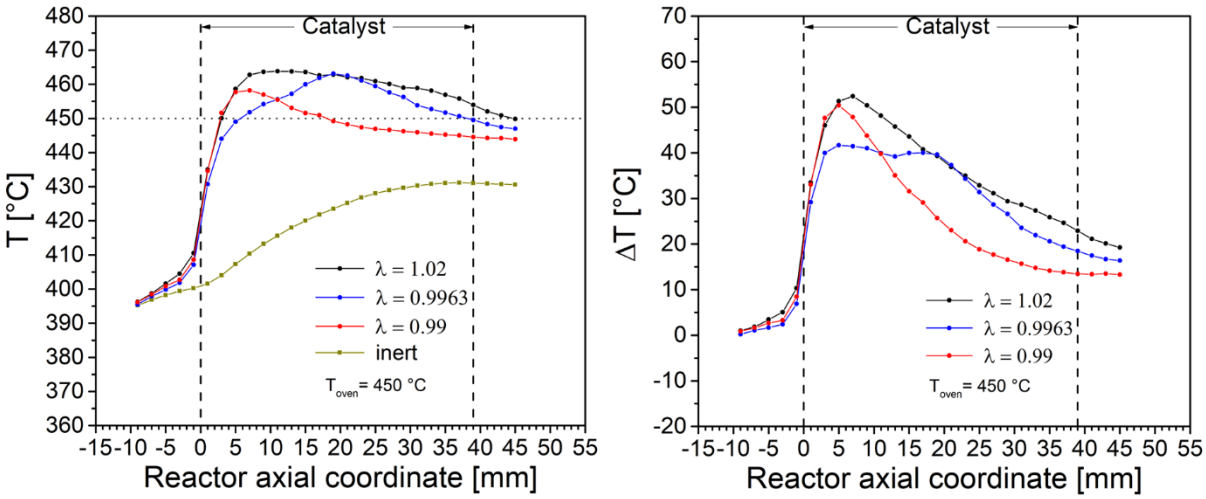

Figure 3. 6 – Temperature profiles at T_{oven} = 450 °C and 10% of H_2O

As already mentioned, the inert (N_2) temperature profile is not uniform along the reactor, the temperature significantly increasing from the inlet to the outlet of the reactor. Fortunately, such non uniformities are balanced by the heat of reactions. In the first part of the reactor, temperature increases rapidly in all profiles, due to the fast oxidation of CO and H_2.

At λ = 1.02, after the initial rapid increase, the temperature profile shows an almost linear trend. This is because methane is converted only by catalytic oxidation with O_2, so that the T profile is simply the result of the heat released by methane combustion.

At λ = 0.99, a peak of temperature is visible at x = 6 mm, that corresponds to the point before the SR start. Then steam reforming, which is an endothermic reaction, occurs and temperature starts decreasing faster than at lean-fuel conditions.

At λ = 0.9963, the profile is quite different due to the presence of a delayed peak. It can be attributed to a change in methane consumption rate at y_{O_2} = 0.0015, which will be discussed later. After the peak, once oxygen is completely consumed at x = 20, SR is responsible for methane conversion and temperature decreases.

In Figure 3.7, concentration profiles at different λ are reported, by fixing T_{oven} = 450 °C and $y_{H_2O}^{in}$ = 0.1.

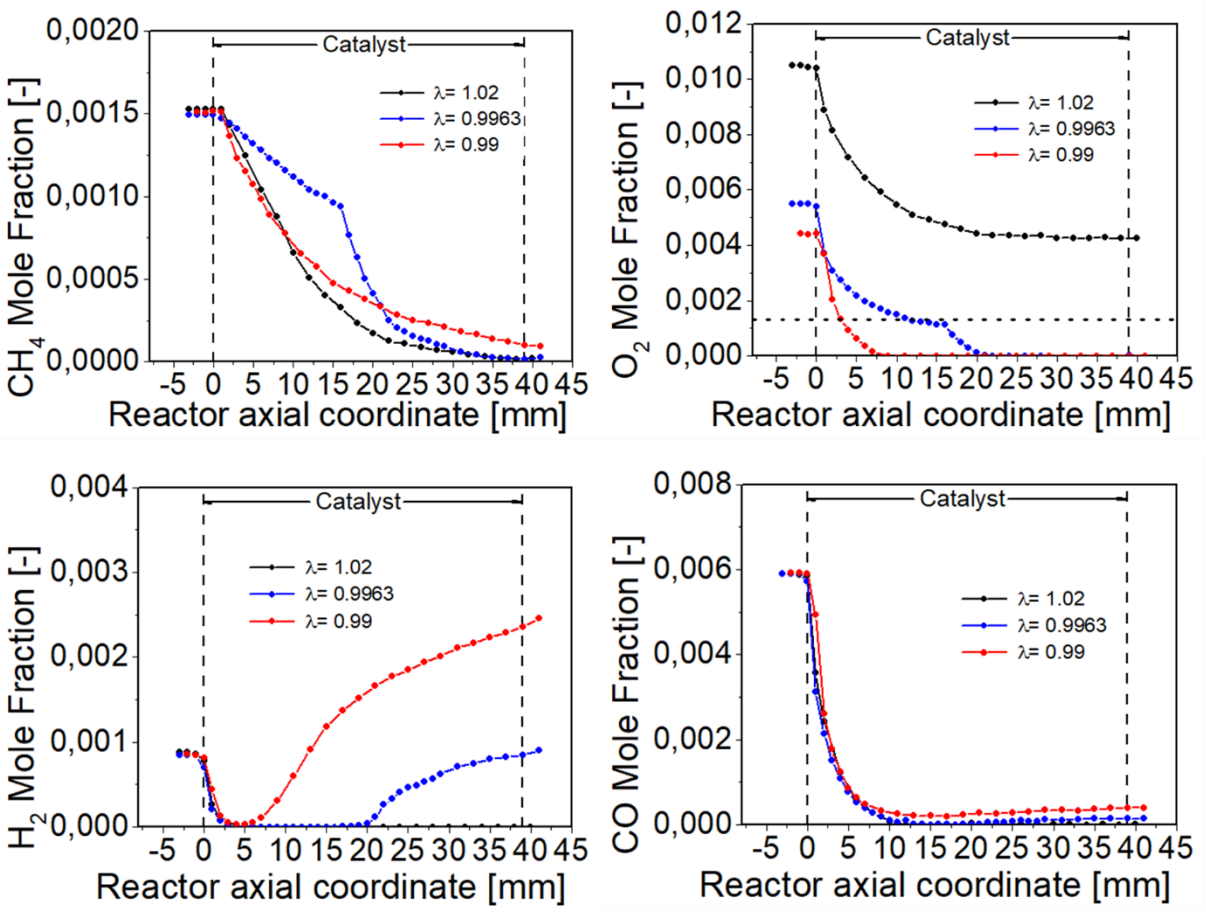

Figure 3. 7 – Concentration profiles at T_{oven} = 450 °C, 10% H_2O, λ = 1.02, 0.9963, 0.99

Both at lean and slightly-rich conditions, pulses are needed to keep constant the methane downstream conversion. This is important in order to compare different feeds without considering the effect of deactivation during the experiment.

As far as it concerns H_2 and CO oxidation, it is possible to affirm that they are not influenced by the oxygen content. In fact, apart from the differences in H_2 and CO productions, the most striking variations are related to the plots of methane and oxygen consumption. In conditions of excess of oxygen, for λ = 1.02, there is no evidence for reaction pathways different from the oxidation ones:

$$H_2 + \frac{1}{2}O_2 \rightarrow H_2O \tag{3. 7}$$

$$CO + \frac{1}{2}O_2 \rightarrow CO_2 \tag{3. 8}$$

$$CH_2 + 2O_2 \rightarrow CO_2 + H_2O$$

(3. 9)

At fully-rich mixture (λ = 0.99), hydrogen production is already visible after the first 4 mm of the monolith, even though oxygen is completely consumed at x = 8 mm. This can be attributed to a back diffusion phenomenon. Anyway, methane is converted thanks to SR in a large part of the monolith. Less evidence in the production of CO is due to the WGS reaction occurring at the same time.

At λ = 0.9963, it is possible to highlight two different trends in methane consumption perfectly matched by the profile of oxygen concentration. In the first section of the catalyst, up to 16 mm, a slower oxidation seems to be responsible for methane conversion. After this point, a sharp increase of CH_4 consumption rate is observed until oxygen has been completely depleted at x = 20 mm. After this section of the monolith, steam reforming of methane continues, as evidenced by the increase of H_2 concentration, until almost complete conversion.

To better characterize the behaviour of methane, a simple quantification can be provided assuming a pseudo-1st-order kinetic reaction [59] and solving an isothermal PFR mass balance:

$$r_{CH_4} = -\frac{dC_{CH_4}}{dt} = -k^{app} \cdot C_{CH_4}$$

(3. 10)

Where:

$$C_{CH_4} = y_{CH_4} \cdot C$$

(3. 11)

$$t = \frac{x}{v}$$

(3. 12)

With:

- r_{CH_4} = methane conversion rate [mol/m^3/s] ;
- C_{CH_4} = methane molar concentration [mol/m^3] ;
- C = total molar concentration [mol/m^3] ;
- k^{app} = apparent reaction rate constant [1/s] ;

Assuming constant velocity along the catalyst axis and approximating the derivative, the Equation (3.12) can be rewritten as:

$$\frac{k^{app}}{v} = -\frac{1}{y_{CH_4}} \cdot \frac{\Delta y_{CH_4}}{\Delta x} \tag{3. 12}$$

With this pseudo-1st-order kinetic reaction model, we can see that the methane oxidation apparent rate constant increases by one order of magnitude at x = 16 mm, as showed in Figure 3.8.

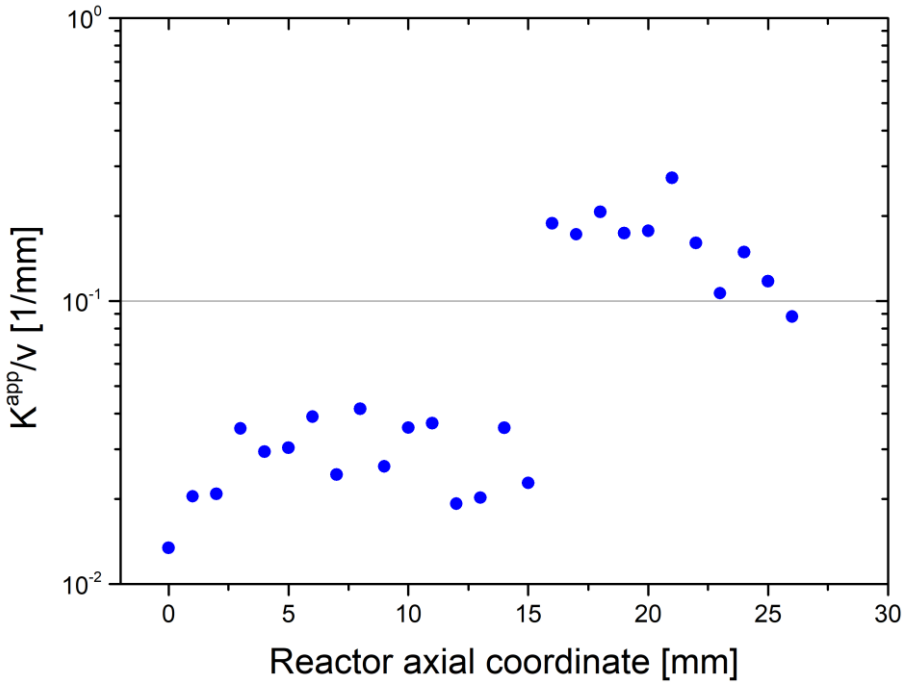

Figure 3. 8 – Methane oxidation apparent rate constant at T_{oven} = 450 °C, 10% of water and λ = 0.9963

According to achievements of a previous thesis work [60], it seems that in slightly rich conditions a change in methane oxidation rate of reaction occurs at a critical oxygen partial pressure equal to 0.0015 atm, when T_{oven} = 450 °C. Data also shows that k_{app} goes down again once oxygen is completely consumed and methane consumption due to SR becomes predominant, showing a third regime. Unfortunately, measurements close to complete methane conversion are influenced by strong oscillations, due to the small concentration differences, that make k_{app} calculation uncertain.

Our study provides additional support for the results reported in [61]: Chin et al. propose a correlation between the temperature and the O_2 partial pressure at which transition metallic Pd – Palladium oxide phase occurs (Figure 3.9). At T = 450 °C, it coincides with the O_2 concentration threshold at which methane conversion rate increases. Therefore, it is highly probable that the boost in methane conversion is related to a rearrangement of the Palladium-based catalyst, which improves the oxygen mobility at the catalyst surface.

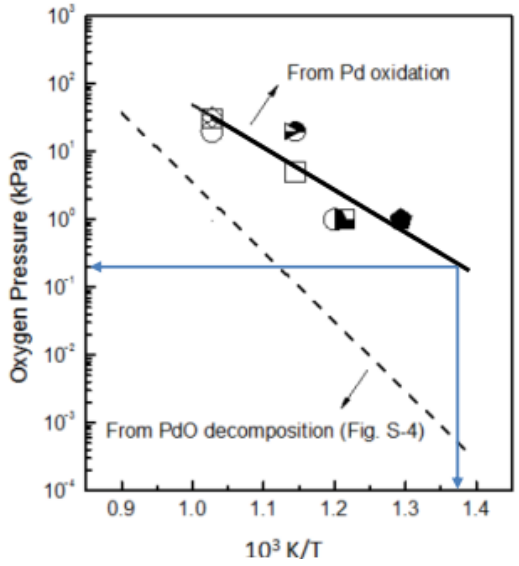

Figure 3. 9 – Correlation between temperature and critical oxygen partial pressure at T = 450 °C [61]

An alternative explanation may involve the activation of an "enhanced SR" as proposed by Wang et al. [62], that attributed this phenomenon to the desorption of carbonaceous species from ceria sites which normally hinder the rate of SR reaction. Correspondingly, the oxygen consumption is boosted by the oxidation of hydrogen and carbon monoxide formed by "enhanced SR", which are in fact observed only when O_2 is completely depleted.

At $\lambda = 0.99$, the absence of a large region where the methane oxidation is predominant, does not allow to show the trend variation in CH_4 oxidation rate, which likely occurs in the very first zone of the monolith.

3.2.2. Effect of temperature

First, it is worth to show a graph where downstream methane conversion and downstream hydrogen production are reported (Figure 3.10). These data are reported for each λ investigated, respectively at 400 °C, 425 °C and 450 °C.

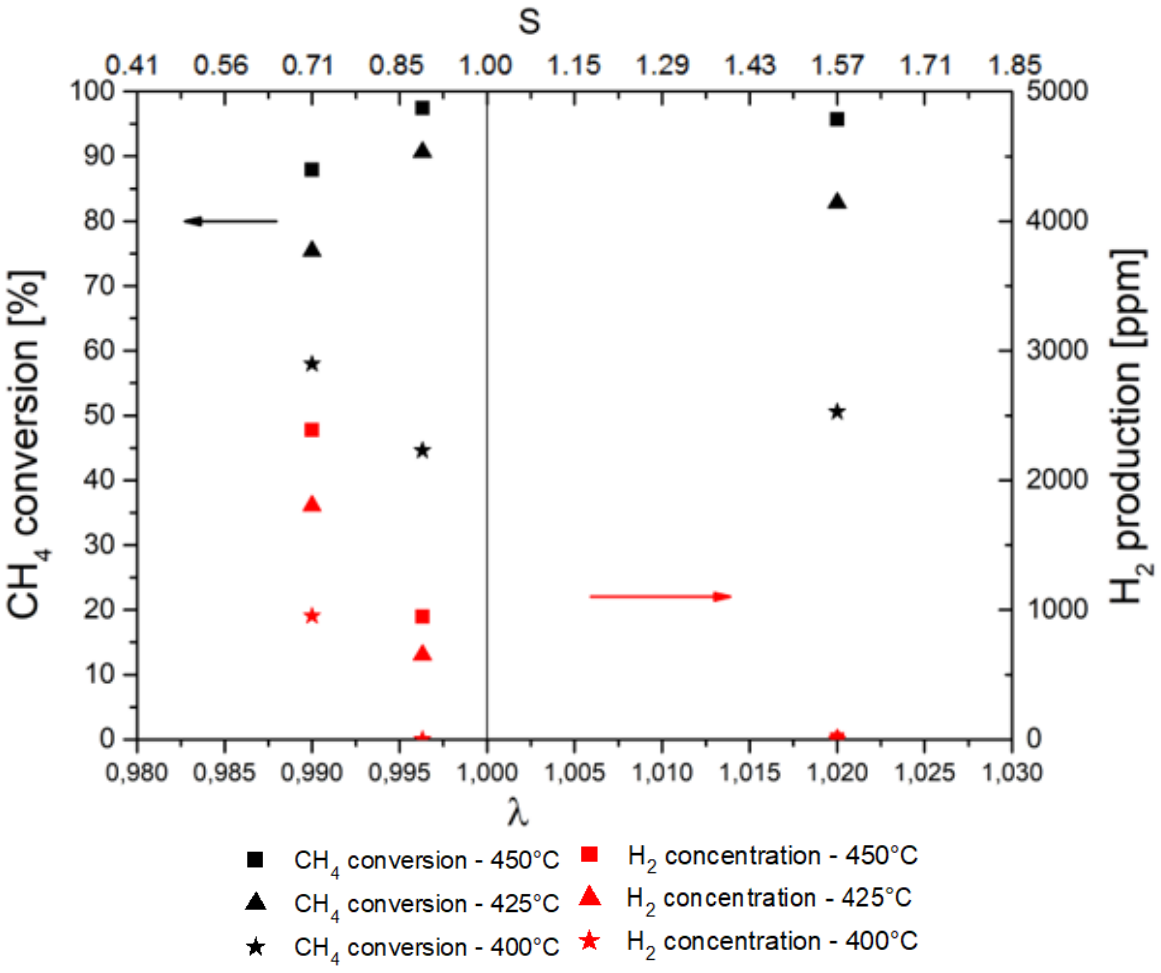

Figure 3. 10 – Downstream CH_4 conversion and H_2 production, at 10% H_2O, T = 450, 425, 400 °C, λ = 1.02, 0.9963, 0.99

Looking at downstream CH_4 conversions, passing from λ = 0.99 to λ = 0.9963, both at 450 °C and 425 °C methane conversion increases, while at 400 °C it decreases. Correspondingly steam reforming does not occur at λ = 0.9963, 400°C. In fact in these conditions hydrogen production remains equal to zero.

In Figure 3.11, it is possible to see the temperature profiles at T_{oven} = 400 °C:

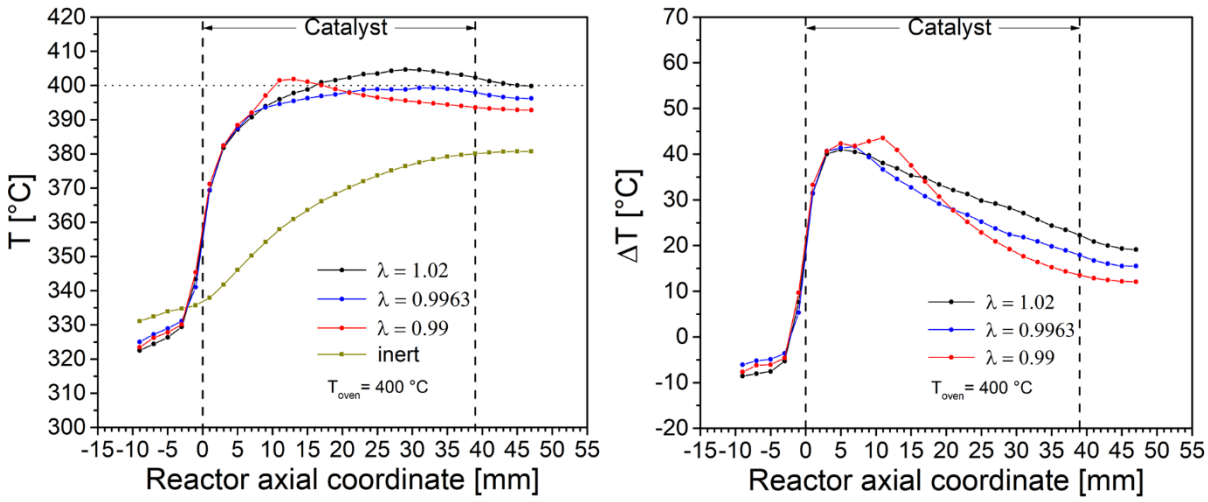

Figure 3. 11 – Temperature profiles at T_{oven} = 400 °C and 10% of H_2O

No significant deviations were found in the temperature profiles: also at 400 °C trends are similar in the first millimeters, where oxygen consumption is related to H_2 and CO oxidation. Both the profiles at λ = 1.02 and λ = 0.9963 exhibit a peak at the same axial coordinate. However, at λ = 1.02 higher temperatures are kept due to larger amount of oxygen that sustains the methane oxidation reaction.

At λ = 0.99, the peak is shifted towards right, where oxygen is completely consumed due to CO oxidation. Then, temperature decreases more rapidly, compared to the other two profiles, matching perfectly the concentration behaviour showed in Figure 3. 12. In fact, between x = 0 and x = 18 coordinates, methane conversion is slow, so once CO is completely burnt (x = 12) a steep gradient of temperature is clear. Starting from x = 18, the critical oxygen concentration is reached, methane conversion is pushed up and the gradient of temperature becomes less steep. The final part of the profile is the result of SR and WGS.

In Figure 3.12, concentration profiles at the studied λ (1.02, 0.9963, 0.99) are reported when T_{oven} = 400 °C at 10% water content:

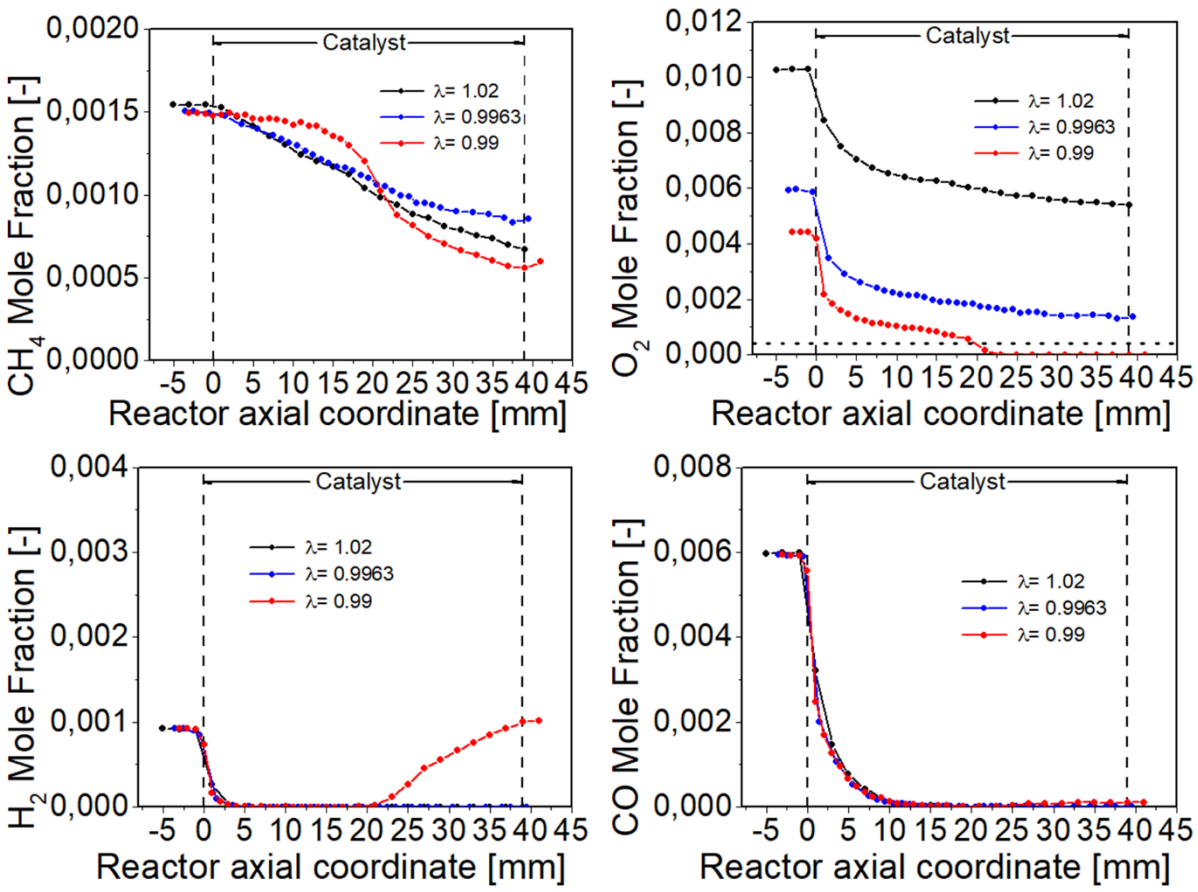

Figure 3. 12 – Concentration profiles and at T_{oven} = 400 °C and 10% H_2O

In line with previous results at higher temperature, no differences are visible in the oxidation of CO and H_2, which are unsensitive to temperature, suggesting an external mass diffusion control. On the other hand, methane conversions are reduced at all λ values, since the involved reactions are kinetically unfavoured by the temperature decrease. In this new set of experimental data, neither the CH_4 consumption rate transition nor SR occur at λ = 0.9963, this is because the temperature is not enough to sustain CH_4 conversion and, consequently, bring O_2 concentration down to the level required for the regime transition which allows to reach the complete consumption of oxygen.

At λ = 0.99 SR occurs, but it is penalized both thermodynamically and kinetically; oxygen needs more time to be completely consumed so SR start is postponed (x = 22 mm), while at T = 450 °C it already occurs in the first millimeters of the reactor. CO is formed but in small quantities, while H_2 production is more evident probably due to water gas shift reaction.

It is worth to notice that the fully-rich mixture shows a sudden change in methane depletion rate, like the λ = 0.9963 test at 450 °C. The oxygen partial pressure at which methane conversion rate increases, in this case, is around 0.4 mbar.

By assuming the pseudo-1st-order kinetic reaction model, the apparent kinetic constant of CH_4 oxidation rate at $\lambda = 0.99$ can be computed (Figure 3.13).

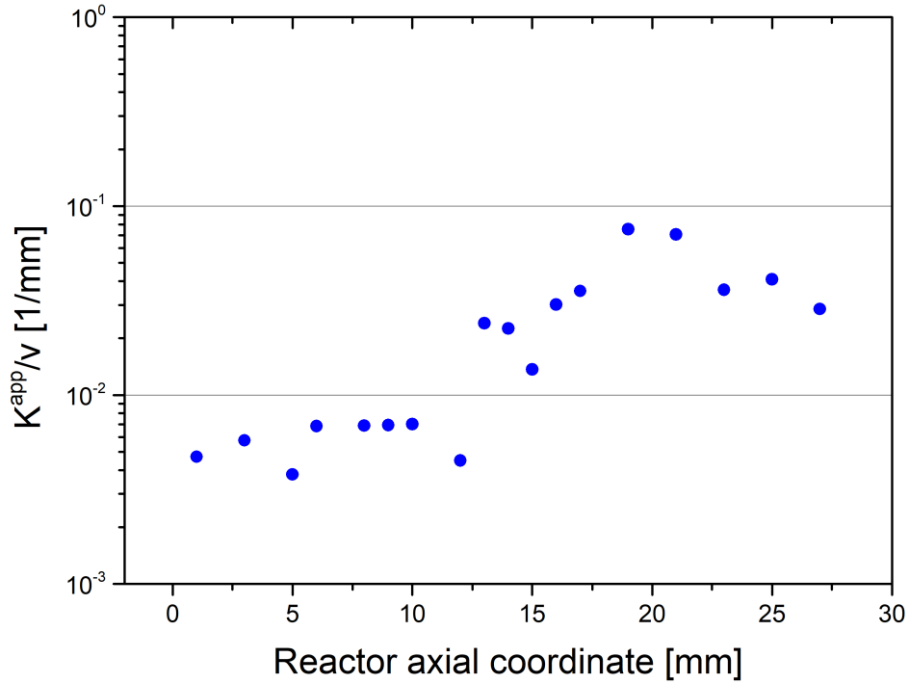

Figure 3. 13 – Methane oxidation apparent rate constant at T_{oven} = 400 °C, 10% of water and $\lambda = 0.99$

Also here, k^{app}/v exhibits one order of magnitude increase in the 16-24 mm region where the regime transition is observed. As can be observed in Figure 3.14, the results correlate satisfactorily well with the correspondence between temperature and critical oxygen value previously mentioned [61].

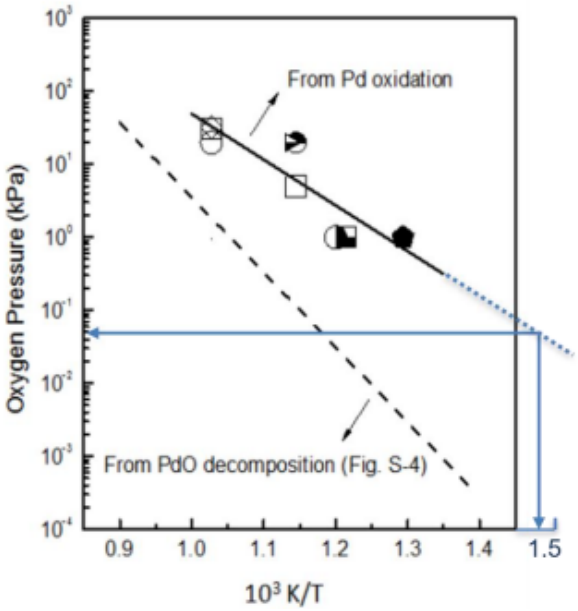

Figure 3. 14 – Correlation between temperature and critical oxygen partial pressure at T = 400 °C [61]

3.2.3. Effect of water

As already acknowledged, Pd-based catalysts suffer from water poisoning. Water tends to create stable surface hydroxides that inhibits the active sites of the catalyst. To investigate this effect, an experimental campaign was performed by keeping the temperature equal to 400 °C. For each of the three selected feeding mixtures in the spectrum of lambda (1.02, 0.9963, 0.99), the three conditions tested, in terms of water content, were:

- y_{H_2O} = 10 vol%
- y_{H_2O} = 2 vol %
- y_{H_2O} = 0 vol %

The complete framework in terms of downstream methane conversion and hydrogen production versus lambda is illustrated in Figure 3.15.

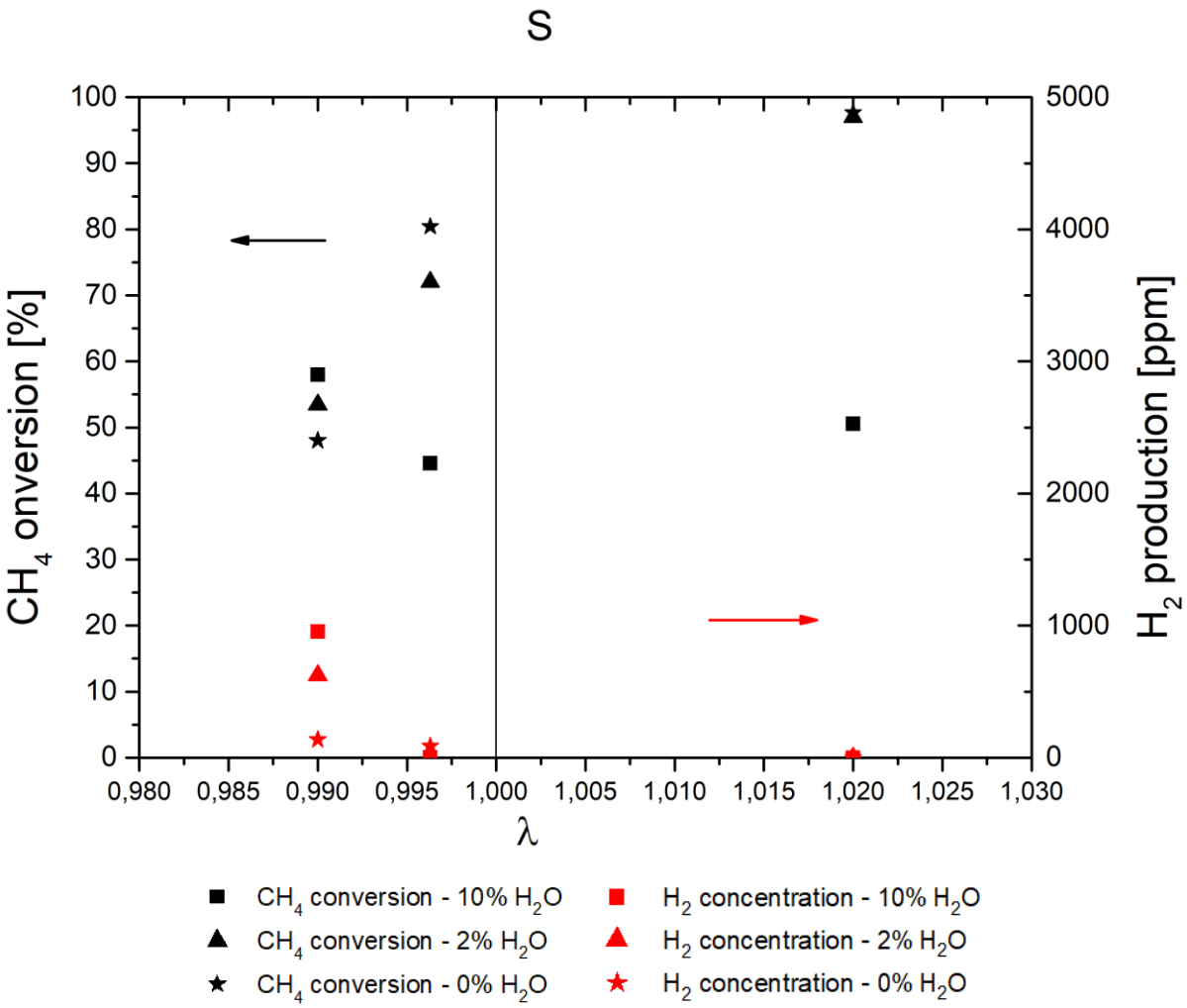

Figure 3. 15 – Downstream CH_4 conversion and H_2 production, at 400 °C, %H_2O = 10, 2, 0%, λ = 1.02, 0.9963, 0.99

For $\lambda > 1$, hydrogen production is always null independently on the water feed content due to the excess of O_2 that makes only oxidative reaction pathways possible. As it regards methane, a substantial gap is observed between the conversions achieved at low feed water concentration and the one at 10% of water. Remarkably, this gap becomes less and less pronounced when entering the rich window towards the richest condition, where the trend is inverted at $\lambda = 0.99$.

While, as previously discussed, with the highest amount of water, the minimum conversion of CH_4 is achieved at $\lambda = 0.9963$, with low amount of water in the feed the CH_4 conversion monotonically decreases with λ.

To gain insight on water effect, spatially resolved temperature and concentration profiles were collected for each value of λ. The objective is to define the impact of water content on the reactants behaviour throughout the entire reactor.

Temperature profiles for a lean-fuel mixture ($\lambda = 1.02$) at 400 °C are reported in Figure 3.16:

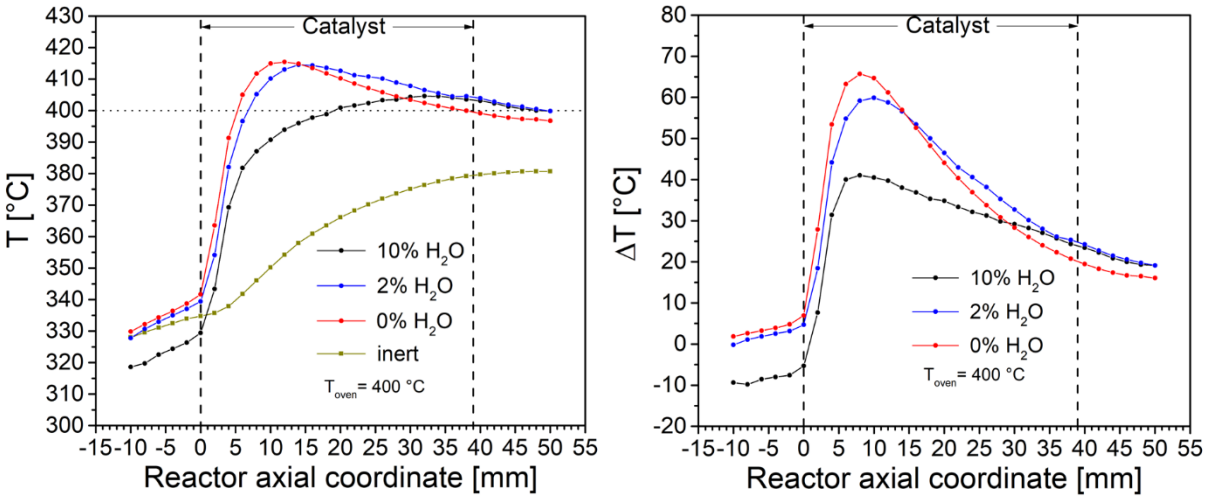

Figure 3. 16 – Temperature profiles at T_{oven} = 400 °C and $\lambda = 1.02$, effect of H_2O

In all tests the temperature is controlled only by the methane, carbon monoxide and hydrogen oxidation reactions.

At 0% and 2% of water content, again, the situation is quite similar: a steep increase due to CO and H_2 combustion, responsible for the peak around x = 10 mm, followed by a slow decrease where only CH_4 consumption controls the temperature.

With the higher concentration of feed water in the gas phase, the concentration of hydroxides species on the catalytic surface is coherently higher, resulting in inhibition of CH_4 oxidation. This is perfectly matched by the lower peak observed in the temperature profile at 10% feed water. Despite this, towards the end of the catalyst

this profile shows a higher temperature then the 0% test, this is probably because in the dry test all the methane concentration drops to zero at around x = 27 mm, then there is no residual fuel to be burnt.

It can be also noticed that at 10% the reactants temperature, before entering in the reactor, is 10° C lower if compared to the dry mixture possibly due to the higher specific heat of the feed gas.

Figure 3.17 shows the influence of water at λ = 1.02 and 400 °C on concentration profiles:

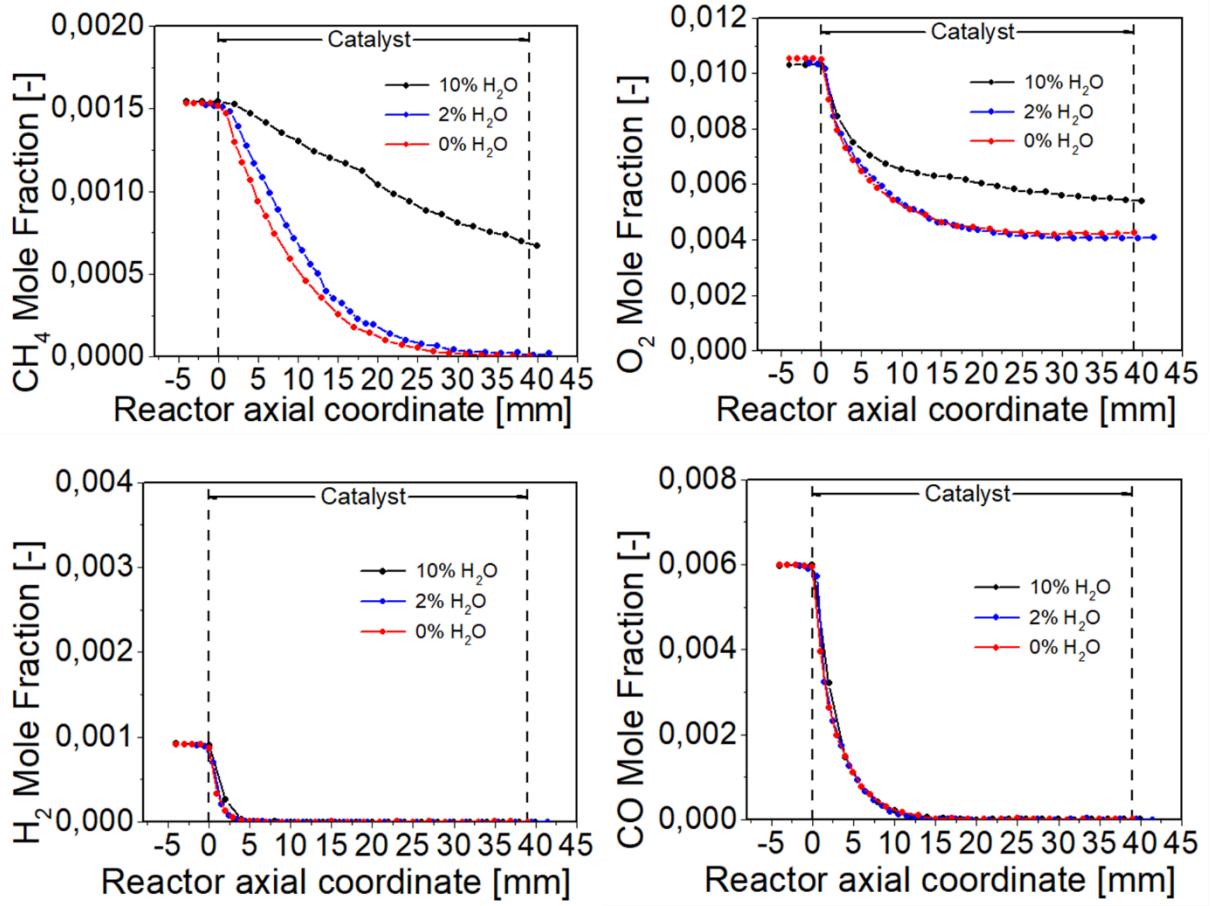

Figure 3. 17 – Concentration profiles at T_{oven} = 400 °C and λ = 1.02, effect of H_2O

CO and H_2 seem to be independent of the water content in the mixture, no differences are visible in their concentration profiles.

At 2% of water, there is a small reduction in the rate of CH_4 consumption in the first half of the profile, but in both 0% and 2% feed water conditions complete downstream

methane conversion is practically reached, making it difficult to assess the real impact of the presence of water.

At 10%, the feed water inhibition effect is evident. Methane conversion strongly decreases along the whole reactor length. At the monolith outlet the methane conversion is practically halved. Such inhibitory effect has been observed by many research groups, all hypothesising that Pd supported on alumina can form $Pd(OH)_x$ species in a wet environment, which hinder the catalyst activity.

The effect of water feed concentration for a slightly rich feed (λ = 0.9963) at 400°C is shown in terms of reactants temperature in Figure 3.18:

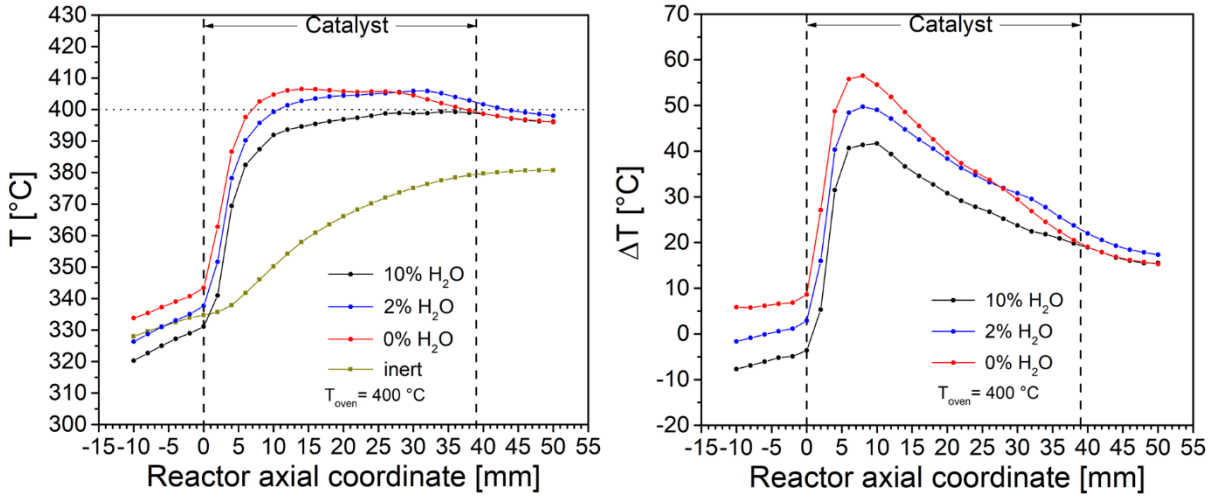

Figure 3. 18 – Temperature profiles at T_{oven} = 400 °C and λ = 0.9963, effect of H_2O

As it concerns the thermal behaviour, at the beginning of the reactor, once the H_2 is completely burned, the 0% mixture reaches the highest temperature, coherently with the higher methane oxidation rate of reaction than in the other profiles. Then, ΔT tends to decrease due to the early start of SR reaction. Looking at the temperature profiles, a practically flat behaviour is obtained, due to the combination of heat losses and heat released by reactions.

Turning now to the 10% H_2O feed test, water poisoning reduces the temperature throughout the reactor. At the end of the honeycomb, all profiles reach similar temperatures, a little bit higher for the 2% mixture maybe due to the low exothermicity of the WGS reaction.

Concentration profiles at λ = 0.9963 and 400 °C are now reported, respectively for wet, slightly-wet and dry conditions in Figure 3.19.

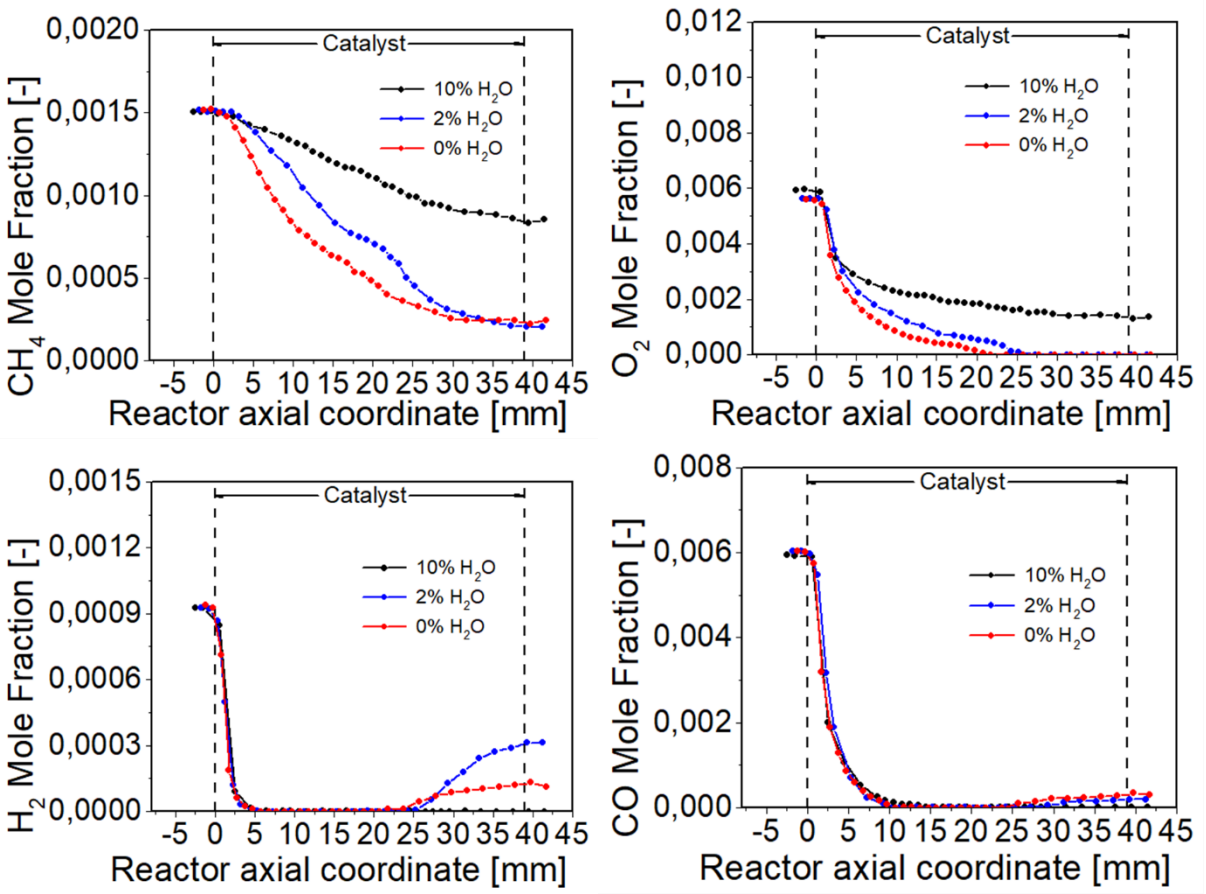

Figure 3. 19 – Concentration profiles at T_{oven} = 400 °C and λ = 0.9963, effect of H_2O

While H_2 and CO concentration profiles are invariant as usual, at 10% of water, the methane conversion is strongly inhibited due to the water poisoning: CH_4 and O_2 are consumed with a slow rate of reaction. As a result, oxygen is not completely consumed and SR reaction does not occur. Between 2% and 0% differences are more visible at λ = 0.9963 rather than in lean conditions previously described. Methane conversion in clearly penalized at 2%, in fact oxygen needs more reactor length to approach zero concentration. Consequently, SR and WGS reactions start from a more advanced reactor axial coordinate. It is interesting to notice that, at the end of the reactor, H_2 concentration is higher at 2% of water than 0%, while it is the opposite for CO. This is the consequence of the higher percentage of water, that pushes the water gas shift reaction towards products. The percentage of water seems to not affect the partial pressure of oxygen at which the acceleration of methane rate of reaction is observed: the 2% O_2 profile is shifted toward right (compared to 0% profile) but the threshold seems to be at the same partial pressure, already found under rich conditions (λ = 0.99) at 400 °C. Of course, at 10% water content, the variation of the trend is not visible because the consumption rate is so slow that the O_2 critical partial pressure is not reached.

Temperature profiles at λ = 0.99, for each percentage of water, are reported in Figure 3.20:

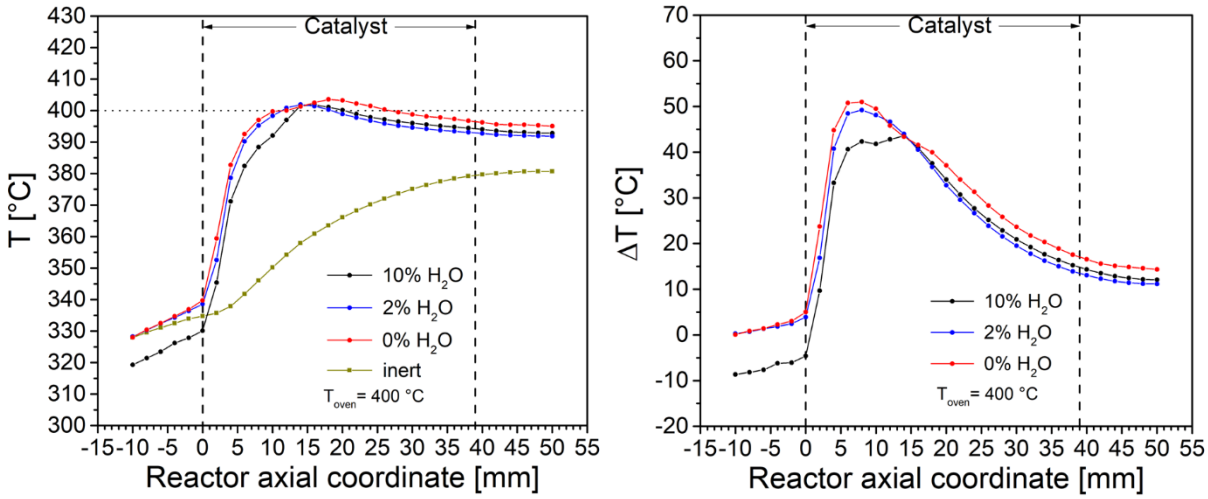

Figure 3. 20 – Temperature profiles at T_{oven} = 400 °C and λ = 0.99, effect of H_2O

At 10% of water, especially in the ΔT graph, two peaks are clearly visible. This is due to the change of the rate of methane consumption. At 2%, it is not so clear, probably because the region where methane conversion is accelerated is too small.

From approximately x = 20 mm until the end of the reactor, the 0% mixture exhibits the highest temperature due to the lower steam reforming endothermic contribution.

Concentration profiles collected at λ = 0.99 and 400°C are reported in Figure 3.21.

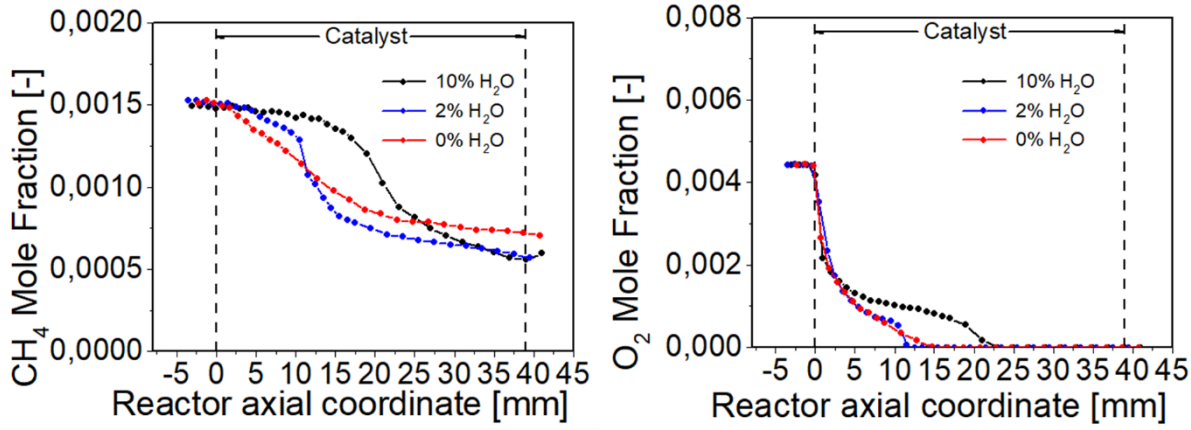

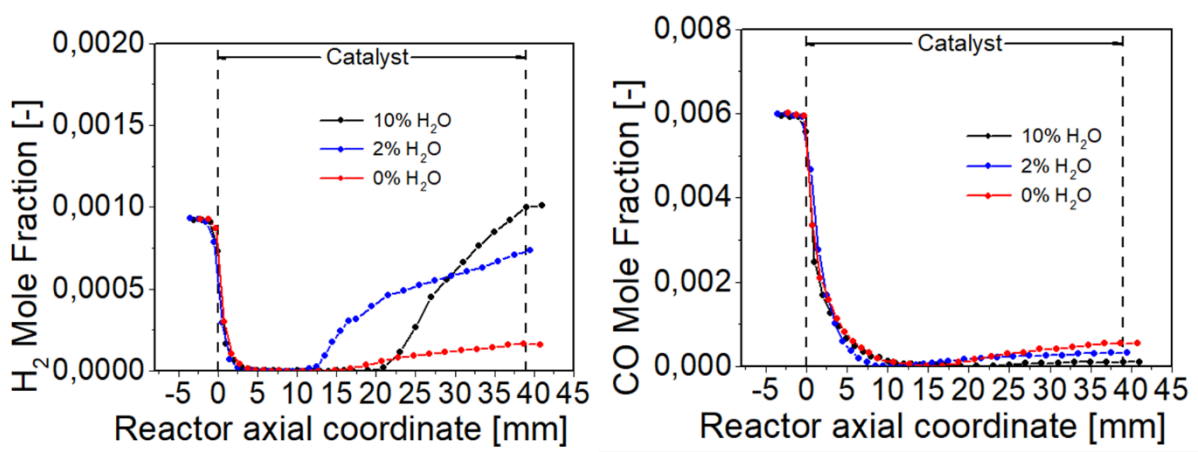

Figure 3. 21 – Concentration profiles at T_{oven} = 400 °C and λ = 0.99, effect of H_2O

Also at this oxygen concentration, the CO and H_2 oxidation is not affected by the water content. In all tests, oxygen is completely consumed, which is consistent because the feed mixture is rich.

At both 2% and 10% water content, methane rate of reaction shows two different regimes. It is interesting to notice that, in both cases, the oxygen threshold occurs at the same partial pressure. This is coherent with the profiles at λ = 0.9963: the water content does not affect the oxygen concentration at which methane conversion rate is increased.

3.3. CH_4 feed

The second experimental campaign has been performed testing only methane as fuel. The CO and H_2 contents were replaced with an equivalent amount of CH_4 (1/4 on a molar basis) in order to keep constant the stoichiometry for O_2 consumption. In Table 3.5, the general composition of the feed mixture is reported:

Table 3. 5 – Species concentrations of the mixture used during the second campaign

Species	**CH_4**	**H_2**	**CO**	**H_2O**	**O_2**	**CO_2**	**N_2**
y_i [vol %]	0.325	0	0	0 - 10	0.46 – 1.03	10.7	Balance

Different conditions were tested, by varying temperature, oxygen concentration and water feed content.

In Table 3.6 a list of the experiments carried out with the CH4-CO-H2 fuel is reported:

Table 3. 6 – List of experiments performed by feeding CH_4 as fuel

λ	**S**	**T [°C]**	**CH_4**	**H_2**	**CO**	**H_2O**	**O_2**	**CO_2**	**N_2**	**Pulses**
1.02	1.57	450	0.325	0	0	10	1.03	10.7	Balance	Yes
1.02	1.57	400	0.325	0	0	10	1.03	10.7	Balance	Yes
1.02	1.57	450	0.325	0	0	0	1.03	10.7	Balance	No
1.02	1.57	400	0.325	0	0	0	1.03	10.7	Balance	Yes
0.9963	0.89	450	0.325	0	0	10	0.58	10.7	Balance	Yes
0.9963	0.89	450	0.325	0	0	0	0.58	10.7	Balance	No
0.99	0.71	450	0.325	0	0	10	0.46	10.7	Balance	No
0.99	0.71	450	0.325	0	0	0	0.46	10.7	Balance	No

3.3.1. Effect of water

The effect of water inhibition has been investigated by focusing for each of the representative lambda (1.02, 0.9963, 0.99) on two limit percentages of water co-feed:

- y_{H_2O} = 10 vol %
- y_{H_2O} = 0 vol %

Downstream results, in terms of methane conversion and hydrogen production, are showed in the following graph (Figure 3.22):

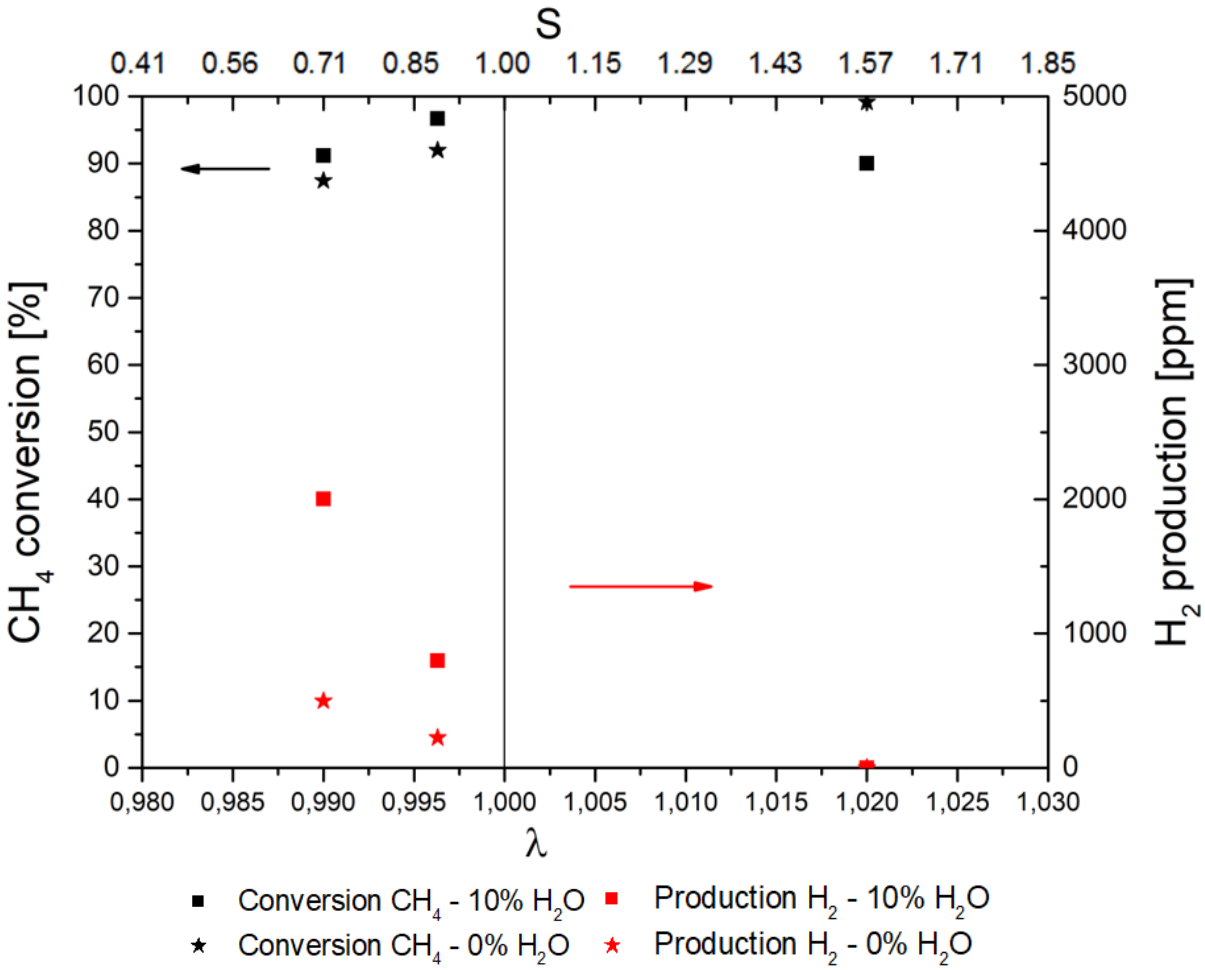

Figure 3. 22 - Downstream CH_4 conversion and H_2 production, at 450 °C, %H_2O = 10, 0%, λ = 1.02, 0.9963, 0.99

Under lean conditions, the wet mixture has a 10% lower downstream methane conversion, due to water inhibition, which severely impairs the activity of the Pd-based catalyst. This is coherent with the fact that methane consumption is only related to CH_4 oxidation: steam reforming and water gas shift do not occur because of the oxygen excess, as confirmed by the H_2 production that equals zero.

Moving to rich and slightly rich conditions, the observed trend is exactly the opposite. In this situation water is still an inhibiting factor in the oxidation zone, but as soon as O_2 is completely depleted, SR can take place. It is evident that there is a tradeoff between the two reactions: if water content is increased, methane oxidation is unfavoured at the advantage of steam reforming. In the rich window of lambda, the SR improvement overcomes the activity reduction for water poisoning. As a result, the downstream methane conversion increases with 10% water content.

In a recent work from Coney et al. [63], it has been reported the evidence that under lean wet conditions, the lower the reaction temperature, the higher impact of water inhibition. In order to achieve further proof of the aforementioned phenomenon, the effect of water along the reactor has been investigated in this thesis at the reference lean lambda (λ = 1.02), at two oven temperatures (400 °C and 450 °C).

In Figure 3.23, both methane concentration and temperature profiles along the catalyst are reported at each of the two experimented temperatures: T_{oven} = 450 °C (a, b) and 400 °C (c, d):

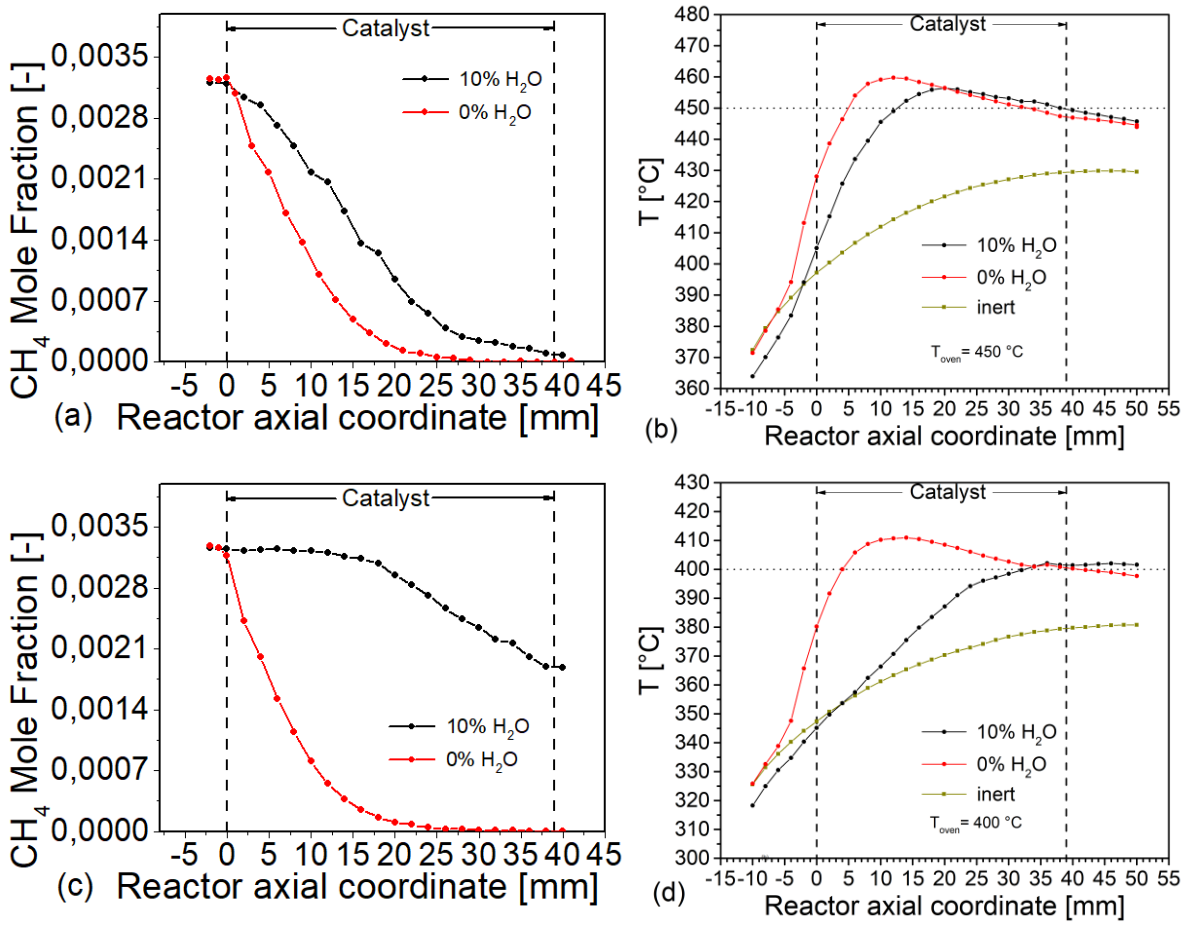

Figure 3. 23 – Methane concentration as a function of axial position at 450 °C (a) and 400 °C (c). Gas temperature as a function of axial position at 450 °C (b) and 400 °C (d)

Looking at plots (a) and (c), it is clearly visible that lower levels of inhibition are obtained at an oven temperature of 450 °C, compared to 400 °C.

At 450 °C, under dry feed practically all methane is consumed, while, at 10% water content, a methane conversion equal to around 90% is reached.

At 400 °C, in panel (b) it is clearly visible that the methane conversion is highly inhibited when 10% of water is co-fed. This is due to a combined effect in which water inhibition and the reaction temperature act synergistically. The high percentage of water, coupled with the low oven temperature, is responsible for the initial low catalytic activity. Only a small amount of the fuel fed can react, so that the heat released by the oxidation reaction is initially very limited. The lower reaction temperature results in a lower rate of methane consumption. Accordingly, water inhibition and thermal effects influence negatively each other, resulting in a markedly lower overall conversion via methane oxidation (40% with wet feed vs 100% with dry feed).

Further investigations are needed to deeply understand how the water inhibition is influenced by the temperature. Nevertheless, the results of this work show in general a good agreement with the aforementioned previous scientific communications.

In the following, the experiments carried out in the rich window of lambda are described.

Temperature profiles under slightly-rich mixture, at T_{oven} = 450 °C, are showed in Figure 3.24:

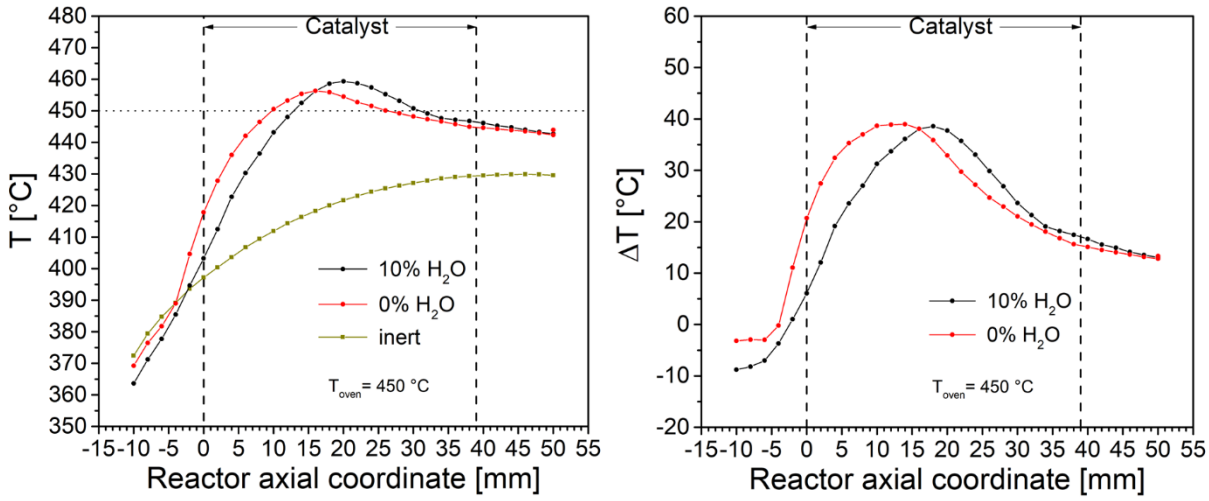

Figure 3. 24 – Temperature profiles at T_{oven} = 450 °C and λ = 0.9963, effect of H_2O

In these conditions, the water inhibition effect is visible in the first part of the reactor. In dry conditions, the methane oxidation rate of reaction is higher and, as a consequence, temperature increases more rapidly.

Differently from lean conditions, focusing on the ΔT profiles, the maximum of the peak of the heat released by the reaction is similar but shifted towards right under wet conditions.

In the last part of the monolith, no differences in terms of temperature are practically visible.

The concentration profiles of the reactants at $\lambda = 0.9963$ are reported in Figure 3.25:

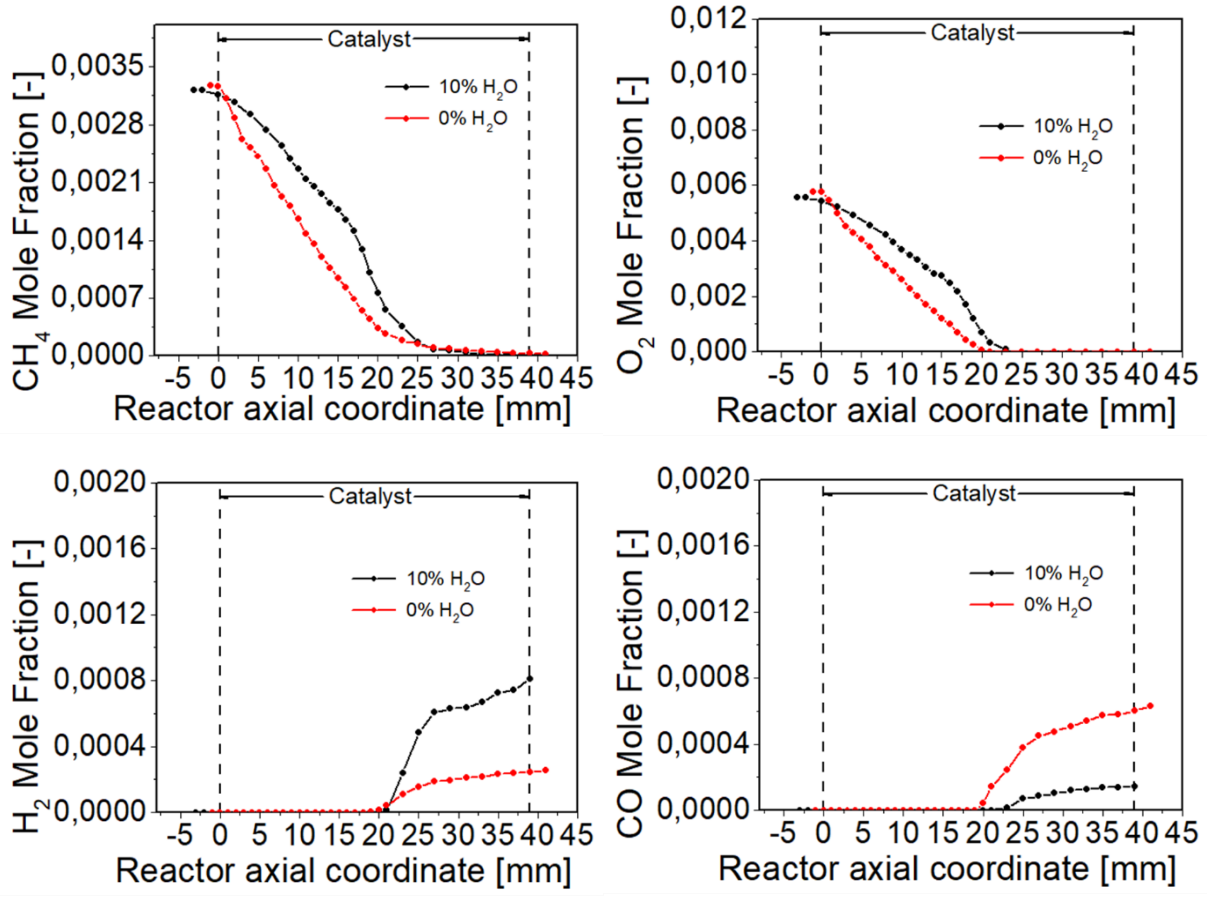

Figure 3. 25 – Concentration profiles at T_{oven} = 450 °C and $\lambda = 0.9963$, effect of H_2O

In the first part of the reactor, the inhibition effect of water is evident: the methane conversion starts slowly when H_2O is co-fed. Once oxygen is totally consumed, the rate of methane consumption becomes almost comparable in the two conditions. Then, steam reforming reaction occurs in both experiments and practically equal downstream CH_4 conversions are obtained.

Looking at CO and H_2 profiles, the impact of WGS reaction is evident. When 10% water is co-fed, hydrogen concentration is always higher, while CO is lower compared to the dry feed: this is because the high percentage of water tends to react with CO to produce H_2 and CO_2, following the water gas shift reaction pathway. Two different rates in the hydrogen production seem to exist at 10% water content: between x = 21 to x = 27 mm there is a steep increase, then it becomes less evident. It is likely that when SR begins, the water content in flues gases is high and strongly pushes the water gas shift reaction towards products.

In wet conditions, an increase in methane oxidation rate is registered at x = 16 mm, similarly to what was observed in the presence of CO and H_2 cofeed. On the other hand under dry conditions the CH_4 consumption trend is regular and does major slope changes along the axial coordinate.

For further investigation concerning methane rate of consumption, the same approach introduced for the first campaign was adopted. By assuming a pseudo-1st-order kinetic reaction and solving an isothermal PFR mass balance, an apparent kinetic constant for methane consumption can be evaluated, as reported in Figure 3.26.

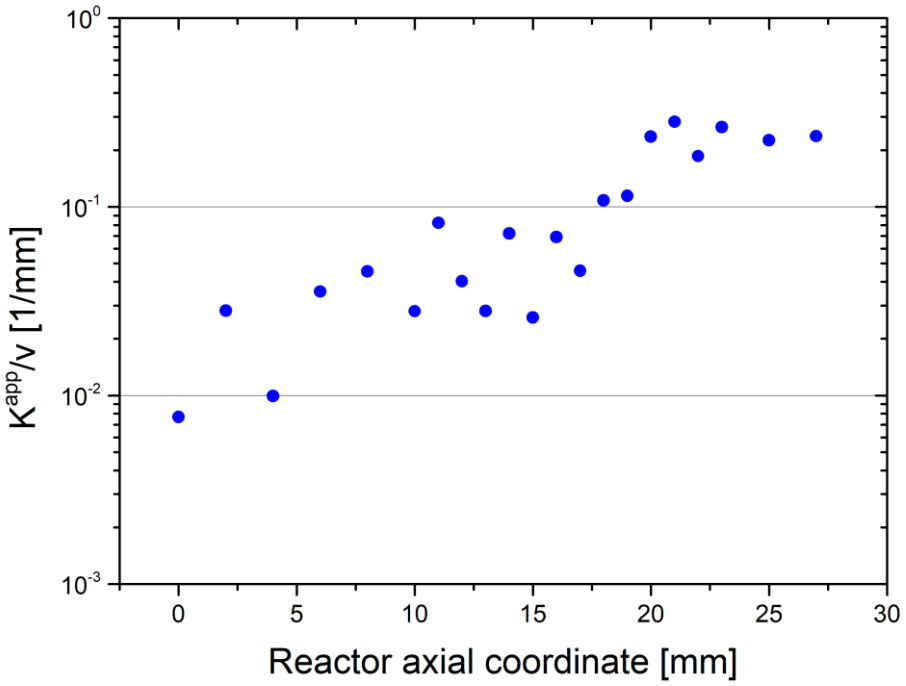

Figure 3. 26 – Methane oxidation apparent rate constant at T_{oven} = 450 °C, 10% of water and λ = 0.9963

Also in this case, an increase of the methane consumption rate of one order of magnitude is calculated. This boost in methane conversion occurs when the partial pressure of oxygen reaches around 2.5 mbar. During the first campaign, when the CH_4-CO-H_2 mixture was fuelled at the same oven temperature of 450°C, the oxygen threshold exhibited at around 1.5 mbar. It is quite challenging to comprehend the

reasons behind this deviation. Temperatures are quite similar in the region of the monolith where respectively the oxygen thresholds manifest (Figure 3.27), so that they seem not to be responsible for the different oxygen threshold.

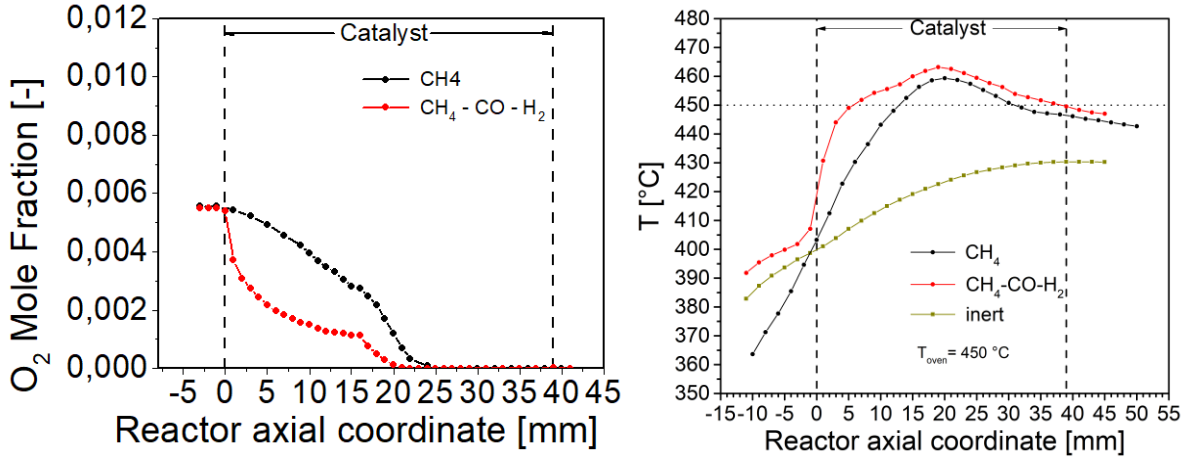

Figure 3. 27– O_2 concentration profile and temperature profile at T_{oven} = 450 °C, 10% H_2O and λ = 0.9963, comparison between fuels

Nevertheless, it is worth to highlight that, by considering absolute values, the discrepancy with respect to Chin et al. model (Figure 3.28) is not so dramatic: the difference in the O_2 partial pressure at which the threshold is observed (1.5 mbar for the CH_4-CO-H_2 mixture, 2.5 mbar for the pure CH_4) would correspond to a temperature difference of around 15 °C so that minor inaccuracies in temperature measurements (e.g differences between gas and solid temperatures) might be responsible for the observed deviation.

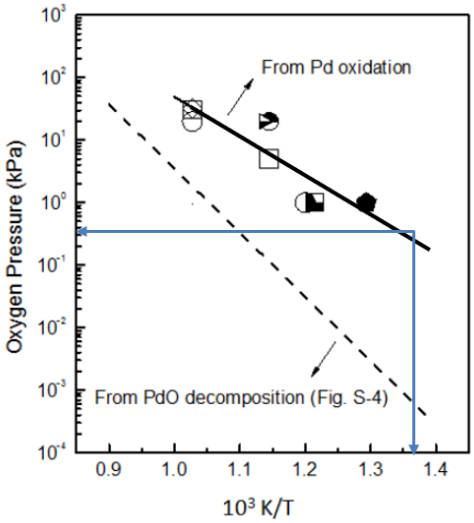

Figure 3. 28 – Correlation between temperature and critical oxygen partial pressure [61]

To complete the investigation of the effect of water content in rich conditions, temperature data at $\lambda = 0.99$ are reported in Figure 3.29, by keeping $T_{oven} = 450$ °C.

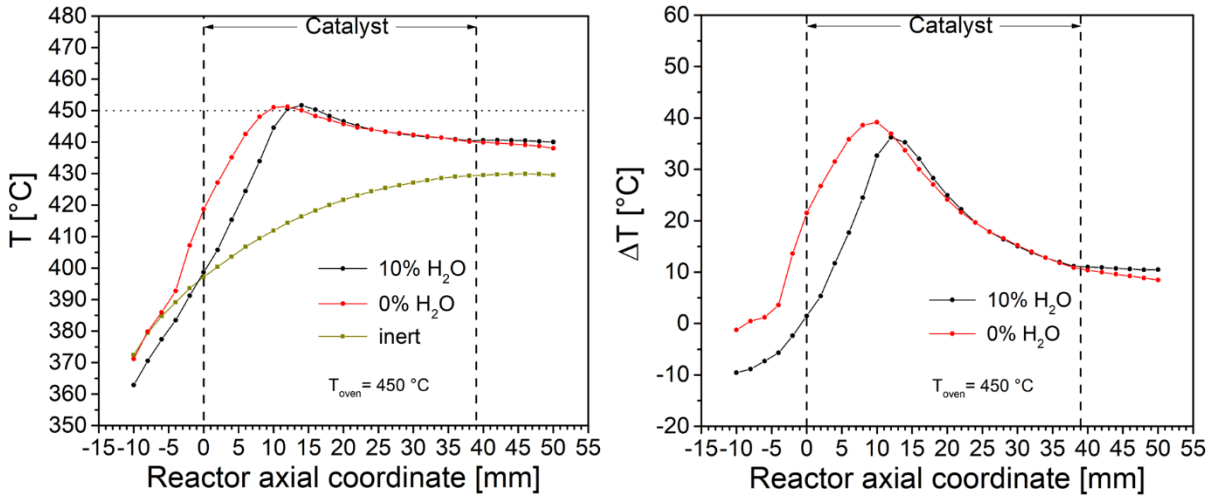

Figure 3. 29 – Temperature profiles at $T_{oven} = 450$ °C and $\lambda = 0.99$, effect of H_2O

At 10% water content, the temperature is lower with respect to the one in dry conditions throughout the first portion of the monolith. To be quantitative, at the coordinate x = 6 mm, a difference of almost 20 °C between the two mixtures is measured by the thermocouple. For both temperature profiles a peak is observed. After that, the profiles become practically aligned.

The correspondent concentration profiles of reactants for the richest mixture ($\lambda = 0.99$) are illustrated in Figure 3.30:

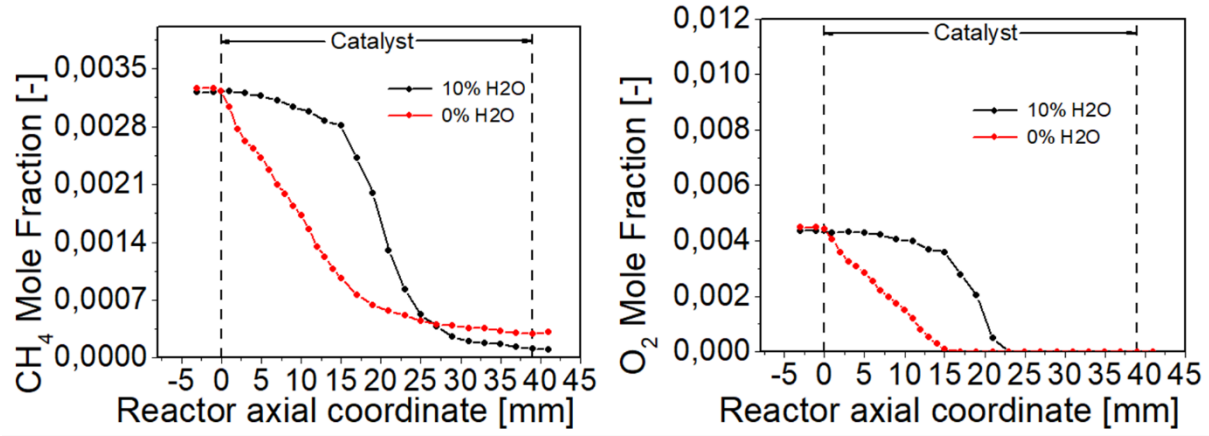

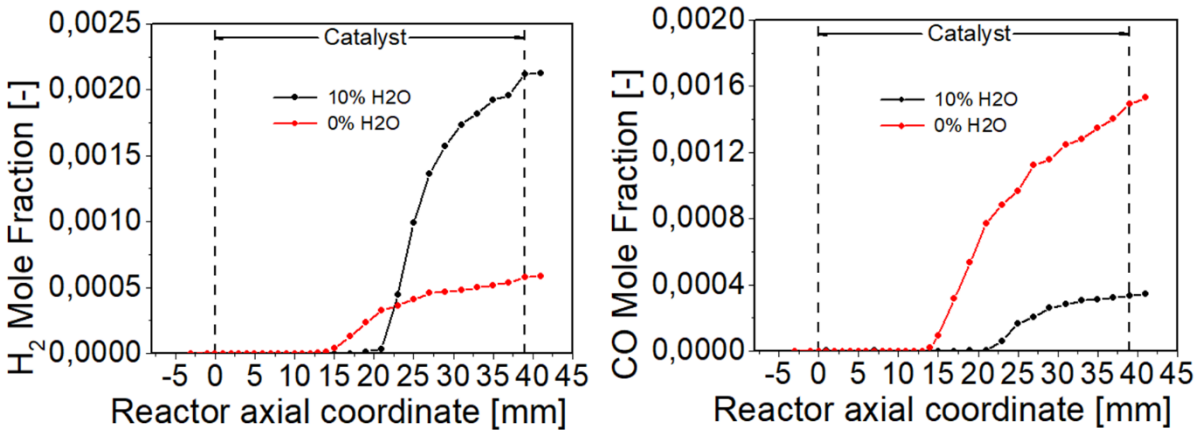

Figure 3. 30 – Concentration profiles at T_{oven} = 450 °C and λ = 0.99, effect of H_2O

At 0% water content, a liner trend in methane consumption is observed in the region controlled by the oxidation reaction. Then, once oxygen is totally consumed, at x=15 mm, SR and, to a limited extent, WGS occur.

At 10% water content, three different rate of methane conversion are clearly visible. In the first part of the reactor, methane is slowly converted due to the water inhibition and the low reaction temperature. Then, at x = 15-16 mm, a steep increase of the rate consumption of methane is exhibited which brings to complete O_2 consumption at x=22 mm. After this point SR and WGS occur. Looking at the CO and H_2 profiles, as in the tests with lambda equal to 0.9963, the large amount of feed water shift WGS equilibrium towards products. As a result, a high amount of hydrogen and a very low one of carbon monoxide are obtained at the outlet of the reactor.

By repeating the procedure already described, an apparent kinetic constant for methane consumption rate has been calculated along the monolith (Figure 3.31).

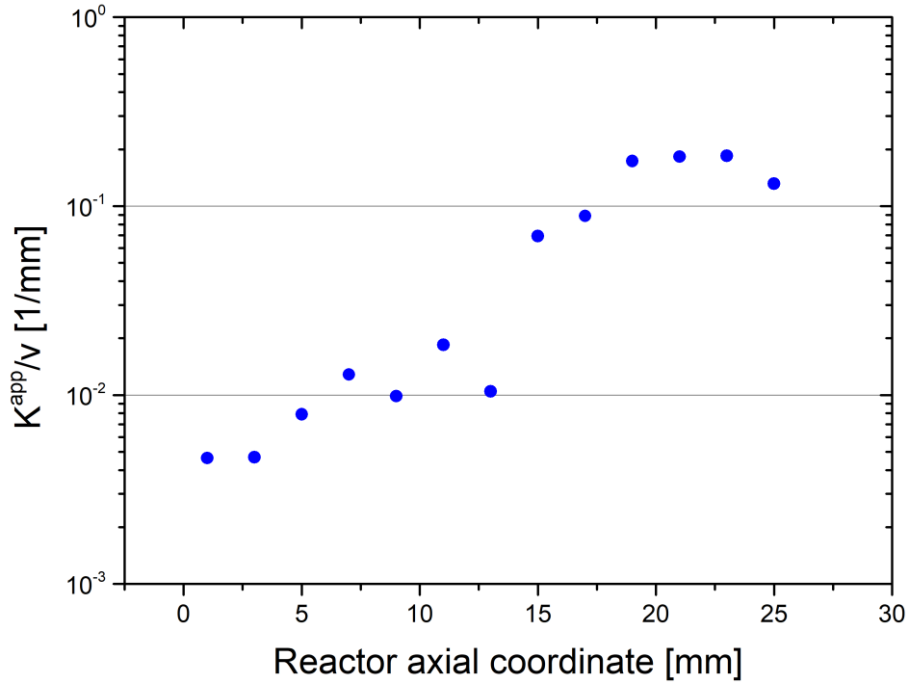

Figure 3. 31 – Methane oxidation apparent rate constant at T_{oven} = 450 °C, 10% of water and λ = 0.99

The increase of k^{app} is even more evident and steep in comparison to the experiment carried out at λ = 0.9963: starting from x = 15 mm it increases of one order of magnitude. Here, the oxygen threshold occurs at around 3 mbar, the double with respect to the value obtained for the first campaign.

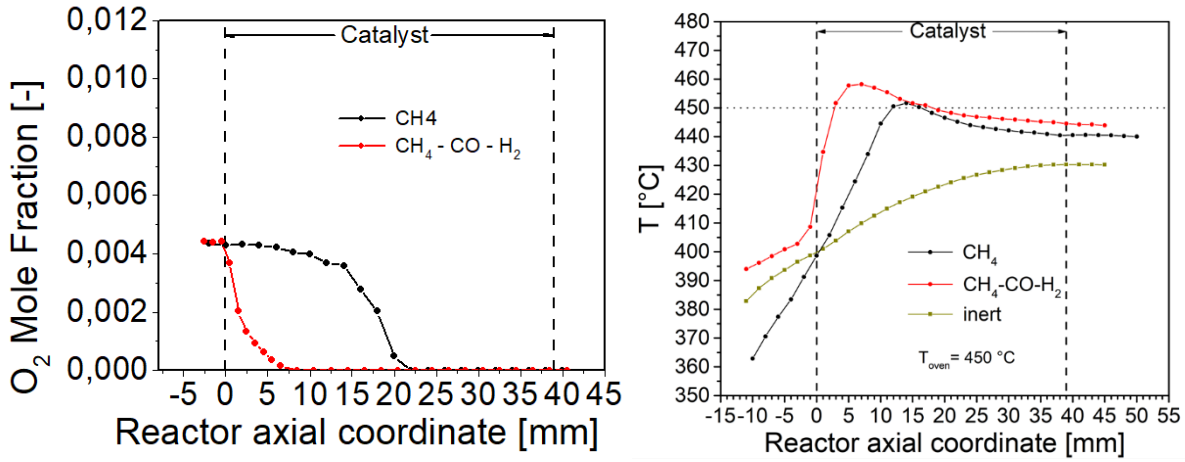

Figure 3. 32 – O_2 concentration profile and temperature profile at at T_{oven} = 450 °C, 10% H_2O, comparison between fuels

By focusing on the role of water, it is worth to highlight that in the first campaign the amount of water seemed not to affect the value of the O_2 concentration at which the increase of conversion rate was experienced. Nevertheless, it could be stated that the

presence of water itself has an impact on the onset of this threshold: with both fuels, no evidence of its occurrence has been found in dry tests.

Further investigations are needed to gain deeper understanding on the mechanisms behind this complex behaviour of the catalyst.

Conclusions

In this thesis work, the performances of a commercial Pd-Rh/Al_2O_3 catalyst for natural gas (or biomethane) fuelled vehicle, were investigated. The catalyst is characterized by a 7.1 g/L loading (Pd:Rh-39:1) and by the presence of cerium and zirconium oxide promoters, in order to increase the oxygen store capacity (OSC). The honeycomb catalyst sample used during experiments was 3.9 cm long which features 6 x 6 channels.

The catalyst samples were tested in an experimental set up equipped for collecting of spatially resolved concentration and temperature profiles. This was obtained by means of a sliding capillary inserted in the central channel of the honeycomb sample. The capillary was moved by a precise positioning sled system controlled by a linear actuator. Local gas sampling and a thermocouple allowed to measure axial concentration and temperature profiles.

The experimental activity aims to investigate the behaviour of the catalyst under a range of different conditions. The effect of temperature, water inhibition and fuel composition were investigated. The Pd-based catalyst might suffer from deactivation during the test time, depending on the experimental conditions. In those tests where a deactivation is registered, typically under lean conditions, periodic rich pulses were performed according to a procedure developed in previous studies. This protocol was successful in keeping constant the downstream CH_4 conversion confirming observed that periodic-rich pulses can help to restore the catalyst activity towards methane oxidation.

In the first experimental campaign, performed by feeding a mixture of CH_4/CO/H_2 as fuel with a composition representative of typical exhaust of a stoichiometric natural gas engine, the effect of temperature and water inhibition have been evaluated at different lambda values around the stoichiometric value.

At 450°C and 10% water content, downstream CH_4 conversion shows a maximum at slightly rich conditions (λ=0.9963). Axially resolved concentration profiles showed that under this condition there is a critical partial pressure of oxygen below which methane conversion rate increases by one order of magnitude and is responsible for the high overall methane conversion. One of the possible explanations refers to the formation of a more active Pd/PdO state. When performing the same experiments at 400 °C and 10% water content, the maximum downstream CH_4 conversion is obtained at richer conditions (λ=0.99). In fact, the O_2 partial pressure threshold where acceleration of CH_4

consumption rate is observed is still present but shifted towards a lower value, which is reached only at the richest investigated conditions. This suggests that there is a relationship between the critical oxygen concentration and the reaction temperature, in agreement with literature on PdO/Pd transition. As expected, CH_4 conversion decreases with the temperature under all the investigated conditions, consistently with the kinetic control of CH_4 consumption reactions.

As it concerns the investigation of water inhibition, at 400 °C under lean and slightly-rich conditions, where only oxidation reactions occur, passing from dry to wet feed tests methane conversion practically halved. On the other hand, under rich conditions, a higher methane conversion is achieved when 10% of water is co-fed: spatially resolved profiles reveal that water inhibition on CH_4 oxidation is still present but, once O_2 is completely consumed, SR is favoured by high water concentration. This suggests that there is a trade-off between the two effects.

On the other hand, H_2 and CO oxidation seem not to be affected by the different conditions: they are rapidly oxidized in the first millimeters of the monolith regardless temperature and water concentration, indicating that their consumption rates are under external mass diffusion control.

The second experimental campaign focused on water content and temperature effects, when only methane is fed as fuel. Results show that, under lean conditions (λ=1.02), the inhibition of the catalyst conversion performances is much higher at 400 °C than at 450 °C due to a combined effect in which water inhibition and the low reaction temperature act synergistically, lowering the performance of the catalyst. The high percentage of water, coupled with the low oven temperature, is responsible for an initial low catalytic activity. Only a small amount of the fuel fed can react, so that the heat released by the oxidation reaction is initially very limited. The lower reaction temperature results in a lower rate of methane consumption. Under slightly-rich and rich wet conditions at 450°C, an oxygen threshold at which methane conversion rate is increased has been found. However, the O_2 partial pressure at which such regime transition occurs is slightly higher than the one observed during the first campaign when the CH_4-CO-H_2- fuel mixture was used.

By focusing on the role of water, it could be stated that it has an impact on the presence of this threshold: with both fuels, in fact no evidence of its occurrence has been found in dry tests.

To achieve further proofs about the state of the catalytic surface, other experimental tools are needed. Also, a kinetic study is necessary in order to develop an ad hoc modelling tool to predict experimental data.

List of Figures

List of Tables

List of symbols

Chapter 1

Variable	Description	SI unit
$\boldsymbol{\lambda}$	equivalence ratio	-
$\boldsymbol{AFR}$	air-fuel ratio	-
$\boldsymbol{AFR^{st}}$	stoichiometric air-fuel ratio	-

Chapter2

Variable	Description	SI unit
$\boldsymbol{\dot{Q}_{H_2O,liq}}$	volumetric flow rate provided by the pump	mL/min
$\boldsymbol{\dot{Q}_{H_2O,gas}}$	water vapour flow rate in the reactants	NmL/min
$\boldsymbol{MW_{H_2O}}$	water molecular weight	g/mol
$\boldsymbol{\rho_{H_2O,liq}}$	water density at ambient conditions	g/mL
$\boldsymbol{t_{cat}}$	catalyst thickness on the support	cm
$\boldsymbol{d_w}$	support thickness	cm
$\boldsymbol{S_{mon}}$	side of the monolith square frontal section	cm
$\boldsymbol{Pitch}$	sum of the cordierite thickness d_w and channel side D	cm
$\boldsymbol{D_{h,ch}}$	length representative of the actual area available for the flow	cm
$\boldsymbol{\varepsilon}$	void fraction	cm
$\boldsymbol{A_{eq}}$	equivalent cross section area	cm
$\boldsymbol{\dot{Q}^{out}_{H_2O}}$	reactor outlet water volumetric flow rate	Nml/min
$\boldsymbol{\dot{Q}^{in}_{H_2O}}$	reactor inlet water volumetric flow rate	Nml/min
$\boldsymbol{\Delta\dot{Q}_{CH_4}}$	$\dot{Q}^{out}_{CH_4} - \dot{Q}^{in}_{CH_4}$	Nml/min
$\boldsymbol{\Delta\dot{Q}_{H_2}}$	$\dot{Q}^{out}_{H_2} - \dot{Q}^{in}_{H_2}$	Nml/min
$\boldsymbol{\alpha_i}$	i-species response factor	-
$\boldsymbol{\dot{Q}_i}$	i-species volumetric flow rate	Nml/min
$\boldsymbol{\dot{Q}_{N_2}}$	nitrogen volumetric flow rate	Nml/min
$\boldsymbol{A_i}$	area subtended by i-species peak	μV·s

A_{N_2}	area subtended by the nitrogen peak	μV·s
$A^*_{N_2}$	area of the "N_2 apparent peak"	μV·s
A_{Macro}	area subtended by the Macro peak	μV·s
m	number of species	-
$\dot{Q}_{tot}$	total volumetric flow rate	NmL/min
$\dot{N}_i$	i-species molar flow rate	mol/min
χ_i	i-species conversion	-
S_i	i-species selectivity	-
$\Delta\dot{N}_i$	$\dot{N}_i^{out} - \dot{N}_i^{in}$	mol/min
n_i^j	number of j-element atoms in i-species molecule	-
$\Delta\dot{N}_i^j$	molar flux of j-element relative to i-species with $\Delta\dot{N}_i \geq 0$	mol/min
B_C	carbon balance	-
B_H	hydrogen balance	-
B_O	oxygen balance	-
β_i	i-species response factor	A/ppm
$\Delta\mu_i$	$\mu_i^{feed} - \mu_i^{background}$	A
Δy_i	$y_i^{feed} - y_i^{background}$	ppm
$GHSV$	Gas Hourly Space Velocity	1/h
V_{mon}	monolithic sample volume	cm^3
$\dot{Q}_{air,engine}$	actual internal combustion engine inlet air flow rate	Ncm^3/min
$\dot{Q}^{st}_{air,engine}$	stoichiometric internal combustion engine inlet air flow rate	Ncm^3/min
y_i	i-species molar fraction at the ICE outlet (i.e., catalytic converter inlet)	-
S	catalyst equivalence ratio	-
$\dot{Q}_{air,cat}$	actual catalyst inlet air flow rate	Ncm^3/min
$\dot{Q}^{st}_{air,cat}$	stoichiometric catalyst inlet air flow rate	Ncm^3/min
y_{O_2}	catalyst inlet oxygen molar fraction	-
$y^{st}_{O_2}$	stoichiometric catalyst inlet oxygen molar fraction	-

Chapter 3

Variable	Description	SI unit
T_{oven}	oven setpoint temperature	°C
x	Catalyst axial coordinate	mm
r_{CH_4}	methane conversion rate	mol/m³/s
C_{CH_4}	methane molar concentration	mol/m³
C	total molar concentration	mol/m³
v	flow velocity	m/s
k^{app}	apparent reaction rate constant	1/s

Bibliography

[1] World Health Organization, *World Health Statistics 2022*. 2022. [Online]. Available: http://apps.who.int/bookorders.

[2] World Meteorological Organization, "State of the Global Climate 2021."

[3] European Parliament and the Council, "Directive 2009/28/EC on the promotion of the use of energy from renewable sources and amending and subsequently repealing Directives 2001/77/EC and 2003/30/EC. 2009" 2009.

[4] European Environment Agency, "Annual European Union greenhouse gas inventory 1990–2020 and inventory report 2022.", 2022.

[5] H. M. Cho and B. Q. He, "Spark ignition natural gas engines—A review" *Energy Conversion and Management*, vol. 48, no. 2, pp. 608–618, Feb. 2007, doi: 10.1016/J.ENCONMAN.2006.05.023.

[6] K. Biernat, I. Samson-bręk, Z. Chłopek, M. Owczuk, and A. Matuszewska, "Assessment of the environmental impact of using methane fuels to supply internal combustion engines" *Energies (Basel)*, vol. 14, no. 11, Jun. 2021, doi: 10.3390/en14113356.

[7] L. D. Danny Harvey, "A guide to global warming potentials (GWPs)" *Energy Policy*, vol. 21, no. 1, pp. 24–34, Jan. 1993, doi: 10.1016/0301-4215(93)90205-T.

[8] United Nations Organization, "PARIS AGREEMENT", 2015.

[9] European Commission, "COMMUNICATION FROM THE COMMISSION TO THE EUROPEAN PARLIAMENT, THE EUROPEAN COUNCIL, THE COUNCIL, THE EUROPEAN ECONOMIC AND SOCIAL COMMITTEE AND THE COMMITTEE OF THE REGIONS - The European Green Deal", 2020.

[10] European Commission, "ANNEX to the COMMUNICATION FROM THE COMMISSION TO THE EUROPEAN PARLIAMENT, THE EUROPEAN COUNCIL, THE COUNCIL, THE EUROPEAN ECONOMIC AND SOCIAL COMMITTEE AND THE COMMITTEE OF THE REGIONS - The European Green Deal.", 2020.

[11] European Commission, "Commission Regulation (EU) No 459/2012 of 29 May 2012 amending Regulation (EC) No 715/2007 of the European Parliament and of the Council and Commission Regulation (EC) No 692/2008 as regards emissions from light passenger and commercial vehicles (Euro 6)."

[12] K. Anagnostopoulos *et al.*, "*From NEDC to WLTP : effect on the type-approval CO2 emissions of light-duty vehicles. "*, *JRC Science for Policy Report*, 2017

[13] R. Suarez-Bertoa *et al.*, "On-road emissions of passenger cars beyond the boundary conditions of the real-driving emissions test", *Environmental Research*, vol. 176, p. 108572, Sep. 2019, doi: 10.1016/J.ENVRES.2019.108572.

[14] British petroleum , "Full report – Statistical Review of World Energy 2021."

[15] D. A. Hagos, E. Ahlgren, M. Stryg, T. Y. Hwan, and W. Jensen, "A state-of-the art review on the development of CNG/LNG infrastructure and natural gas vehicles (NGVs) ", Technical report FutureGas project, 2018.

[16] NGVA Europe, "NGVA Europe - Report of Activities 2020".

[17] L. Petrus and M. A. Noordermeer, "Biomass to biofuels, a chemical perspective", 2006, doi: 10.1039/b605036k.

[18] J. Niesner, D. Jecha, and P. Stehlík, "Biogas upgrading technologies: State of art review in european region", in *Chemical Engineering Transactions*, 2013, vol. 35, pp. 517–522. doi: 10.3303/CET1335086.

[19] T. Bridgwater, "Review Biomass for energy", *Journal of the Science of Food and Agriculture J Sci Food Agric*, vol. 86, pp. 1755–1768, 2006, doi: 10.1002/jsfa.2605.

[20] A. Molino, V. Larocca, S. Chianese, and D. Musmarra, "Biofuels production by biomass gasification: A review", *Energies (Basel)*, vol. 11, no. 4, Apr. 2018, doi: 10.3390/EN11040811.

[21] M. A. Toema, "PHYSICS-BASED CHARACTERIZATION OF LAMBDA SENSOR OUTPUT TO CONTROL EMISSIONS FROM NATURAL GAS FUELED ENGINES", PhD Thesis, Department of Mechanical and Nuclear Engineering, Kansas State University, 1995.

[22] R. M. Heck, S. Gulati, and R. J. Farrauto, "The application of monoliths for gas phase catalytic reactions", *Chemical Engineering Journal*, vol. 82, no. 1–3, pp. 149–156, Mar. 2001, doi: 10.1016/S1385-8947(00)00365-X.

[23] H. Santos and M. Costa, "Evaluation of the conversion efficiency of ceramic and metallic three way catalytic converters", *Energy Conversion*

and Management, vol. 49, no. 2, pp. 291–300, Feb. 2008, doi: 10.1016/J.ENCONMAN.2007.06.008.

[24] N. Guillén-hurtado, V. Rico-pérez, D. Lozano-castelló, and A. Bueno-lópez, "THREE-WAY CATALYSTS: PAST, PRESENT AND FUTURE", *Dyna*, vol. 79, pp. 114–121, 2012, [Online]. Available: http://www.redalyc.org/articulo.oa?id=49624956014

[25] W. Shan, Y. Zhang, C. Huang, ab Wenpo Shan, ab Zhihua Lian, and H. He acd, "Recent advances in three-way catalysts of natural gas vehicles", *Catal. Sci. Technol*, vol. 10, p. 6407, 2020, doi: 10.1039/d0cy01320j.

[26] M. Trueba and S. P. Trasatti, "γ-Alumina as a Support for Catalysts: A Review of Fundamental Aspects", *European Journal of Inorganic Chemistry*, vol. 17, pp. 3393-3403, 2005, doi: 10.1002/ejic.200500348.

[27] E. Yalamaç, A. Trapani, and S. Akkurt, "Sintering and microstructural investigation of gamma–alpha alumina powders", *Engineering Science and Technology, an International Journal*, vol. 17, no. 1, pp. 2–7, Mar. 2014, doi: 10.1016/J.JESTCH.2014.02.001.

[28] S.-H. Cai, S. N. Rashkeev, S. T. Pantelides, and K. Sohlberg, "Atomic Scale Mechanism of the Transformation of γ-Alumina to θ-Alumina", *Physical Review Letters*, vol. 89, no. 23, p. 235501, Nov. 2002, doi: 10.1103/PhysRevLett.89.235501.

[29] J. B. Miller and M. Malatpure, "Pd catalysts for total oxidation of methane: Support effects", *Applied Catalysis A: General*, vol. 495, pp. 54–62, Apr. 2015, doi: 10.1016/J.APCATA.2015.01.044.

[30] C. Huang, W. Shan, Z. Lian, Y. Zhang, and H. He, "Recent advances in three-way catalysts of natural gas vehicles", *Catalysis Science and Technology*, vol. 10, no. 19, pp. 6407–6419, Oct. 2020, doi: 10.1039/D0CY01320J.

[31] J. Kašpar, P. Fornasiero, and M. Graziani, "Use of CeO2-based oxides in the three-way catalysis", *Catalysis Today*, vol. 50, no. 2, pp. 285–298, Apr. 1999, doi: 10.1016/S0920-5861(98)00510-0.

[32] J. Du *et al.*, "Performance, structure and kinetics of Pd catalyst supported in Ba modified γ-Al2O3 for low temperature wet methane oxidation", *Chemical Engineering Journal*, vol. 430, p. 133113, Feb. 2022, doi: 10.1016/J.CEJ.2021.133113.

[33] W. Lin, Y. X. Zhu, N. Z. Wu, Y. C. Xie, I. Murwani, and E. Kemnitz, "Total oxidation of methane at low temperature over Pd/TiO2/Al2O3: effects of the support and residual chlorine ions", *Applied Catalysis B: Environmental*, vol. 50, no. 1, pp. 59–66, Jun. 2004, doi: 10.1016/J.APCATB.2004.03.009.

[34] H. Liu, B. Zhao, Y. Chen, C. Ren, and Y. Chen, "Rare earths (Ce, Y, Pr) modified Pd/La2O3ZrO2Al2O3 catalysts used in lean-burn natural gas fueled vehicles", *Journal of Rare Earths*, vol. 35, no. 11, pp. 1077–1082, Nov. 2017, doi: 10.1016/J.JRE.2017.07.006.

[35] P. Gélin and M. Primet, "Complete oxidation of methane at low temperature over noble metal based catalysts: a review", *Applied Catalysis B: Environmental*, vol. 39, no. 1, pp. 1–37, Nov. 2002, doi: 10.1016/S0926-3373(02)00076-0.

[36] L. He, Y. Fan, J. Bellettre, J. Yue, and L. Luo, "A review on catalytic methane combustion at low temperatures: Catalysts, mechanisms, reaction conditions and reactor designs", *Renewable and Sustainable Energy Reviews*, vol. 119, p. 109589, Mar. 2020, doi: 10.1016/J.RSER.2019.109589.

[37] D. Bounechada, "STRATEGIES FOR THE ENHANCEMENT OF LOW-TEMPERATURE CATALYTIC OXIDATION OF METHANE EMISSIONS", Chemical Engineering PhD Thesis, Politecnico di Milano, 2009.

[38] C. A. Mu, M. Maciejewski, R. A. Koeppel, R. Tschan, and A. Baiker, "Role of Lattice Oxygen in the Combustion of Methane over PdO/ZrO 2 : Combined Pulse TG/DTA and MS Study with 18 O-Labeled Catalyst", *The Journal of Physical Chemistry*, vol. 100(51), pp. 20006-20014, 1996, doi: 10.1021/jp961903a

[39] M. Monai, T. Montini, R. J. Gorte, and P. Fornasiero, "Catalytic Oxidation of Methane: Pd and Beyond", *European Journal of Inorganic Chemistry*, vol. 2018, no. 25. Wiley-VCH Verlag, pp. 2884–2893, Jul. 06, 2018. doi: 10.1002/ejic.201800326.

[40] D. Ciuparu, N. Katsikis, and L. Pfefferle, "Temperature and time dependence of the water inhibition effect on supported palladium catalyst for methane combustion", *Applied Catalysis A: General*, vol. 216, no. 1–2, pp. 209–215, Aug. 2001, doi: 10.1016/S0926-860X(01)00558-0.

[41] D. Ciuparu and L. Pfefferle, "Support and water effects on palladium based methane combustion catalysts", *Applied Catalysis A: General*, vol. 209, no. 1–2, pp. 415–428, Feb. 2001, doi: 10.1016/S0926-860X(00)00783-3.

[42] A. Gremminger, P. Lott, M. Merts, M. Casapu, J. D. Grunwaldt, and O. Deutschmann, "Sulfur poisoning and regeneration of bimetallic Pd-Pt methane oxidation catalysts", *Applied Catalysis B: Environmental*, vol. 218, pp. 833–843, Dec. 2017, doi: 10.1016/J.APCATB.2017.06.048.

[43] S. H. Oh and P. J. Mitchell, "Effects of rhodium addition on methane oxidation behavior of alumina-supported noble metal catalysts", *Applied*

Catalysis B: Environmental, vol. 5, no. 1–2, pp. 165–179, Dec. 1994, doi: 10.1016/0926-3373(94)00034-4.

[44] D. T. Wickham, B. A. Banse, and B. E. Koel, "Adsorption of nitrogen dioxide and nitric oxide on Pd", *Surface Science*, vol. 243, no. 1–3, pp. 83–95, Feb. 1991, doi: 10.1016/0039-6028(91)90347-U.

[45] C. S. Smith *et al.*, "Oxidation of Alkanes over Noble Metal Catalysts", I*ndustrial & Engineering Chemistry Product Research and Development*, vol. 19(3), pp. 293-298, 1980, doi: 10.1021/i360075a003

[46] V. A. Drozdov, P. G. Tsyrulnikov, V. v Popovskii, N. N. Bulgakov, E. M. Moroz, and T. G. Galeev, "COMPARATIVE STUDY OF THE ACTIVITY OF AI-Pd AND AI-Pt CATALYSTS IN DEEP OXIDATION OF HYDROCARBONS", *React Kinet Catal,* vol. 27, pp. 425-427, 1985, doi: 10.1007/BF02070487

[47] P. Gélin, L. Urfels, M. Primet, and E. Tena, "Complete oxidation of methane at low temperature over Pt and Pd catalysts for the abatement of lean-burn natural gas fuelled vehicles emissions: influence of water and sulphur containing compounds", *Catalysis Today*, vol. 83, no. 1–4, pp. 45–57, Aug. 2003, doi: 10.1016/S0920-5861(03)00215-3.

[48] K. Persson, A. Ersson, K. Jansson, N. Iverlund, and S. Järås, "Influence of co-metals on bimetallic palladium catalysts for methane combustion", *Journal of Catalysis*, vol. 231, no. 1, pp. 139–150, Apr. 2005, doi: 10.1016/J.JCAT.2005.01.001.

[49] K. Persson, K. Jansson, and S. G. Järås, "Characterisation and microstructure of Pd and bimetallic Pd–Pt catalysts during methane oxidation", *Journal of Catalysis*, vol. 245, no. 2, pp. 401–414, Jan. 2007, doi: 10.1016/J.JCAT.2006.10.029.

[50] D. Fino, N. Russo, G. Saracco, and V. Specchia, "CNG engines exhaust gas treatment via Pd-Spinel-type-oxide catalysts", *Catalysis Today*, vol. 117, no. 4, pp. 559–563, Oct. 2006, doi: 10.1016/J.CATTOD.2006.06.003.

[51] T. C. Xiao, S. F. Ji, H. T. Wang, K. S. Coleman, and M. L. H. Green, "Methane combustion over supported cobalt catalysts", *Journal of Molecular Catalysis A: Chemical*, vol. 175, no. 1–2, pp. 111–123, Oct. 2001, doi: 10.1016/S1381-1169(01)00205-9.

[52] H. Arai, T. Yamada, K. Eguchi, and T. Seiyama, "Catalytic combustion of methane over various perovskite-type oxides", *Applied Catalysis*, vol. 26, no. C, pp. 265–276, Jan. 1986, doi: 10.1016/S0166-9834(00)82556-7.

[53] F. Maschinenbau, "Automotive Three-Way Exhaust Aftertreatment under Transient Conditions-Measurements, Modeling and Simulation", Mechanical Engineering PhD Thesis, University of Stuttgard 2006.

[54] A. Knafl *et al.*, "Characterizing Light-Off Behavior and Species-Resolved Conversion Efficiencies During In-Situ Diesel Oxidation Catalyst Degreening", *SAE Transactions*, vol. 115, pp. 53–62, 2006. [Online]. Available: https://www.jstor.org/stable/44687468

[55] J. Gong *et al.*, "O2 dosage as a descriptor of TWC performance under lean/rich dithering in stoichiometric natural gas engines", *Catalysis Today*, vol. 360, pp. 294–304, Jan. 2021, doi: 10.1016/J.CATTOD.2020.02.022.

[56] P. Castellazzi, G. Groppi, P. Forzatti, E. Finocchio, and G. Busca, "Activation process of Pd/Al2O3 catalysts for CH4 combustion by reduction/oxidation cycles in CH4-containing atmosphere", *Journal of Catalysis*, vol. 275, no. 2, pp. 218–227, Oct. 2010, doi: 10.1016/J.JCAT.2010.07.028.

[57] F. Arosio, S. Colussi, A. Trovarelli, and G. Groppi, "Effect of alternate CH4-reducing/lean combustion treatments on the reactivity of fresh and S-poisoned Pd/CeO2/Al2O3 catalysts", *Applied Catalysis B: Environmental*, vol. 80, no. 3–4, pp. 335–342, May 2008, doi: 10.1016/J.APCATB.2007.11.030.

[58] M. Wang, P. Dimopoulos Eggenschwiler, D. Ferri, and O. Kröcher, "Experimental and modeling-based analysis of reaction pathways on catalysts for natural gas engines under periodic lean/rich oscillations", *Chemical Engineering Journal*, vol. 430, p. 132848, Feb. 2022, doi: 10.1016/J.CEJ.2021.132848.

[59] R. E. Hayes, S. T. Kolaczkowski, P. K. C. Li, and S. Awdry, "The palladium catalysed oxidation of methane: reaction kinetics and the effect of diffusion barriers", *Chemical Engineering Science*, vol. 56, no. 16, pp. 4815–4835, Aug. 2001, doi: 10.1016/S0009-2509(01)00131-2.

[60] M. Pagliari, "Low-temperature oxidation of methane on Pd-based monolith catalysts: spatially resolved concentration and temperature profiles.", Energy Engineering Master Thesis, Politecnico di Milano, 2021

[61] Y.-H. Chin, M. García-Diéguez, and E. Iglesia, "Supporting Information Dynamics and Thermodynamics of Pd-PdO Phase Transitions: Effects of Pd Cluster Size and Kinetic Implications for Catalytic Methane Combustion.", *The Journal of Physical Chemistry*, vol. 120 (3), pp. 1446-1460, doi: 10.1021/acs.jpcc.5b06677

[62] M. Wang, P. Dimopoulos Eggenschwiler, T. Franken, D. Ferri, and O. Kröcher, "Reaction pathways of methane abatement in Pd-Rh three-way

catalyst in heavy duty applications: A combined approach based on exhaust analysis, model gas reactor and DRIFTS measurements", *Chemical Engineering Journal*, vol. 422, p. 129932, Oct. 2021, doi: 10.1016/J.CEJ.2021.129932.

[63] C. Coney *et al.*, "Spatially-resolved investigation of the water inhibition of methane oxidation over palladium", *Catal. Sci. Technol*, vol. 10, p. 1858, 2020, doi: 10.1039/d0cy00154f.